NORTHWESTERN UNIVERSITY

Characterization of *in vivo* Human Olfactory System and Orbitofrontal Cortex Anatomy, and Olfactory Perceptual Decline in Aging and Dementia

A DISSERTATION

SUBMITTED TO THE GRADUATE SCHOOL
IN PARTIAL FULFILLMENT OF THE REQUIREMENTS

for the degree

DOCTOR OF PHILOSOPHY

Field of Neuroscience

By

Shiloh Luela Echevarria-Cooper

EVANSTON, ILLINOIS

March 2023

Abstract

Human olfactory function is important for a myriad of behaviors, including food seeking, social cognition, memory, emotional regulation, and detecting environmental threats. In animal models, particularly dense olfactory inputs have been shown to target orbitofrontal cortex (OFC), a region involved in multimodal sensory integration, reward coding, and flexibly guiding our motivated goal-directed behaviours. Both the primary olfactory cortex and the OFC have been shown in animal models to have widespread connectivity with medial temporal lobe regions involved in learning and memory. However, the specific anatomical properties and physical brain mechanisms through which the olfactory-OFC system influences behavior and memory are not well understood. In this thesis, we have developed optimized diffusion magnetic resonance imaging (dMRI) techniques to image the olfactory and orbitofrontal brain areas, and we have used a diffusion tractography approach to map out the anatomical connectivity of the human lateral olfactory tracts and OFC. By providing a detailed anatomical characterization of the human olfactory-OFC brain networks, we provide a valuable source of information from which to develop mechanistic hypotheses of human olfactory system and OFC function.

Interestingly, olfactory perceptual impairments are gaining notice as one of the earliest symptoms in Alzheimer's disease (AD), suggesting that olfactory perceptual tests may be sensitive to dysfunction in olfactory and medial temporal lobe regions. However, the specific mechanisms causing olfactory perceptual impairments in the earliest stages of AD are not known, and there is an open question about whether detecting olfactory impairments earlier on may help to target preventative treatments to slow the AD progression. In this thesis, we have shown that performance on the NIH Toolbox Odor Identification test declines with age, and is

worse in elderly adults with amnestic mild cognitive impairment (aMCI) and AD compared to those with normal cognition (NC). We also found that scores on this same test are able to detect which participants have aMCI versus NC, indicating that olfactory perceptual measures are sensitive to the earliest stages of the AD disease process.

Acknowledgments

During my time at Northwestern, I have received a lot of support from several notable individuals, without which I would not have been able to complete this work. I would first like to thank my thesis advisor, Dr. Thorsten Kahnt. Thorsten's scientific insight and attention to detail are unmatched, and he has helped me to deepen the way that I think about scientific problems and develop a strong understanding of the scientific process. Thank you for always pushing me to improve, teaching me how to approach a question from every possible angle, and encouraging my development into a confident and competent scientist. Being a part of your lab has truly been a rewarding and fulfilling experience.

I would also like to thank the members of my thesis committee, Drs. Christina Zelano, Todd Parrish, and Robert Vassar, for providing valuable advice, discussion, and encouragement over the years. I truly looked forward to every committee meeting because I knew that each of you would bring excitement and engaging discussion to the table regarding my thesis work.

In addition, I would like to thank my former professor and collaborator, Franco Pestilli. Thank you for helping me get my start in neuroscience research, teaching me all about diffusion MRI, and for introducing me to Thorsten. You have been one of my strongest advocates from the beginning, and I continue to value your friendship and collaboration.

I would also like to thank several past and present members of the Kahnt lab, including Vivek Sagar, Daria Porter, Laura Shanahan, Devyn Smith, Rachel Reynolds, James Howard, Fang Wang, Jana Tegelbeckers, Qingfang Liu, Donnisa Edmonds, Hamna Siddiqui, Yao Zhao, Sumedha Attani, and Tanya Bhargava. Thank you each for being there and fostering a fun and

supportive lab environment. I am grateful for the friendships that we have developed over the past five years.

I would also like to thank my good friends in NUIN for always bringing humor and fun to the grad school experience, especially Rogan Grant, Sarah Lurie, Lynn Ren, and Mariah Meyer. You guys are the real ones. Thank you for understanding my niche sense of humor and always have something equally silly to bring to the table.

I would next like to thank my family. Thank you to my dad, Steven Cooper, for setting me on this path and always going above and beyond to support me through this degree. I appreciate everything you do, and all the ways you have indulged my curiosity over the years. Thank you for letting me play with your brain-themed puzzles when I was little, while you studied for your Master's degree; and for letting me dissect a real cow brain on the kitchen counter in high school; and for buying me that huge Kandel book and letting me tell you about everything I read in it. I would never have accomplished any of the things that I have without you! Thank you to my mom, Tami Rogers, for talking to me just about every day and being a constant source of support over the last several years. Thank you for always asking about my research, and for being genuinely excited to hear me explain it, and for telling me often and loudly how proud you are of me. Thank you to my step-mom, Giselle Lima Cooper, for always being a bright ray of sunshine, excitement, and positivity. I look up to you as a scientist, as a role model, and as a person. Thank you for always making time for me and encouraging me to be my happiest self. Thank you to my brother, Joseph Cooper, and my sister, Michaela Cooper, for being my confidants and best friends. I'm so grateful for our closeness and for your love. Thank you to my grandparents, Joseph Cooper, Debbie Cooper, and Susan Hazzard. If it wasn't for

your hard work and legacy, I wouldn't be here today. You laid the groundwork to make life better for my parents and for me, and without you I would never be able to accomplish such big things.

Most importantly, I want to thank my best friend in the world, my husband, Dennis Echevarria-Cooper. We first met during NUIN orientation, and soon fell hard and fast in love. Through all the ups and downs in grad school and in life, you have been the one constant and stable thing that has kept me going. I have so much to thank you for and I have so much excitement and joy in thinking of our future together. You're the one person on this Earth that really sees me for me, the good and the bad, and you meet all of it with love and devotion. Wherever you are, there I'll be too, because you're my true love and my home.

Finally, these acknowledgements would not be complete without a mention of my two cats, Jack and Sylvia, who provided companionship and affection, alongside numerous interruptions and distractions, as cats are wont to do.

List of Abbreviations

ACT …….…….. Anatomically-constrained tractography

AD …… Alzheimer's disease

ADRC ……..… Alzheimer's disease research center

aMCI …….. Amnestic mild cognitive impairment

AMY …… Amygdala

ANCOVA ……...…….. Analysis of covariance

AON …… Anterior olfactory nucleus

APC …… Anterior piriform cortex (rat)

APOE …… Apolipoprotein E

ARMADA ……...….. Assessing reliable measurement in Alzheimer's disease and cognitive aging

AUC ……. Area under the curve

BSIT ……...…… Brief smell identification test

CoA …… Cortical nucleus of the amygdala (macaque)

CO_a …… Anterior cortical nucleus of the amygdala (rat)

CO_p …… Posterior cortical nucleus of the amygdala (rat)

CPOF …….. Centeroposterior orbitofrontal area (macaque)

CSD …… Constrained spherical deconvolution

CSF …… Cerebrospinal fluid

dlPFC …… Dorsolateral prefrontal cortex

dMRI ……... Diffusion magnetic resonance imaging

EC …….…… Entorhinal cortex

EPI …….….. Echo planar imaging

FA ……..…. Fractional anisotropy

fMRI …….. Functional magnetic resonance imaging

fODF ……..…….. Fiber orientation distribution function

FOD ……..…….. Fiber orientation distribution

FPC ……...…. Frontal piriform cortex (human)

GMWMI ……..... Gray matter-white matter interface

LEA ……...…… Lateral entorhinal area (rat)

LOT …… Lateral olfactory tract

LPOF …….. Lateroposterior orbitofrontal area (macaque)

MD ……...…….. Mean diffusivity

MEA ……..…… Medial entorhinal area (rat)

MNI …… Montreal Neurological Institute

MRI ……. Magnetic resonance imaging

MS-EPI ……...…… Multi-shot echo planar imaging

NC ……...…. Normal cognition

NIH …….. National Institutes of Health

NIHTB …….. National Institutes of Health Toolbox

NLOT ……..…… Nucleus of the lateral olfactory tract

OB …… Olfactory bulb

OFC …….. Orbitofrontal cortex

OT …… Olfactory tubercle

PAC …….. Periamygdaloid cortex

PC …… Piriform cortex

PET ……...… Positron emission tomography

PPC …… Posterior piriform cortex (rat)

RESOLVE ……Readout segmentation of long variable echo trains

RF …….…….. Radiofrequency

ROC …….……. Receiver operating characteristic

ROI …….…….. Region of interest

RS …… Rhinal sulcus

rs-fMRI ..…….. Resting-state functional magnetic resonance imaging

SCGM ……...……. Sub-cortical gray matter

SDOIT ……... San Diego Odor Identification Test

SII ……...….. Secondary somatosensory cortex

SIFT ……..…… Spherical deconvolution-informed filtering of tractograms

SS-EPI ……... Single-shot echo planar imaging

TDI Score …….…. Threshold + discrimination + identification Score

TE ……. Echo time

TOL…… Olfactory tubercle (macaque)

TPC …….…….. Temporal piriform cortex (human)

TT_V ……...…… Ventral tenia tecta

UPSIT …….. University of Pennsylvania Smell Identification Test

vmPFC ……...…….. Ventromedial prefrontal cortex

Table of Contents

List of Tables and Figures

Chapter 1: Background, Specific Aims, and Research Approach

1.1. Significance and Specific Aims

In our daily lives, we are faced with a wide assortment of emotionally motivating stimuli that demand behavioural responses. However, the value of these stimuli and the contexts in which we encounter them are not static. Our ability to learn and remember changing contexts and reward contingencies allows us to respond to incoming stimuli flexibly and in a goal-directed manner. A critical source of motivationally salient information is the sense of smell. Olfaction is tightly integrated with emotion, learning, and memory, and we rely on olfactory stimuli in our daily environments to inform our behaviours. Olfactory sensations play a role in several goal-directed behaviours, including food seeking and consumption, social cognition and mating behaviours, emotional regulation, memory encoding and retrieval, and detecting and responding to potential environmental threats. Strong olfactory functioning is important for adaptive behaviour, but unfortunately, impairments in olfactory function become more common as we age. Olfactory deficits are especially common in elderly adults who go on to develop amnestic mild cognitive impairment (aMCI) and Alzheimer's disease (AD), and often precede severe cognitive and memory impairments by several years.

From animal studies and human functional neuroimaging and lesion studies, we know that the ability to flexibly encode and update stimulus identity and reward values is supported by a part of the neocortex called the orbitofrontal cortex (OFC), located on the ventral surface of the frontal lobes. The OFC shares reciprocal connectivity with brain regions serving every sensory modality, and sends heavy outputs to visceromotor and limbic regions such as the hypothalamus, frontal premotor cortex, the striatum, the amygdala, and the hippocampus. It is thought to be

involved in multisensory integration and orchestration of motivated emotional and behavioural responses important for goal-directed behaviours. Olfactory inputs to the OFC are very dense and relatively "unprocessed" compared to the other sensory modalities. The OFC has been implicated in conscious odor perception and odor identification and discrimination. Olfactory information is first encoded in olfactory sensory neurons in the nasal epithelium, which project to the olfactory bulb, then to the primary olfactory cortex (including the piriform cortex), and from there to the OFC. The OFC thus serves as "secondary olfactory cortex", whereas for other sensory modalities, the OFC receives projections from higher order unimodal and polymodal sensory association cortices. Additionally, the OFC and primary olfactory cortex both share strong reciprocal connectivity with limbic system regions important for emotional regulation, learning, and memory. Understanding the anatomical connectivity of the human olfactory and orbitofrontal brain regions is essential to understanding how these structures encode olfactory information and use it to influence goal-directed behaviours. There is currently a large knowledge gap regarding human olfactory system anatomy, olfactory and orbitofrontal connectivity with limbic regions, and why the functions supported by these brain regions deteriorate in aMCI and AD.

While we have documented the anatomical connectivity of the lateral olfactory tracts and OFC in rodents and primates, these same anatomical connections have yet to be verified in the human brain. *Post mortem* data using methods such as dissection and histochemical methods such as silver staining are available, but they are unable to capture the full complexity of human olfactory system connectivity with precision. While diffusion magnetic resonance imaging (dMRI) is a robust tool for probing human brain connectivity and white matter properties *in vivo*,

the olfactory and OFC regions of the brain suffer from strong susceptibility artifacts due to their proximity to the sinus cavities, thus far preventing a thorough and accurate characterization of the olfactory and orbitofrontal white matter pathways. The first aim of this thesis project was then to develop an optimized dMRI protocol to clearly image the olfactory and orbitofrontal brain regions, and to characterize the cortical projections of the human lateral olfactory tracts *in vivo*. The second aim was then to characterize the gross anatomical connectivity of the human OFC, and to use a k-means clustering approach to parcellate this region into smaller subregions distinguished by unique connectivity. Aim 2 will provide a detailed, data-driven characterization of the intrinsic anatomical organization of the human OFC.

The olfactory, orbitofrontal, and limbic brain regions are particularly vulnerable to age and neurodegenerative diseases, including aMCI and AD. Functions supported by these brain regions include olfactory sensory function, learning and memory, and emotional regulation, all of which become progressively more disrupted in the AD disease process. Olfactory impairments become more likely as we age, and are often one of the earliest symptoms of neurodegenerative disease. To perform well on an odor identification test, participants must rely on intact olfactory sensory functioning, cognitive functions such as working memory and recognition memory, and semantic functions required for naming odor sources. Simple tests of odor identification have been proposed as a way to identify individuals who may be at risk of developing aMCI and further cognitive decline. Therefore, the third aim of this thesis project was to validate the NIH Toolbox Odor Identification Test for a population of elderly adults (above age 65) with normal cognition, aMCI, and AD, and to determine how well scores on this simple test are able to detect individuals with aMCI compared to individuals with normal cognition in this age group.

1.2. Background Literature Review

1.2.1. Mammalian Olfactory System Anatomy

In mammals, olfactory information first reaches the brain via the olfactory bulb, a neuronal structure whose axons form the first cranial nerve, also called the lateral olfactory tract. The olfactory bulbs send several parallel projections along the lateral olfactory tracts to several different cortical regions, comprising the primary olfactory cortex. These projections have been most extensively characterized in rodent models, using axon tracing and histology. Several studies have also characterized olfactory system connectivity in the primate, using axon tracing, histology, antidromal stimulation, and intracranial electroencephalography. Myelin staining and histological approaches have been used to evaluate the projections of the olfactory bulb and primary olfactory cortical structures in the *post mortem* human brain. A handful of more recent studies have used neuroimaging approaches to study *in vivo* human olfactory system anatomical and functional connectivity. A comparison of olfactory bulb and primary olfactory cortical projections in the rat, macaque, and human will be provided here.

Olfactory Bulb and Primary Olfactory Cortical Connectivity of the Rat. The projections of the olfactory bulb into primary olfactory cortex have been extensively characterized in the rat using horseradish peroxidase, as an anterograde and retrograde axon tracer (Haberly & Price, 1978a, 1978b). The olfactory bulb sends parallel afferents to several primary olfactory cortical areas, including the anterior olfactory nucleus and ventral tenia tecta, the anterior and posterior piriform cortices, the olfactory tubercle, the anterior cortical nucleus of the amygdala, periamygdaloid cortex, and the lateral entorhinal area. A drawing of the relative location of these structures on

the ventral surface of the rat brain is provided in **Figure 1.1**, reproduced from Haberly & Price 1978a. While the anterior olfactory nucleus, tenia tecta, and anterior piriform cortex were all found to send strong reciprocal connections back to the olfactory bulb, the lateral entorhinal area and the olfactory tubercle did not.

Among the listed primary olfactory cortical areas, Haberly & Price identified a loose pseudo-hierarchy of connectivity in the anterior-posterior direction. Anterior primary olfactory regions send projections back to posterior regions, with denser projections reaching closer structures and more diffuse projections reaching more distal structures. Posterior structures send reciprocal projections back to anterior structures, with the densest projections reaching the closest regions. The anterior olfactory nucleus and the anterior piriform cortex were found to send the heaviest commissural projections through the anterior commissure. The densest commissural projections of the anterior olfactory nucleus reached the contralateral anterior olfactory nucleus, olfactory bulb, and anterior piriform cortex. The densest commissural projections of the anterior piriform cortex reached the contralateral posterior piriform cortex, cortical nucleus of the amygdala, periamygdaloid cortex, and lateral entorhinal area. Following retrograde tracer injections, Haberly & Price additionally identified several subcortical projections of the primary olfactory cortex, including the hypothalamus, diagonal band, raphe nuclei, locus coeruleus, ventral tegmental area, and the paraventricular and parafascicular nuclei of the thalamus. In another study, electrical stimulation of the rat olfactory bulb was used to identify olfactory projections to the thalamus (Price & Slotnick, 1983). Responses were measured in the mediodorsal thalamic nucleus. Retrograde axonal tracers were then placed in this nucleus, and led to labeled cells in the olfactory tubercle, anterior piriform cortex, posterior

piriform cortex, periamygdaloid cortex, and the lateral entorhinal area, indicating that these primary olfactory cortical regions send projections to the mediodorsal thalamic nucleus in the rat. The secondary olfactory cortex of the rat is comprised of three major regions, including the lateral orbital area, the ventrolateral orbital area, and the agranular insular area. Together, these regions form a rudimentary orbitofrontal cortex. These regions receive heavy reciprocal projections from the piriform cortex, and from the mediodorsal thalamic nucleus (Illig, 2005; Ray & Price, 1992). Ray & Price (1992) have suggested a "triangular" organization with interconnectivity between the primary olfactory regions, mediodorsal thalamic nucleus, and secondary olfactory regions in the orbitofrontal cortex. Additionally, electrophysiological recordings have revealed highly correlated neuronal activity in both the piriform cortex and the orbitofrontal cortex of the rat in response to odorants (Schoenbaum & Eichenbaum, 1995).

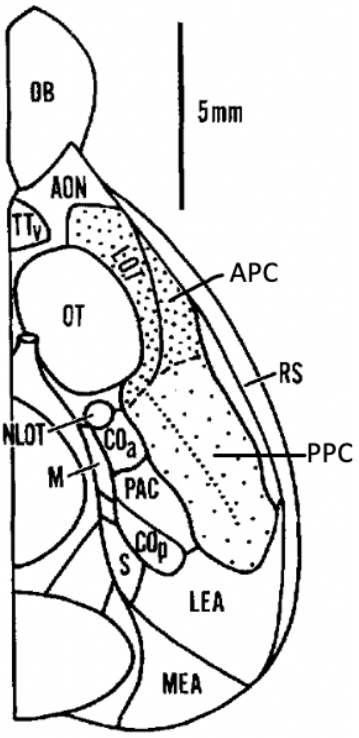

Figure 1.1. Olfactory cortical structures on the ventral surface of the rat brain. Abbreviations: OB, olfactory bulb; AON, anterior olfactory nucleus; TT_v, ventral tenia tecta; APC, anterior piriform cortex; PPC, posterior piriform cortex; OT, olfactory tubercle; LOT, lateral olfactory tract; RS, rhinal sulcus; NLOT, nucleus of the lateral olfactory tract; CO_a, anterior cortical nucleus of the amygdala; CO_p, posterior cortical nucleus of the amygdala; PAC, periamygdaloid cortex; LEA, lateral entorhinal area; MEA, medial entorhinal area. (Adapted from Fig. 2 of Haberly, L. B., & Price, J. L. (1978). Association and commissural fiber systems of the olfactory cortex of the rat. I. Systems originating in the piriform cortex and adjacent areas. *Journal of Comparative Neurology*, *178*(4), 711-740.Copyright 2004 by John Wiley and Sons, Inc.)

Olfactory Bulb and Primary Olfactory Cortical Connectivity of the Macaque. Carmichael, Clugent, & Price (1994) provide the most thorough characterization of olfactory system connectivity in the macaque monkey, using anterograde (fluororuby, biotinylated dextran amine, and ^{3}H-leucine) and retrograde (fast blue, diamindino yellow) axonal tracers (Carmichael et al., 1994). In this study, the olfactory bulb was found to send projections to the anterior olfactory nucleus, the ventral tenia tecta, the olfactory tubercle, frontal and temporal piriform cortices, the entopiriform nucleus, the periamygdaloid cortex, the anterior cortical amygdaloid nucleus, and the rostral entorhinal cortex. Each of these regions, aside from the olfactory tubercle, also sent reciprocal projections back to the bilateral olfactory bulbs. The density of olfactory bulb projections was highest for the anterior-most regions, including the anterior olfactory nucleus and frontal piriform cortex, and decreased in density toward more posterior regions, with the least dense projections sent to the periamygdaloid cortex and rostral entorhinal cortex. **Figure 1.2**, adapted from Carmichael, Clugent & Price (1994), illustrates the density of olfactory bulb projections to primary olfactory cortical regions.

Carmichael, Clugent & Price (1994) additionally identified several cytoarchitectural regions in the macaque orbitofrontal cortex that receive direct projections from the primary olfactory cortical regions. These include medial and central regions of the orbitofrontal cortex, including areas 13a, 13m, 14c, and 25, as well as agranular insular areas Iam, Iai, Ial, Iapl, and Iapm. The approximate location of each of these regions is illustrated in **Figure 1.3**, adapted from Ongur, Ferry & Price (2003). Each of these regions sent reciprocal projections back to primary olfactory cortex. Connections between the orbitofrontal cortex and primary olfactory cortex were organized topographically, such that more anterior primary olfactory cortical regions

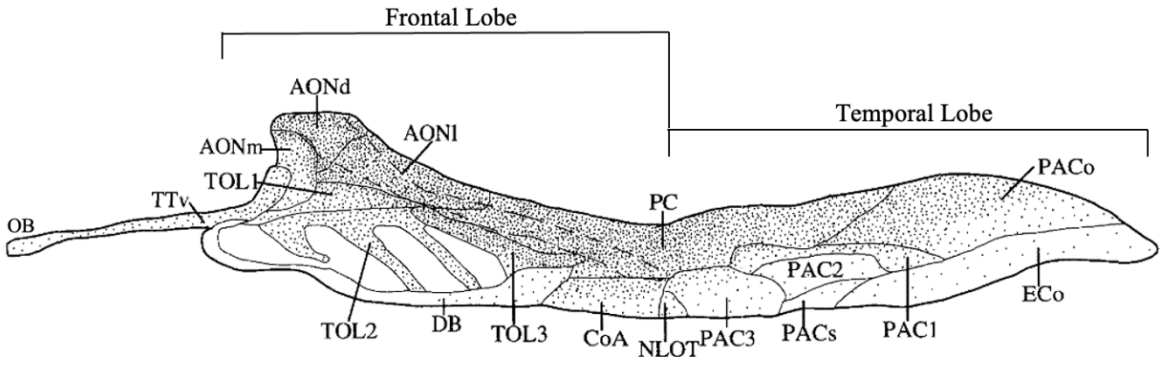

Figure 1.2. Map of the unfolded macaque primary olfactory cortex, at the junction of the frontal and temporal lobes. Density of stippling corresponds to the density of olfactory bulb afferent projections to each of the primary olfactory cortical regions. List of abbreviations: OB, olfactory bulb; AON, anterior olfactory nucleus; TT_v, ventral tenia tecta; TOL, olfactory tubercle; PC, piriform cortex; PAC, periamygdaloid cortex; CoA, cortical nucleus of the amygdala; NLOT, nucleus of the lateral olfactory tract; EC, entorhinal cortex. (Adapted from Fig. 2 of Carmichael, S. T., Clugnet, M. C., & Price, J. L. (1994). Central olfactory connections in the macaque monkey. Journal of Comparative Neurology, 346(3), 403-434. Copyright 2004 by John Wiley and Sons, Inc.)

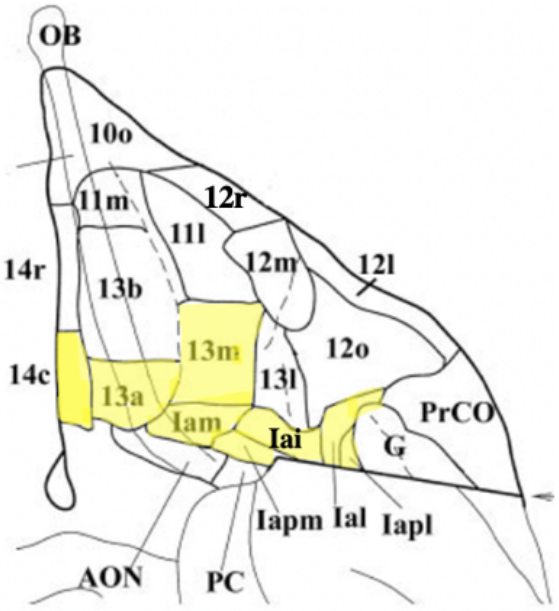

Figure 1.3. Cytoarchitectonic divisions of the macaque orbitofrontal cortex. A ventral view of the macaque frontal lobes is shown. Regions highlighted in yellow received direct projections from the primary olfactory cortex. Area 25, located on the medial wall below the rostrum of the corpus callosum, is not shown. (Adapted from Fig. 2 of Öngür, D., Ferry, A. T., & Price, J. L. (2003). Architectonic subdivision of the human orbital and medial prefrontal cortex. *Journal of Comparative Neurology*, *460*(3), 425-449.Copyright 2003 by John Wiley and Sons, Inc.)

sent denser projections to more medial orbitofrontal regions, and more posterior primary olfactory cortical regions sent denser projections to more lateral orbitofrontal regions. The authors additionally performed electrophysiological recordings in anaesthetized monkeys, and recorded multiunit evoked action potentials in the piriform cortex, anterior olfactory nucleus, olfactory tubercle, and orbitofrontal cortical areas 13a, Iam, and Iapm following olfactory bulb stimulation.

Similar to the rodent, evidence for indirect pathways from primary olfactory cortex to orbitofrontal cortex exist (Tanabe et al., 1975; Yarita et al., 1980). Using electrophysiological methods, Tanabe et al. (1975) identified a region of orbitofrontal cortex, termed the lateroposterior orbitofrontal area (LPOF), that exhibited evoked potentials following electrical stimulation of the olfactory bulb and following stimulation of the lateral hypothalamus. The authors found that LPOF activation and hypothalamic activation following olfactory bulb stimulation disappeared following an anterior piriform lesion, but LPOF could still be activated by lateral hypothalamus stimulation. The authors suggested a network of connectivity between the anterior piriform cortex, the lateral hypothalamus, and the LPOF region, which encompasses portions of areas 13, 12, and agranular insular area. In a separate study, Yarita et al. (1980) used electrophysiological methods to demonstrate a transthalamic olfactory pathway to the orbitofrontal cortex. They found that orthodromic stimulation of the olfactory bulb led to evoked potentials in the mediodorsal thalamic nucleus. Additionally, they found that antidromic stimulation of the centeroposterior portion of the orbitofrontal cortex (CPOF) led to activity in the same regions of the mediodorsal thalamic nucleus. The authors found that aspiration and electrolytic lesions to LPOF disrupted the macaques' ability to discriminate between different

odors, while lesions to the CPOF left olfactory discrimination intact. **Figure 1.4**, adapted from Yarita et al. (1980), shows the extent of the LPOF and CPOF regions.

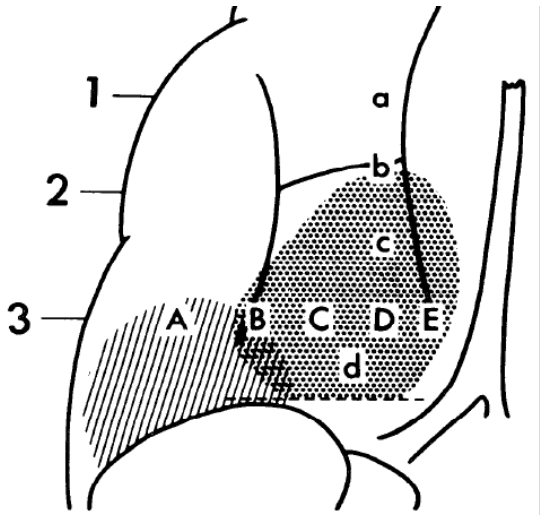

Figure 1.4. Centeroposterior and latero-posterior orbitofrontal areas (CPOF and LPOF) of the macaque frontal lobe. Stippled region shows extent of the CPOF region implicated in the indirect olfactory pathway through the mediodorsal thalamic nucleus. Hatched region shows the extent of the LPOF region implicated in the indirect olfactory pathway through the lateral hypothalamus. (Adapted from Fig. 3 of Yarita, H., Iino, M., Tanabe, T., Kogure, S., & Takagi, S. F. (1980). A transthalamic olfactory pathway to orbitofrontal cortex in the monkey. *Journal of Neurophysiology*, *43*(1), 69-85. Copyright 1980 by The American Physiological Society)

Human Olfactory System Anatomy. In the human brain, establishing the precise projections of the olfactory bulb to primary olfactory cortex has been challenging due to methodological limitations. The piriform cortex, olfactory tubercle, and anterior olfactory nucleus have been identified using histological and immunohistochemical methods (Allison, 1954; Gottfried, 2010; Ongür et al., 2003a; Zhou et al., 2019). The piriform cortex is located at the junction of the frontal and temporal poles, and may be divided into frontal and temporal sections. The anterior olfactory nucleus is located at the posterior end of the olfactory sulcus, adjacent to the olfactory trigone. The olfactory tubercle has been identified as a cluster of cells that overlap with, but are histologically distinct from, the base of the nucleus accumbens (Mesulam et al., 1992). In a silver myelin staining study, Allison (1954) identified dense projections from the *post mortem* human olfactory bulb to the anterior olfactory nucleus, the olfactory tubercle, the frontal and temporal

divisions of piriform cortex, and the cortico-medial amygdala nuclei. Allison noted three branches of the olfactory tracts, termed striae, with a medial stria reaching the olfactory tubercle, a small intermediate stria reaching the anterior olfactory nucleus, and the largest lateral stria reaching the piriform and olfactory amygdala. Allison failed to find any direct projections from the olfactory bulb to the entorhinal cortex.

Two more recent neuroimaging studies have attempted to map the projections of the olfactory bulb into primary olfactory cortex using diffusion magnetic resonance imaging (dMRI), but were unable to provide a comprehensive characterization of these projections due to methodological limitations, low signal, and susceptibility artifacts in these brain regions (Fjaeldstad et al., 2017; Milardi et al., 2017). Fjaeldstad et al. (2017) reconstructed the main body of the olfactory tracts, but were unable to identify the branching striae, as they used a tensor model that is unable to resolve multiple fiber directions within single voxels. Milardi et al. (2017) used a constrained spherical deconvolution model, which is able to resolve crossing fibers. While they successfully reconstructed the lateral striae, they were unable to reconstruct the intermediate or medial striae due to poor resolution and susceptibility artifacts present near the sinus cavities.

Recently, we used resting state functional MRI (rs-fMRI) to evaluate the functional connectivity patterns of the primary olfactory cortex (Zhou et al., 2019). Zhou et al. used a k-means clustering approach to delineate the primary olfactory cortex into four clusters based on distinguishable functional connectivity patterns. The resulting four clusters, shown in **Figure 1.5**, corresponded to the anatomical boundaries of the frontal piriform cortex, temporal piriform cortex, anterior olfactory nucleus, and olfactory tubercle, suggesting differing functional

connectivity for these regions. All four regions showed strong connectivity with the posterior orbitofrontal cortex, the anterior insula, the hippocampus, and the amygdala. The anterior olfactory nucleus showed strong connectivity with extensive regions in the orbitofrontal cortex, and posterior hypothalamic nucleus. The olfactory tubercle showed connectivity with the medial prefrontal cortex, the left temporal fusiform cortex, and the ventral striatum. The frontal piriform cortex showed strong connectivity with the mediodorsal thalamic nucleus and the dorsal striatum. The temporal piriform cortex showed connectivity with the inferior frontal gyri, the temporal pole, the superior temporal gyri, the hippocampus, and the posterior insula. It is possible that the differing functional connectivity profiles of these four regions are evidence of differing functional roles, which may be supported by differing anatomical connections.

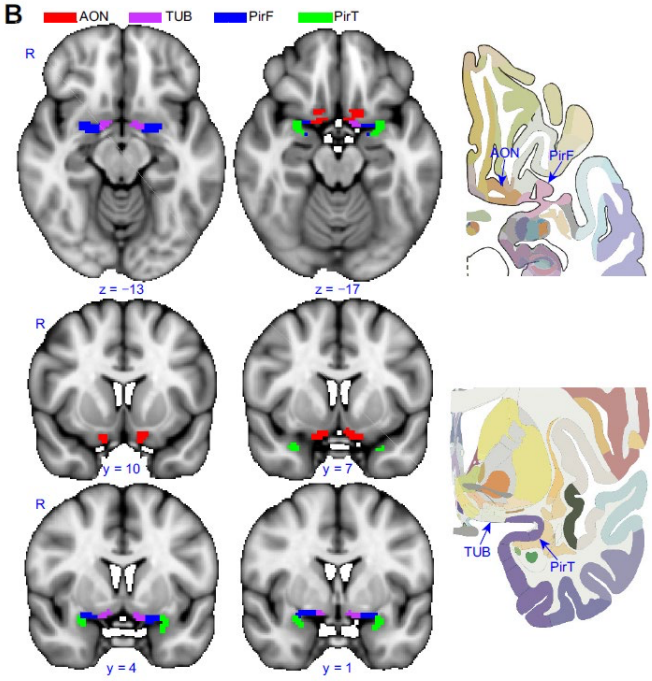

Figure 1.5. K-means clustering of the human primary olfactory cortex into four regions, corresponding to the anterior olfactory nucleus (AON), olfactory tubercle (TUB), frontal piriform (PirF) and temporal piriform (PirT). (Reproduced from Zhou, G., Lane, G., Cooper, S. L., Kahnt, T., & Zelano, C. (2019). Characterizing functional pathways of the human olfactory system. *Elife*, *8*, e47177. under Creative Commons License (https://creativecommons.org/licenses/by/4.0/legalcode)).

1.2.2. Primate and Human Orbitofrontal Cortex Anatomy and Function

The orbitofrontal cortex (OFC) refers to the neocortex located on the ventral surface of the frontal lobes, just above the eye orbits. The OFC receives inputs from brain areas involved in every sensory modality, including olfactory, gustatory, visual, auditory, somatosensory, viscerosensory, and limbic inputs. Outputs from the OFC target diverse limbic, premotor, and visceromotor regions, including the hippocampus, hypothalamus, lateral prefrontal cortex, and the striatum. The OFC is thus situated to serve a complex functional role in behaviour, and has been implicated in multimodal sensory integration, representation of motivationally salient memories, flexible updating of reward values for specific stimuli based on context and experience, visceromotor and emotional regulation, and coordinating adaptive goal-directed behaviour (Howard & Kahnt, 2021; Rudebeck & Rich, 2018; Stalnaker et al., 2015; Wallis, 2012). The specific connectivity of the human OFC and the precise mechanisms by which it carries out its various functional roles to coordinate behaviour are not well understood. In the present section, I present a summary of the human and primate OFC cytoarchitectural organization, a detailed description of primate OFC anatomical connectivity identified with axon tracing and electrophysiological methods, and descriptions of the major white matter fibers and functional connectivity of the human OFC identified with *in vivo* dMRI and fMRI methods. Additionally, I present a summary on the olfactory-specific anatomy and function of the OFC.

Anatomical Connectivity of the Orbitofrontal Cortex. The macaque and human OFC have both been divided into several cytoarchitecturally-distinct regions, with a numbering system that denotes likely homologues across species (Carmichael & Price, 1994; Mackey & Petrides, 2010;

Ongür et al., 2003a; Petrides & Pandya, 2002). The major regions identified in both the macaque and human include area 10 comprising the ventral frontal poles, area 11 just posterior to area 10, area 47/12 along the lateral side, area 13 in the center, area 14 along the medial side forming gyrus rectus, and the agranular insular region along the posterior side, bordering the frontal operculum of the insula. These regions are then further subdivided based on morphological differences observed with different histological techniques. These regions are shown above on a drawing of the macaque OFC in **Figure 1.3**, and below outlined on the human OFC in **Figure 1.6**, adapted from Ongur et al., (2003).

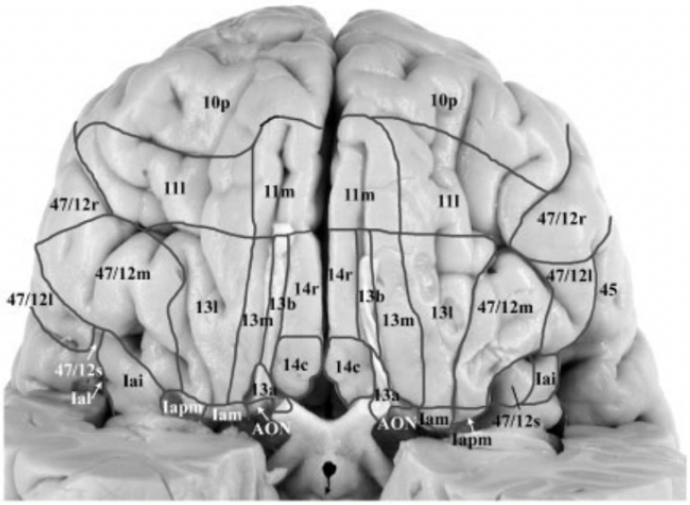

Figure 1.6. Cytoarchitectonic divisions of the human orbitofrontal cortex. Ventral view of the human frontal lobes with temporal lobes resected. (Reproduced from Fig. 2 of Öngür, D., Ferry, A. T., & Price, J. L. (2003). Architectonic subdivision of the human orbital and medial prefrontal cortex. *Journal of Comparative Neurology*, *460*(3), 425-449. Copyright 2003 by John Wiley and Sons, Inc.)

The white matter connectivity of the OFC has been extensively studied in the macaque using axonal tracing techniques. The macaque OFC has widespread connectivity with sensory and premotor brain regions, and receives input from every sensory modality (Carmichael & Price, 1995b). Visual inputs to OFC are heaviest in area 12l and arise from ventral temporal lobe area TE, along the ventral and lateral surfaces of the temporal lobe. This region is considered a homologue of human Brodmann areas 20-21, and consists of visual association cortex involved in object recognition, along the ventral visual stream, or "what" pathway. Auditory inputs are

heavies to OFC areas 12o, 13a, and Iai, arising from the superior temporal gyrus and parainsular cortex in the limiting sulcus. These regions correspond to secondary auditory cortex and auditory association cortex, and encompass regions near what is considered to be Wernicke's area in the human. Heavy somatosensory inputs reach OFC area 12m, arising from areas SII, 7a, 7b, opercular areas 1-2, the anterior inferior parietal lobule, posterior granular insula, and parts of area 3b. These regions correspond to human analogues in primary (areas 1-3) and secondary somatosensory cortex (SII), parietal cortical regions involved in visuomotor coordination (area 7 and inferior parietal lobule), and posterior insular regions involved in proprioception and interoception. Gustatory and viscerosensory inputs reach primary gustatory cortex (area G noted in **Figure 1.3**) and agranular insular areas Iapm and Ial via the ventroposterior medial thalamic nucleus, which serves as a relay from the nucleus of the solitary tract. Area G then sends further projections to OFC area 13l. Olfactory inputs from primary olfactory cortex to the OFC are numerous, and reach areas 13a, 13m, 13l, Iam, Iapm, Iai, Ial, and Iapl. Much of the lateral OFC, including areas 11l, 12r, 12m, 12l, 12o, 13m, and 13l, receive premotor inputs from dorsal area 6, corresponding to the supplementary eye field, and ventral area 6. Area 12l, which receives visual inputs, receives the heaviest premotor projections from the supplementary eye fields, while area 12m, which receives somatosensory inputs, receives the heaviest premotor projections from ventral area 6.

Limbic connectivity with the macaque OFC was also extensively characterized by Carmichael & Price in a separate study (Carmichael & Price, 1995a). The authors found heavy reciprocal connections between the amygdala and OFC, with the densest connections in areas 14r, 14c, 11m, 13b, 13a, Iam, Iapm, Ial, 12o, and 12l. Connectivity with the amygdala was

heaviest along the posterior, medial, and lateral borders of OFC, and relatively sparse in central and rostral orbital areas. The subiculum, part of the hippocampal formation, was found to have a substantial projection to OFC areas 10o, 11m, 13a, 13b, 14r, and 14c. Areas 13a, 13b and 11m were found to send some reciprocal projections back to the subiculum. Several regions of parahippocampal cortex share reciprocal connectivity with the OFC. The parahippocampal gyrus shared reciprocal connectivity with the medial-most regions of the OFC, areas 14r, 14c, 11m, and 13a. The entorhinal cortex was found to share connectivity with medial regions 14r, 14c, 11m, 13b, and 13a, as well as agranular insular regions Iam, Iapm, Ial, and Iai. The agranular insular regions of OFC tended to share connectivity with the rostral (olfactory) portion of the entorhinal cortex, while medial OFC regions were connected with more caudal portions of entorhinal cortex. Perirhinal cortex shared connectivity with OFC regions just lateral to those connected with entorhinal cortex, including areas 11m, 13b, 13a, 13m, and 13l, as well as with the agranular insular areas Iam, Iapm, Iai, and Ial. The OFC also shares widespread connectivity with the anterior cingulate cortex and the temporal pole. Medial areas 14r, 14c, 11m, 13a, and 13b, and lateral areas 12o and 12r shared strong connectivity with the anterior cingulate cortex. Virtually the entire OFC shares connectivity with the temporal pole, and is topographically organized. Caudal and central areas of OFC (Iam, Ial, 13m, 13a, and 13b) shared the heaviest connectivity with ventromedial temporal pole. Lateral and rostral areas of OFC (12o, 12l, 12m, 10o, and 14r) shared the heaviest connectivity with the dorsolateral temporal pole. Areas 11m and 11l had heaviest connectivity with the central regions of the temporal pole, and areas 14c and Iai received projections from the entire extent of the temporal pole.

Additional projections linking macaque OFC with various subcortical structures have been described, including the striatum, hypothalamus, and thalamus. The macaque OFC shares strong, topographically organized connectivity with the ventral striatum, an important structure linking limbic and motor systems (Ferry et al., 2000; Haber et al., 1995; Haber & Knutson, 2010). Medial OFC area 14 shared the densest connectivity with the medial ventral striatum, central area 13 shared the densest connectivity with the lateral ventral striatum, and lateral area 12 shared dense connectivity with the nucleus accumbens. These cortico-striatal connections are critical to reinforcement learning and reward processing, and are heavily regulated by dopaminergic inputs from the ventral tegmental area and substantia nigra (Haber & Knutson, 2010). The caudal orbitofrontal cortex (areas 13a, 12o, and Iai in particular) send strong projections to the lateral hypothalamus (Öngür et al., 1998; Rempel-Clower & Barbas, 1998). The caudal orbitofrontal cortex, along with the ventromedial prefrontal cortex and (to a lesser extent) the anterior insula, provide strong inputs to the hypothalamus and are thought to help regulate its autonomic function. The macaque OFC receives input from several thalamic nuclei, including the midline, anteromedial, anteroventral, ventral anterior, paracentral, central medial, ventroposterior medial, and mediodorsal nuclei (Cavada et al., 2000). The inputs from the mediodorsal thalamic nucleus are the largest and most studied (Giguere & Goldman-Rakic, 1988; Ray & Price, 1992; Yarita et al., 1980). The mediodorsal nucleus is thought to serve as an olfactory thalamic relay in the “indirect” pathway between primary olfactory cortex and OFC (Yarita et al., 1980). Additionally, the mediodorsal nucleus serves as the thalamic node in the limbic cortico-striato-thalamo-cortical loop, involving the OFC and the ventral striatum (Haber & Knutson, 2010). Portions of caudal OFC likely receive gustatory information via projections

of the ventroposterior medial thalamic nucleus (Carmichael & Price, 1995b). Additionally, many of the same regions of OFC that received inputs from the subiculum (14r, 13a, 13b, and 11m) also received inputs from the anteromedial thalamic nucleus, which is heavily connected to the subiculum and thought to be involved in memory and head positioning in spatial navigation (Carmichael & Price, 1995a).

Several major white matter structures have been identified as having connectivity with the human OFC, and have been delineated using dMRI methods. These include the uncinate fasciculus, the inferior fronto-occipital fasciculus, the orbito-polar tract, the extreme capsule, the fornix, the cingulum, amygdala fibers, and ventral striatal fibers (Croxson et al., 2005; Heather Hsu et al., 2020; Thiebaut de Schotten et al., 2012). Temporal pole connectivity with the OFC via the uncinate fasciculus has been described in the human brain using Klingler (freeze-and-break) dissection methods, as well as dMRI methods (Ebeling & Cramon, 1992; Leng et al., 2016; Thiebaut de Schotten et al., 2012). An additional white matter pathway of special interest is the inferior fronto-occipital fasciculus, which has been described in the human brain using both Klingler dissection and dMRI, but is noticeably absent from the primate brain (Catani & Thiebaut de Schotten, 2008; Martino et al., 2010; Thiebaut de Schotten et al., 2012). This human-specific fiber pathway appears to connect anterior orbitofrontal cortex and frontal pole with the posterior fusiform gyrus, superior parietal lobe, and anterior occipital cortex, and may carry visual and semantic inputs to the orbitofrontal cortex.

Medial-Lateral Organization of the Orbitofrontal Cortex. Based on intrinsic connectivity between OFC subregions, the macaque OFC can be subdivided into a medial network and a lateral network (Carmichael & Price, 1996). Regions in the medial network include areas Iai,

14c, 14r, 11m, 10o, and 10m; regions in the lateral (orbital) network include areas 12l, 12m, 12r, 11l, 13l, Ial, Iapm, Iam, 13m, and 13b. Regions within the medial network are highly interconnected with each other, and regions in the lateral network are highly interconnected, but there are relatively few connections between medial regions and lateral regions. Two central OFC regions, 13a and 12o, shared strong connectivity with both the medial and lateral networks, and may serve to coordinate activity between them. There are also noticeable differences in the connectivity of the medial and lateral networks with the rest of the brain. Lateral network regions tend to be the target of heavy sensory inputs, and receive inputs from every sensory modality and from premotor regions. Medial network regions, in contrast, receive few direct sensory inputs, but send heavy outputs to limbic and visceromotor regions, including the hypothalamus, hippocampus, cingulate gyrus, and ventromedial prefrontal cortex. In a more recent study, Cerliani et al. (2017) performed a diffusion tractography-based parcellation of 5 *ex vivo* macaque frontal lobes (3 left and 2 right hemispheres) (Cerliani et al., 2017). They measured ipsilateral cortico-cortical connectivity for each frontal lobe voxel (connectivity with subcortical gray matter regions was not assessed). Voxels were sorted into clusters based on a principal component analysis, and they consistently identified 11 principal components in each hemisphere. Two of these subdivisions covered the OFC; one was comprised of medial area 14, parts of area 10, and the ventromedial prefrontal cortex (vmPFC), while the other was comprised of lateral areas 11, 12, 13, and parts of area 10. The lateral OFC cluster that they identified shared connectivity with dorsolateral prefrontal cortex (dlPFC), the posterior cingulate, the precuneus, dorsal parietal cortex, and medial, lateral, ventral, and polar temporal cortex. The

medial OFC cluster that they identified had less widespread connectivity, but reached the anterior cingulate and the anterior temporal pole.

The medial-lateral organization of the OFC has also been shown in human resting-state functional connectivity studies (rs-fMRI) (Kahnt et al., 2012; Kahnt & Tobler, 2017). Kahnt et al. (2012) used k-means clustering to sort OFC voxels based on their resting state functional connectivity with the rest of the brain. For K=2, they identified one medial-posterior OFC cluster and one cluster in antero-lateral OFC. The medial-posterior cluster showed strong functional connectivity with the ventromedial prefrontal cortex, the superior frontal gyrus, the inferior parietal cortex, the middle and inferior temporal cortex, the posterior cingulate, the precuneus, the ventromedial striatum, the parahippocampal gyrus, and the temporal pole. The antero-lateral cluster shared strong connectivity with the inferior and middle frontal gyri, the inferior parietal cortex, the inferior temporal gyrus, the medial superior frontal gyrus, and the dorsal striatum. For K=6, the authors identified a medial cluster along gyrus rectus, a posterior-central cluster corresponding roughly to area 13, a central OFC cluster, and three lateral OFC clusters along the rostro-caudal extent of lateral OFC. The medial cluster showed strongest functional connectivity with the inferior parietal cortex, anterior middle and inferior temporal gyri, medial prefrontal cortex, posterior cingulate cortex, medial temporal cortex, and the temporal pole. The posterior-central cluster showed strongest functional connectivity with the hypothalamus, basal forebrain, ventral striatum, and parahippocampal gyrus. The central cluster had strong functional connectivity with the anterior insula, the left ventrolateral prefrontal cortex, the anterior cingulate cortex, and the dorsal and ventral striatum. The three lateral clusters showed strongest functional connectivity with lateral prefrontal cortex, the middle and inferior temporal cortex, the medial

superior frontal gyrus, and the supplementary motor area. Kahnt & Tobler (2017) further discovered that suppressing dopaminergic inputs to OFC by administering the D_2 receptor antagonist amisulpride disrupts the organization of these clusters. **Figure 1.7** illustrates the macaque medial and lateral networks based on white matter connectivity patterns, adapted from Carmichael & Price (1996), as well as the 2- and 6-cluster rs-fMRI solutions in the human OFC, adapted from Kahnt et al. (2012).

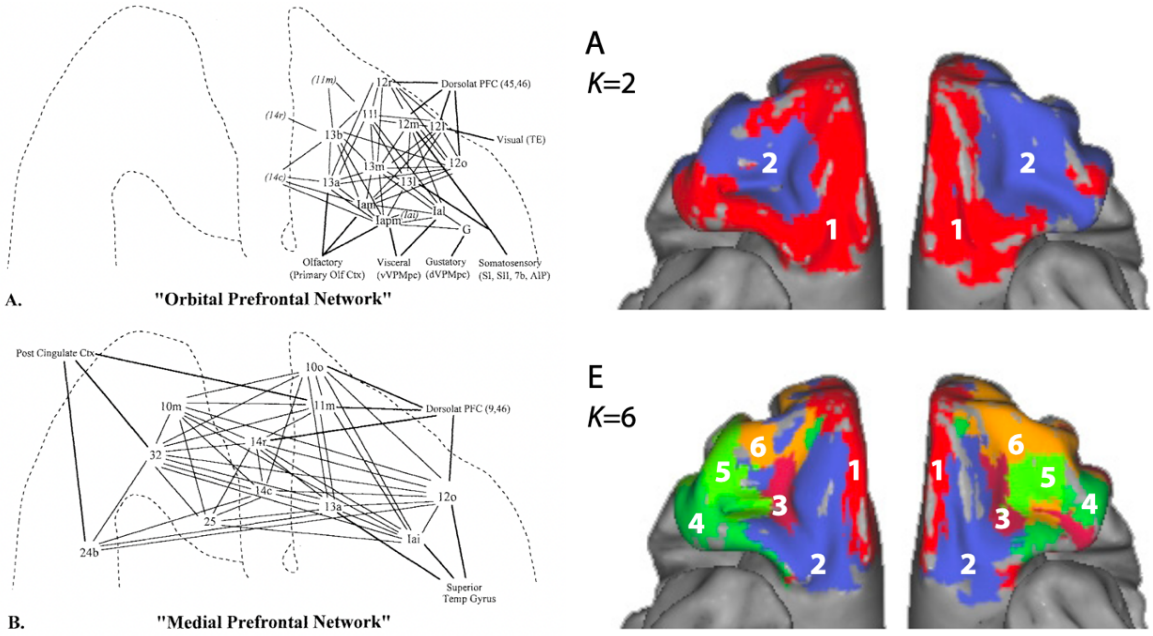

Figure 1.7 Medial and lateral networks of the orbitofrontal cortex. **Left panel:** Diagram of the Medial prefrontal network and Lateral (Orbital) prefrontal network of the macaque OFC, based on anatomical connectivity patterns of OFC subregions. (Reproduced from Fig. 19 of Carmichael, S. T., & Price, J. L. (1996). Connectional networks within the orbital andial prefrontal cortex of macaque monkeys. *Journal of Comparative Neurology*, *371*(2), 179-207. Copyright 1998 by John Wiley and Sons, Inc.). **Right panel:** K-means parcellation of the human orbitofrontal cortex based on resting-state fMRI connectivity profiles, for K=2 (top) and K=6 (bottom). (Reproduced from Fig. 3 of Kahnt, T., Chang, L. J., Park, S. Q., Heinzle, J., & Haynes, J. D. (2012). Connectivity-based parcellation of the human orbitofrontal cortex. *Journal of Neuroscience*, *32*(18), 6240-6250. under Creative Commons License (https://creativecommons.org/licenses/by-nc-sa/3.0/legalcode)).

Rostro-Caudal Organization of the Orbitofrontal Cortex. The human and primate OFC has distinct cytoarchitectural features and connectivity patterns that vary along the rostro-caudal dimension (Carmichael & Price, 1994; Ongür et al., 2003a). In both humans and primates, more rostral regions of the OFC, including areas 10, 11, and 47/12, are characterized by granular cortex, with a dense granule cell layer (layer IV). More caudal regions, including the agranular insula, are characterized by agranular cortex, with a very sparse granule cell layer and a larger layer V. Central region of OFC, including areas 13 and 14, exhibit dysgranular cortex with a present, but not dense, granule cell layer. In general, cortico-cortical projections of the OFC tend to match in terms of granularity, in that more granular cortical regions project to rostral granular OFC, and less granular neocortical regions and paleocortical regions project to central dysgranular and caudal agranular OFC (Cavada et al., 2000; Kringelbach & Rolls, 2004). Granular OFC receives the densest visual, somatosensory, and auditory inputs, while agranular OFC receives the densest olfactory, gustatory, and visceral inputs.

The Olfactory Orbitofrontal Cortex. The orbitofrontal cortex of the rat and macaque serves as "secondary olfactory cortex", receiving direct projections from primary olfactory cortex (Carmichael et al., 1994; Carmichael & Price, 1995b; Haberly & Price, 1978a, 1978b), and indirect projections from primary olfactory cortex via the mediodorsal nucleus of the thalamus (Potter & Nauta, 1979; Price & Slotnick, 1983; Tanabe et al., 1975; Yarita et al., 1980). While the macaque OFC receives inputs from every sensory modality, and is involved in multimodal sensory integration, the olfactory information reaching the OFC is relatively "unprocessed" compared to the visual, auditory, and somatosensory information. Pathways relating to these

senses are routed through secondary, tertiary, and association regions before reaching the OFC, whereas olfactory inputs come directly from primary olfactory cortex, placing the OFC only three synapses away from the site of olfactory sensory transduction in the nasal epithelium (Carmichael & Price, 1995b; Cavada et al., 2000). The secondary olfactory regions of the macaque OFC are also somewhat segregated from the regions first reached by other sensory modalities. Olfactory inputs to the OFC reach more posterior-medial agranular cortical regions that share strong connectivity with limbic and visceral structures, while the visual, auditory, and somatosensory inputs to the OFC reach more antero-lateral granular cortex that is further removed from limbic and visceral regions (Carmichael & Price, 1995a, 1995b; Kringelbach & Rolls, 2004). Thus, olfactory inputs are uniquely situated to quickly influence visceral, emotional, and memory processes regulated by the OFC.

Several human lesion studies have found that right orbitofrontal cortical lesions disrupt conscious odor perception, odor discrimination, and odor naming, although autonomic responses to odorants may be preserved (Jones-Gotman & Zatorre, 1993; W. Li et al., 2010; Potter & Butters, 1980). Additionally, *in vivo* human neuroimaging studies have implicated the OFC in odor detection and identification (Gottfried & Zald, 2005; Sobel et al., 1998; Zatorre & Jones-Gotman, 1991), odor discrimination (Bowman et al., 2012), flexible experience-based odor reward value and identity representation (Howard et al., 2015; Howard & Kahnt, 2017; W. Li et al., 2006), and expected future olfactory reward outcomes (Howard et al., 2020; F. Wang et al., 2020). The human OFC has also been shown to flexibly alter its responding to specific odorants depending on experience, including in olfactory habituation (W. Li et al., 2006) and devaluation (O'Doherty et al., 2000) paradigms. The human OFC is likely critical for generating our

olfactory perceptual experiences, as well as modifying them following learning and in response to our current internal motivational states.

1.2.3. Diffusion Magnetic Resonance Imaging and Tractography

Diffusion magnetic resonance imaging (dMRI) is currently the only method available for investigating the structure of *in vivo* white matter pathways. This method uses magnetic gradients to measure the Brownian motion of water (diffusion) through brain tissue. The diffusion signal intensity depends inversely on the magnitude of water displacement measured along a particular axis through the tissue. In the cerebrospinal fluid (CSF) there are no organized cell structures, so the diffusion signal is weak and *isotropic* (equal in magnitude along every axis). In the gray matter, approximately spherical cell bodies are packed together and provide some impediment to diffusion. The diffusion signal in the gray matter will be slightly stronger, but still isotropic. In the white matter, myelinated axons are organized into myelinated fibers with a particular orientation. Diffusion will be greater along the length of the fibers compared to perpendicular directions, leading to *anisotropic diffusion*. Thus, the diffusion signal will be weakest along the axis that most closely matches the orientation of the local white matter fibers, and stronger in perpendicular directions. By measuring diffusion along many different axes, and then rendering a 3D model of water displacement within each voxel, we can estimate microstructural properties of the tissue and the trajectory of the white matter fibers in each voxel (Basser et al., 1994; Basser & Pierpaoli, 1996). An illustration of these concepts is provided in **Figure 1.8**, adapted from Rokem et al. (2017).

Data Acquisition and Imaging Artifacts. In order to estimate the 3D shape of diffusivity in each voxel, a separate diffusion-weighted image volume will need to be created for each measured diffusion direction. Measuring more directions provides greater angular resolution and improves our ability to model crossing and curving white matter fibers, but it increases the total scan time. Common models used to approximate 3D diffusivity include the tensor model (Alexander et al., 2007; Basser et al., 1994), and the constrained spherical deconvolution (CSD) model (Tournier et al., 2007, 2008, 2012).

Several considerations must be taken into account to improve data quality and to avoid artifacts. Common artifacts in dMRI data include *image blurring, susceptibility artifacts,* and *motion artifacts*. Blurring artifacts result from both *signal loss*, as the diffusion signal decreases during acquisition time, and from *partial volume effects*, where a voxel may contain two or more different tissues that have differences in magnetic properties. Susceptibility artifacts, which appear as stretching, warping, or hyperintensities in the image, are also a direct result of large differences in magnetic properties between neighboring tissue types. Susceptibility artifacts are particularly problematic when imaging the OFC and olfactory brain areas, which sit adjacent to air-filled sinus cavities. The rather large difference in magnetic susceptibility between the brain tissue and the sinus cavity leads to artifacts so severe that the data from these regions is often uninterpretable. Ensuring a short echo time (the time elapsed between exciting the tissue with a radiofrequency (RF) pulse and reading out the resulting signal in the RF coil) during scanning is imperative to preserving signal in these regions, and can reduce the severity of blurring and susceptibility artifacts. In addition, dMRI protocols are particularly sensitive to subject motion since the acquisition of several direction-weighted volumes is required. Excessive motion will

make co-registration of the final images difficult, and the fitted 3D diffusion model may be noisy or corrupted.

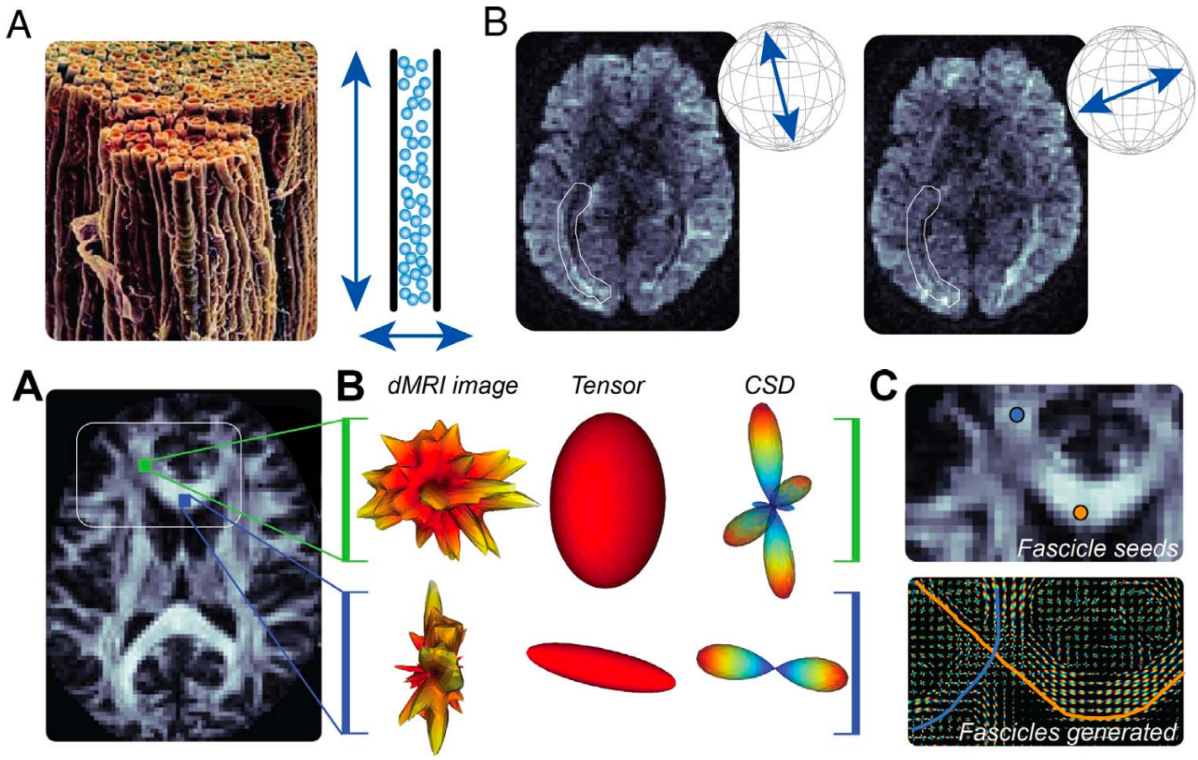

Figure 1.8. Diffusion magnetic resonance imaging and tractography. Top row; A. An electron micrograph of the human optic nerve, a highly myelinated bundle of axons, and a cartoon illustration of the anisotropic diffusion in the nerve, with water more easily traveling along the length of the nerve than in perpendicular directions. **B**. Two diffusion-weighted volumes, measuring water diffusion along the axis illustrated in the adjacent spheres. Note how when the measured diffusion direction matches the trajectory of the optic radiation (outlined on the diffusion-weighted volumes in white), the voxels within that white matter pathway are dark (low signal). When the measured diffusion direction is perpendicular to the optic radiations, the voxels within that region are bright (high signal). **Bottom row; A.** An axial brain slice showing fractional anisotropy in the white matter. **B.** The diffusion signal, fitted tensor, and fitted CSD fiber orientation distribution function for a voxel with crossing white matter pathways (top row, green) and a voxel with only one white matter pathway (bottom row, blue). **C.** Top, two user-defined seeding regions. Bottom, Streamlines generated using tractography starting from each seeding region, overlaid on a map of CSD fiber orientation distribution functions. (Reproduced from Rokem, A., Takemura, H., Bock, A. S., Scherf, K. S., Behrmann, M., Wandell, B. A., ... & Pestilli, F. (2017). The visual white matter: The application of diffusion MRI and fiber tractography to vision science. *Journal of Vision*, *17*(2), 4-4. under Creative Commons License (https://creativecommons.org/licenses/by/4.0/legalcode)).

Tractography and Connectivity Measures. Once the 3D diffusion signal is approximated in each voxel, tractography algorithms can trace the probable trajectories of white matter fibers through the brain. Specific *seeding regions*, or starting points, may be defined by the user. Tractography algorithms then trace a continuous path from voxel to voxel based on the primary direction(s) of diffusion, and give *streamlines* as output. In *deterministic* algorithms, the direction of largest diffusion magnitude is always chosen; thus, given the exact same seeding region and tracking parameters, the exact same streamlines will be output every time. *Probabilistic* algorithms instead choose a direction based on a gaussian distribution around the largest diffusion direction(s), and will produce different streamlines every time. Deterministic algorithms are more conservative and less prone to false positives, and are better for reliably reconstructing the core trajectories of major white matter pathways with little noise. Probabilistic algorithms are better when the exact trajectory of white matter fibers is unknown. They can be used to model the entire possible spread of a white matter bundle's trajectory and cortical endpoints, but will likely include many false positives (Jeurissen et al., 2019; Tournier et al., 2012).

The most commonly used diffusion model is the *tensor* model (Alexander et al., 2007; Basser et al., 1994). This model can be fit with as few as six diffusion-weighted directions, and is thus very time efficient. The diffusion signal is modeled by a tensor with three orthogonal *eigenvectors*. The primary eigenvector λ_1 is assigned to the direction with the least restricted diffusion (lowest diffusion signal). The eigenvectors λ_2 and λ_3 are then assigned to the two orthogonal axes of λ_1. The tensor will be approximately sphere shaped in regions with isotropic diffusion, and cigar shaped in regions with a single major diffusion direction. The tensor model is useful for characterizing the local tissue microstructure, but falls short when performing

tractography, as it is incapable of modeling multiple white matter orientations within a single voxel. It is estimated that up to 90% of white matter voxels contain crossing fibers at 2.4mm resolution (Jeurissen et al., 2013). Fewer measured diffusion directions also means reduced angular resolution, so modeling curving fibers may be impeded.

Higher order models, such as *constrained spherical deconvolution* (CSD), have been developed to address the crossing fiber problem in tractography (Jeurissen et al., 2013; Tournier et al., 2007, 2008, 2012). CSD approximates a 3D fiber orientation density function (fODF), which allows for multiple diffusion directions to be modeled within a single voxel. This model more accurately accounts for crossing and curving white matter fibers, and reduces the incidence of *jumping* fibers. For instance, when tracking with the tensor model, if one of two crossing fibers has a higher degree of myelination or fasciculation, then its orientation will dominate the local signal. Streamlines approaching the crossing point from the smaller fiber structure will "jump" onto the more fasciculated fiber's path, producing anatomically inaccurate streamlines. In contrast, fODFs account for multiple fiber directions, and will enable streamlines tracking across the intersection. To properly fit a CSD model, however, a large number of diffusion directions is required, usually between 40 and 90 directions.

Interpreting Microstructure Data. One important application of the tensor model is the characterization of microstructural tissue properties. Four main measures can be calculated based on the tensor eigenvalues. *Mean diffusivity* is the average magnitude of diffusion along the three eigenvectors. *Axial diffusivity* is the magnitude of the largest eigenvector along the primary direction of diffusion, and *radial diffusivity* is the average magnitude of diffusivity along the two

smaller orthogonal eigenvectors. *Fractional anisotropy* is a scalar value between zero and one that represents the variability in diffusion magnitude between the three eigenvectors (Rokem et al., 2017). These measures correlate with properties of the underlying tissues, and can be used to characterize differences between subject groups, such as patients versus a control group. Mean diffusivity is dependent on the tissue type contained within the voxel. Typically, CSF has high mean diffusivity, gray matter has low mean diffusivity, and white matter has intermediary values (Pierpaoli et al., 1996). Within a white matter fiber group, decreasing axial diffusivity and increasing radial diffusivity has been associated with demyelination (Klawiter et al., 2011; Song et al., 2005). Fractional anisotropy is highest in voxels containing a large number of fibers that are all oriented in the same direction, such as the midline of the corpus callosum. It is correlated with myelination thickness and fiber density, and is lower in areas with large numbers of crossing fibers (Basser & Pierpaoli, 1996). Local fractional anisotropy values are known to change when anatomical changes take place, but the direction of change is dependent on the local tissue environment (Beaulieu et al., 1996; Frank, 2002). For example, in a voxel containing crossing fibers from both the corpus callosum and the corticospinal tract, the fractional anisotropy will be fairly low. If the corpus callosum degenerates, then the fractional anisotropy will increase as the diffusion signal becomes dominated by the corticospinal tract. However, for a voxel at the midline of the corpus callosum, the fractional anisotropy will decrease since there are no other competing fiber pathways, and the diffusion signal at this location is entirely dependent on the callosal fibers. Taken together, these four measures can provide a picture of the underlying white matter integrity, and can help to pinpoint regions whose properties correlate with individual perceptual differences (Allen et al., 2015; Dietrich et al., 2015; Genc et al., 2011;

Miao et al., 2013; D. Wang et al., 2013), practice and learning of behavioral tasks (Bengtsson et al., 2005; Blumenfeld-Katzir et al., 2011; Hofstetter et al., 2013; Sampaio-Baptista et al., 2013; Thomas & Baker, 2013), or regions with white matter or axonal degeneration (Duan et al., 2015; Hanekamp et al., 2021; Ogawa et al., 2014; Roosendaal et al., 2009; Yeatman et al., 2012).

1.2.4. Olfactory Perceptual Decline in Aging, aMCI, and AD

The olfactory system is profoundly affected by aging and dementia (Doty & Kamath, 2014; Mobley et al., 2014; Murphy, 2019). Only 6% of adults aged 50-59 exhibit olfactory impairments, but for adults aged 65-80, over 50% show deficits in olfactory functioning, and over 75% adults over age 80 are affected (Albers et al., 2015; Doty & Kamath, 2014). They are often unaware of their declining olfactory function, but the loss of olfactory perceptual acuity is associated with increased incidence of depression (Negoias et al., 2010) and overall higher mortality risk (Pinto et al., 2014; Wilson et al., 2011), with much of the difference attributable to odor-related incidents, such as failing to detect a gas leak or ingesting spoiled food. Olfactory deficits are even more profound in elderly adults who go on to develop amnestic mild cognitive impairment (aMCI) and Alzheimer's disease (AD) (Albers et al., 2020; Devanand et al., 2015; Djordjevic et al., 2008; Murphy, 2019; Wilson et al., 2007). Elderly adults with aMCI and AD are found to have impaired odor memory (Albers et al., 2020; Nordin & Murphy, 1996), perform poorly on odor identification tasks (Lafaille-Magnan et al., 2017; Wilson et al., 2007, 2011; Woodward et al., 2017), and have higher odor detection thresholds relative to cognitively normal adults (Doty et al., 1987; Murphy et al., 1990). Olfactory impairments have also been associated with carrying the apolipoprotein E (APOE) gene ε4 allele, a gene associated with an increased

risk for developing cognitive impairment and Alzheimer's disease (Handley et al., 2006; Josefsson et al., 2017; Oleson & Murphy, 2015; Olofsson et al., 2010). Olfactory impairments often precede the onset of more severe cognitive symptoms by a year or more (Bacon et al., 1998; Roberts et al., 2016; Schubert et al., 2008; Wilson et al., 2007). Simple olfactory identification tests may prove to be useful tools for early detection aMCI and AD.

Predictive Olfactory Perceptual Measures. Odor identification, odor memory, and odor detection threshold tests have been evaluated for their ability to detect and predict aMCI and AD (Murphy, 2019). Measuring pure olfactory ability is a difficult task, however. Olfactory identification and odor memory tests require intact olfactory sensory functioning, attention to the task, working memory, episodic memory, recognition memory, and semantic processes necessary to name an odor. Odor threshold tests are also quite a bit longer and more intensive than odor identification or memory tasks, and will require sustained attention and working memory over a longer testing period. However, the intricate links between olfaction, cognition, and memory may work in our favor, as simple olfactory identification tests may be used to probe for potential deficits across a broad range of cognitive functioning.

Odor threshold tests involve many trials arranged in a staircase procedure where a participant must identify a low-concentration target odorant amidst a set of "blank" distractor odors. Odor threshold tests have been found to predict which APOE ε4 carriers with aMCI* will be diagnosed with AD in the next year (Bacon et al., 1998). (*Called "Questionable AD" here; recruited participants had mild memory impairments but were still able to live independently.) Higher olfactory detection thresholds have also been shown to correlate with the severity of AD

symptoms (Doty et al., 1987; Murphy et al., 1990). Odor recognition memory tasks typically begin with exposure to a set of odorants, followed by a series of trials where participants must identify which odorants they have encountered already amidst additional new distractor odorants. Participants with aMCI* were also shown to have poor odor recognition memory (Nordin & Murphy, 1996). In a separate study, participants with AD were shown to perform worse than healthy controls on an odor memory test. These effects were stronger for APOE ε4 carriers. However, performance on a visual memory test was not significantly different depending on diagnosis or genotype (Gilbert & Murphy, 2004).

Odor identification tests are the simplest tests to administer. Each trial involves only a single odorant and a set of picture, word-form, or verbal multiple-choice response options that the participant must choose from to name the odorant. Several studies have found that odor identification is impaired in aMCI (Djordjevic et al., 2008; Nordin & Murphy, 1996; Roalf et al., 2017), and even worse in AD (Albers et al., 2015; Doty et al., 1987; Oleson & Murphy, 2015; Woodward et al., 2017). It has been estimated that 85-90% of patients with AD are impaired on olfactory identification tests (Woodward et al., 2017). Woodward et al. (2017) evaluated the ability of the University of Pennsylvania Smell Identification Test (UPSIT) to classify participants by healthy cognition, aMCI, and AD. They found that the UPSIT had a sensitivity and specificity of 74% and 71% for detecting aMCI compared to healthy controls, and a sensitivity and specificity of 88% and 71% for detecting AD compared to healthy controls. Several longitudinal studies have found that poor performance on odor identification tests predicts conversion from healthy cognition to aMCI, and from aMCI to AD (Roberts et al., 2016; Schubert et al., 2008; Wilson et al., 2007). Wilson et al. (2007), as part of the Rush Memory and

Aging Project, found that in a retirement home population of 589 participants (mean age 79.9) who were cognitively healthy at baseline, there was a 50% increase in risk for developing aMCI with poor performance on the Brief Smell Identification Test (25th percentile or below) compared to performance at or above the 75th percentile. Schubert et al. (2008) tested 1920 participants (mean age 66.9) on the San Diego Odor Identification Test (SDOIT) as part of the Beaver Dam Epidemiological Study. They found that performance on the SDOIT was significantly associated with the development of cognitive impairment after 5 years (positive predictive value = 15.9%). The authors also noted that participants who performed well on the SDOIT were very unlikely to develop aMCI over the 5-year study period (negative predictive value = 97.2%). In another study, Roberts et al. (2016) found that performance on the Brief Smell Identification Test (BSIT) predicted progression from healthy cognition to aMCI, and progression from aMCI to AD over an average time period of 3.5 years. For participants with healthy cognition at baseline (N=1430), the hazard ratio for developing aMCI was 2.18 for scores in the lower quartile on the BSIT. For participants with aMCI at baseline (N=221), the hazard ratio for developing AD was 5.20 for scores in the lower quartile on the BSIT. A growing literature is thus lending credence to the use of simple olfactory identification tests as a tool in early detection of aMCI and AD.

Olfactory System Pathology in aMCI and AD. The olfactory sense is truly a limbic sense, in that it shares close, strong anatomic connectivity with the medial temporal lobe and orbitofrontal limbic regions (Catani et al., 2013). These limbic regions are also heavily involved in olfactory processing, and are particularly vulnerable to the amyloid plaque and tau tangle pathology observed in the progression of AD. Tau pathology first affect the entorhinal cortex, amygdala,

hippocampus, and parahippocampal cortex in Braak stages I-II. By Braak stages III-IV, the primary olfactory cortex, the olfactory bulbs, and the posterior orbitofrontal cortex are affected (Braak & Braak, 1991, 1995; Murphy, 2019; Price et al., 1991). In an autopsy study, the level of neurofibrillary tangles observed in the olfactory bulbs and tracts was found to match the level of tangles observed in medial temporal lobe limbic regions (Attems et al., 2005). All subjects diagnosed with AD were found to have Braak stages V-VI levels of neurofibrillary tangles in the olfactory bulbs, while those diagnosed with aMCI had Braak stages III-IV level pathology in the olfactory bulbs.

A growing literature suggests that olfactory impairments are significantly associated with tau pathology and with amyloid-beta pathology in the presence of tau pathology, but not with amyloid-beta pathology alone (Murphy, 2019; Tu et al., 2020). Two studies found no significant associations between scores on olfactory identification tests and amyloid-beta pathology, measured with amyloid-PET (Bahar-Fuchs et al., 2010; Buchanan et al., 2020). A third study found that amyloid burden assessed with amyloid-PET was significantly higher in participants with anosmia (total loss of smell) compared to normosmic (healthy olfaction) participants, but there was no statistically significant difference in amyloid burden between hyposmic (reduced olfactory ability) and normosmic participants (Vassilaki et al., 2017). Another study that investigated both CSF-tau and CSF-amyloid markers found that reduced olfactory identification scores were significantly associated with CSF tau pathology, and with CSF tau and amyloid pathology, but not with CSF amyloid pathology alone (Lafaille-Magnan et al., 2017). Another more recent study also found a significant negative association between performance on an olfactory identification test and the level of tau pathology measured by tau-PET imaging and

CSF lumbar punctures (Klein et al., 2021). The authors note that this association was primarily driven by participants who exhibited both amyloid-beta (assessed with amyloid-PET) and tau pathology. These results taken together suggest that amyloid-beta burden alone is not associated with olfactory impairments, so odor identification tests may not detect the presence of amyloid pathology. However, the degree of tau pathology appears to correlate more strongly with odor identification scores. Tau pathology is believed to precede cognitive and memory impairments in the progression of AD (Jack et al., 2010), so if simple olfactory identification tests are sensitive to the degree of tau pathology, they may prove to be useful tools for early detection and diagnosis of aMCI and AD.

1.3 Detailed Aims and Research Approach

1.3.1. Aim 1: Mapping the Striae and Microstructure of the Human Olfactory Tracts

The first aim of this thesis work was to identify and characterize the *in vivo* white matter projections of the lateral olfactory tract into primary olfactory cortex in the human, using diffusion magnetic resonance imaging (dMRI). This aim was broken up into four objectives. The first objective was to develop an optimized dMRI protocol that would allow clear imaging of the olfactory and orbitofrontal brain regions. The second objective was to design a tractography pipeline to extract streamlines from the lateral olfactory tracts, and characterize the tracts' endpoints in primary olfactory cortex. The third objective was to create a probabilistic atlas illustrating the location of the olfactory tracts in standardized MNI space. The last objective was to evaluate microstructural properties of the lateral olfactory tracts, including fractional anisotropy (FA) and mean diffusivity (MD), and their relationships with subjects' performance on olfactory perceptual tasks. The detailed methods and results of this aim are described in **Chapter 2** of this thesis, which was published in the Journal of Neuroscience in January, 2022; Echevarria-Cooper, S. L., Zhou, G., Zelano, C., Pestilli, F., Parrish, T. B., & Kahnt, T. (2022). Mapping the Microstructure and Striae of the Human Olfactory Tract with Diffusion MRI. *Journal of Neuroscience*, *42*(1), 58–68. https://doi.org/10.1523/JNEUROSCI.1552-21.2021

The Optimized dMRI Dataset. To image the olfactory tracts and their cortical endpoints with clarity, it was important to collect high-resolution dMRI data that was relatively free of susceptibility artifacts and motion artifacts. To prevent motion artifacts, we used individualized 3D-milled head stabilizers to essentially "head-fix" participants while in the scanner. These head

stabilizers were milled on the outside to fit snugly in the scanner coil, and on the inside to fit each individual subject based on 3D renderings of their head and face. To reduce susceptibility artifacts, we used a multi-shot echo planar imaging (EPI) technique (Siemens RESOLVE) to split data acquisition for each tissue slice into seven segments in the read-out direction. This allowed us to collect data for each slice at a very early echo time (TE), preventing the substantial signal decay in the olfactory brain regions that leads to susceptibility artifacts in typical single-shot EPI sequences. We chose to collect 90 diffusion weighted directions at b=1000 s/mm^2, providing high angular resolution and a better signal-to-noise ratio than would have been possible with higher b-values. Using these methods, we were able to collect data at 1.5mm isotropic resolution; a higher resolution than has been used before to image the olfactory tracts. With these methods, we collected dMRI data, T1-weighted and T2-weighted anatomical scans, and olfactory perceptual data (Sniffin' Sticks Threshold, Discrimination, and Identification scores) from N=25 subjects.

Tractography Approach and Olfactory Tract Cortical Connectivity. To generate streamlines in the olfactory tracts, we first fit a constrained spherical deconvolution (CSD) model to the diffusion data, capable of modeling crossing and curving fiber pathways within single voxels. We then used probabilistic tractography and seeded streamlines from the olfactory bulbs, a midpoint along the olfactory tracts just anterior to the anterior olfactory nucleus, and from the primary olfactory cortical regions. For one subject, we were able to generate continuous streamlines from the olfactory bulb to the primary olfactory cortex. For other subjects, there was a small area of signal drop-out near the sphenoid sinus preventing continuous tracking. In these

subjects, we used a b-spline interpolation method to infer the trajectory of the tracts between streamlines seeded from the olfactory bulb and streamlines seeded from the olfactory tract midpoint. We then recorded counts of how many streamlines existed between the olfactory tract midpoint and primary olfactory cortical regions, including the anterior olfactory nucleus, the olfactory tubercle, the frontal piriform cortex, the temporal piriform cortex, the amygdala, and the entorhinal cortex.

Creation of the Olfactory Tract Atlas. To create the probabilistic olfactory tract atlas, we first created binary voxel-wise masks of the olfactory tracts of each subject in native space. Any voxels traversed by olfactory tract streamlines were included in each subject's mask. These masks were then normalized to standardized MNI space, and averaged together to create a probabilistic atlas. This atlas is now freely available to the public on NeuroVault (https://neurovault.org/collections/ZTCWDMII/) and on BrainLife (https://brainlife.io/project/5ac2a489e182730027c55588).

Olfactory Perceptual Performance and Olfactory Tract Microstructure. FA and MD measures were evaluated and plotted for eight longitudinal segments of the olfactory tracts for each subject. For each of the eight segments, we evaluated correlations between the three olfactory perceptual measures (Threshold, Discrimination, and Identification scores) and the two diffusion microstructure measures (FA and MD). We then used a Bonferroni correction for multiple comparisons (8 segments x 3 perceptual measures) and evaluated the relationships between diffusion microstructure and olfactory perceptual performance in each segment.

1.3.2 Aim 2: Anatomical Parcellation of the Human Orbitofrontal Cortex using Diffusion MRI

The second aim of this thesis work was to characterize the anatomical connectivity of the *in vivo* human orbitofrontal cortex (OFC), using the same dMRI dataset from Aim 1. This aim was split into three objectives; first, to design a tractography pipeline that would allow us to extract streamlines and characterize the broad anatomical connections of the OFC; second, to use a k-means parcellation approach to identify OFC sub-regions with distinct anatomical connectivity; and third, to identify the regions of the OFC that have the strongest connectivity with the primary olfactory cortex. The detailed methods and results of this aim are described in **Chapter 3** of this thesis.

Tractography Approach and Evaluating OFC Connectivity. For this aim, we used anatomically constrained tractography (R. E. Smith et al., 2012). This probabilistic tractography approach seeds streamlines from the gray-matter white-matter interface (GMWMI), and only allows streamlines to have endpoints in the GMWMI or in the subcortical gray matter. We seeded 10 million streamlines from the whole brain GMWMI, and 10 million streamlines from the OFC GMWMI, producing 20 million streamlines for each subject's tractogram. Streamlines were then weighted using the Spherical deconvolution Informed Filtering of Tractograms (SIFT2) method (Smith et al., 2015) to prevent bias toward larger, long-range white matter pathways in the final connectome. A connectome matrix was then created, with the down-sampled 3mm isotropic voxels of the OFC GMWMI represented in the rows, and the down-sampled 3mm isotropic GMWMI and subcortical gray matter voxels represented in the columns. The degree of connectivity (sum of the SIFT2 streamline weights) between each pair of voxels was recorded.

K-Means Parcellation Approach and Identifying Distinct OFC Subregions. K-means parcellation was then used on the OFC connectome matrix to sort the rows of this matrix (corresponding to 3mm OFC GMWMI voxels) into distinct clusters based on connectivity with the rest of the brain. Parcellation was performed separately for the left and right hemispheres. We varied K from 2-6 to produce unique clustering solutions. Clustering was performed separately for each subject and hemisphere. We then created 3mm voxel masks in each subject's native T1 space of the OFC voxel cluster assignments for each value of K. These masks were then normalized to standardized MNI space. Each subject's normalized masks were then re-labeled according to similarity with a template subject (voxel cluster assignments remained the same for each subject's masks, only the cluster number labels were changed). These re-labeled masks were then averaged together to produce probability maps for each individual cluster, for each value of K. For K=2, K=3, and K=6 clustering solutions, we evaluated the connectivity patterns of each individual cluster across subjects, based on the weighted streamlines from the whole brain tractograms that intersected with voxels in each cluster.

1.3.3 Aim 3: Validation of the NIH Toolbox Odor Identification Test across Normal Cognition, amnestic Mild Cognitive Impairment, and Alzheimer's Disease

The third aim of this thesis work was to validate the National Institutes of Health Toolbox (NIHTB) Odor Identification Test for a population of adults over age 65 with normal cognition (NC), amnestic mild cognitive impairment (aMCI), and Alzheimer's disease (AD). Data for this aim were collected through several Alzheimer's Disease Research Centers (ADRCs) across the United States as part of the Assessing Reliable Measurement in Alzheimer's

Disease and cognitive Aging (ARMADA) project (Weintraub et al., 2022), and included N=389 participants (NC, N=248; aMCI, N=79; AD, N=62). This aim was split into three objectives. The first objective to evaluate differences in performance on the Odor Identification Test across diagnostic categories (NC, aMCI, and AD), sex, and age. The second objective was to determine how well the Odor Identification Test is able to classify participants with aMCI compared to participants with NC. The last objective was to evaluate whether performance on the Odor Identification test is significantly different across three special interest measures, including AD biomarker status (positive versus negative), APOE ε4 allele carrier status (positive versus negative), and across NC age groups (ages 65-84 versus ages 85+). The detailed methods and results of this aim are described in **Chapter 4** of this thesis.

Evaluating Odor Identification Performance across Age, Sex, and Diagnosis. Summary statistics were evaluated to determine the mean, standard deviation, and spread of odor identification scores across sex (male versus female) and diagnostic categories (NC, aMCI, and AD). Main effects and interactions between diagnostic categories, age, and sex on odor identification scores were evaluated using multiple linear regression.

Predictive Value of the Odor Identification Test for aMCI. For this analysis, we included only participants with NC and aMCI. A logistic regression model was used to evaluate whether lower odor scores were significantly associated with having aMCI. A receiver operating characteristic (ROC) curve was then plotted based on the fitted values of the logistic regression model, and the

area under the curve (AUC) was calculated to determine how well odor identification scores can classify NC versus aMCI.

Odor Identification Performance across Special Interest Measures. Here, we evaluated differences in odor identification scores based on AD biomarker status (positive versus negative), APOE ε4 allele carrier status (positive versus negative), and across age groups within the NC subset of participants (ages 65-84 versus ages 85+). Three-way analyses of covariance (ANCOVAs) were used to evaluate differences in odor identification scores, age, and sex across groups for each of the three special interest measures. The subset of participants included in the AD biomarker analysis were any participants that had a lumbar puncture to evaluate tau levels in the cerebrospinal fluid or that had PET imaging to evaluate amyloid plaque levels. Participants were classified as "positive" if they were indicated as meeting AD biomarker thresholds on at least one of these two tests, and "negative" if they were indicated as not meeting AD biomarker thresholds on one or both of these tests. In total, there were N=48 participants with positive biomarker tests, and N=117 participants with negative biomarker tests. For the APOE analysis, participants were placed in the "positive" group if they had at least one ε4 allele, and in the "negative" group if they had no ε4 alleles. In total, there were N=177 participants with at least one ε4 allele, and N=98 participants with no ε4 allele. For the analysis across age groups in the Normal Cognition diagnostic category, there were N=152 participants aged 65-84 and N=96 participants aged 85+.

Chapter 2: Mapping the Microstructure and Striae the Human Olfactory Tract with Diffusion MRI

This chapter is adapted from a manuscript published in *The Journal of Neuroscience* in January 2022 (Echevarria-Cooper et al., 2022).

2.1. Abstract and Significance

The human sense of smell plays an important role in appetite and food intake, detecting environmental threats, social interactions, and memory processing. However, little is known about the neural circuity supporting its function. The olfactory tracts project from the olfactory bulb along the base of the frontal cortex, branching into several striae to meet diverse cortical regions. Historically, using diffusion magnetic resonance imaging (dMRI) to reconstruct the human olfactory tracts has been prevented by susceptibility and motion artifacts. Here, we used a dMRI method with readout segmentation of long variable echo-trains (RESOLVE) to minimize image distortions and characterize the human olfactory tracts *in vivo*. We collected high-resolution dMRI data from 25 healthy human participants (12 male and 13 female) and performed probabilistic tractography using constrained spherical deconvolution (CSD). At the individual subject level, we identified the lateral, medial, and intermediate striae with their respective cortical connections to the piriform cortex and amygdala, olfactory tubercle, and anterior olfactory nucleus. We combined individual results across subjects to create a normalized, probabilistic atlas of the olfactory tracts. We then investigated the relationship between olfactory perceptual scores and measures of white matter integrity, including mean diffusivity (MD). Importantly, we found that olfactory tract MD negatively correlated with odor

discrimination performance. In summary, our results provide a detailed characterization of the connectivity of the human olfactory tracts and demonstrate an association between their structural integrity and olfactory perceptual function.

This study provides the first detailed *in vivo* description of the cortical connectivity of the three olfactory tract striae in the human brain, using diffusion magnetic resonance imaging (dMRI). Additionally, we show that tract microstructure correlates with performance on an odor discrimination task, suggesting a link between the structural integrity of the olfactory tracts and odor perception. Lastly, we generated a normalized probabilistic atlas of the olfactory tracts that may be used in future research to study its integrity in health and disease.

2.2. Introduction

Human olfaction supports many important cognitive and behavioral functions, including food-intake, social interactions, memory, and detecting threats in the environment (Gottfried, 2010; McGann, 2017). Despite its importance, much of our knowledge about the connectivity of olfactory bulb afferents is inferred from work in nonhuman animals. *Post mortem* studies in humans suggest that the olfactory tracts are comprised of parallel afferents that split into three separate striae (lateral, medial, and intermediate) before meeting primary olfactory cortex, but their precise targets remain difficult to identify (Allison, 1954; Boniface M. Kavoi & Hassanali Jameela, 2011; Mark et al., 1994; Rose, 1927). In rats and mice, axon tracing reveals projections to the anterior olfactory nucleus (AON), anterior and posterior piriform cortices, the olfactory tubercle (OT), the amygdala (AMY), periamygdaloid cortex, and lateral entorhinal cortex (EC) (Haberly & Price, 1978a, 1978b; Miyamichi et al., 2011; Schwob & Price, 1984; Scott et al.,

1980; White, 1965). In macaque monkeys, projections identified with axon tracing methods appear to be highly conserved and innervate homologous primary olfactory regions, but connectivity to the EC is confined only to its most rostral aspect (Carmichael et al., 1994). Homologous cortical regions have been identified in humans (Allison, 1954; Boniface M. Kavoi & Hassanali Jameela, 2011; Crosby & Humphrey, 1941; Rose, 1927; Uyematsu, 1921), including the AON, frontal piriform cortex (FPC), temporal piriform cortex (TPC), OT, AMY, and EC. Allison (1954) identified the striae of the *post mortem* human olfactory tracts with silver staining, and concluded that they reached each of these regions with the exception of EC. However, precise replication of these findings using *in vivo* methods is still needed.

In vivo investigations of the human olfactory tracts have only recently become possible with innovations in dMRI (Fjaeldstad et al., 2017; Milardi et al., 2017; Skorpil et al., 2011). However, several limitations have so far prevented a comprehensive mapping of their connectivity. First, magnetic susceptibility differences between brain tissue and air in the sinus cavities cause severe artifacts, warping the final image and obscuring the olfactory tracts. Second, dMRI scans are particularly sensitive to head motion. Third, the branching and highly curved olfactory tract striae pose problems for the traditional diffusion tensor model, which cannot model multiple fiber orientations within a single voxel (Tournier et al., 2007, 2012).

In the present study, we sought to overcome these challenges by using recent advances in dMRI technology. Most importantly, we used a method with readout segmentation of long variable echo-trains (RESOLVE) to segment data acquisition in the read-out direction and achieve short echo times (TEs), allowing high-resolution scanning with relatively few susceptibility artifacts (Porter & Heidemann, 2009). We also used customized head stabilizers to

"head-fix" participants during scanning (Power et al., 2019). Finally, to discern the branching striae, we performed probabilistic tractography using the constrained spherical deconvolution (CSD) model, capable of fitting multiple fiber orientations within each voxel (Tournier et al., 2007, 2012).

Using these optimized methods, we have identified the three striae of the olfactory tracts and characterized their connectivity with primary olfactory cortex in 25 healthy human subjects. Further, we found a correlation between the microstructural integrity of the olfactory tracts and olfactory perceptual function. These results provide novel insight regarding human olfactory tract connectivity, which has historically been difficult to discern. They also provide the first step toward investigating in vivo microstructure-function relationships in the human olfactory system, which may be useful for studying olfactory tissue integrity in clinical populations. Specifically, olfactory dysfunction may serve as an early harbinger of neurodegenerative diseases such as Parkinson's (Fullard et al., 2017; M. Witt et al., 2009) or Alzheimer's disease (Murphy, 2019; Peters et al., 2003), and in demyelinating diseases such as multiple sclerosis (Carotenuto et al., 2019; Lucassen et al., 2016). Identifying specific patterns of tissue degeneration in conjunction with olfactory perceptual testing may help dissociate different degenerative diseases in their prodromal stages.

2.3. Materials and Methods

Subjects. A total of 27 right-handed subjects (14 male and 13 female; age: mean 25.76 +/- standard deviation 4.01 years), with no neurologic disorders, psychiatric disorders, or MRI contraindications, were enrolled in this study. Two subjects, both males, were excluded from

final analyses because they did not complete the MRI scanning protocol. The study was approved by the Northwestern IRB (STU00098371), and all subjects gave written informed consent for participation.

Study design. Subjects visited the lab two times (**Figure 2.1A**). During visit 1, they completed three olfactory perceptual tests (threshold, discrimination, and identification) and were fitted for a personalized head stabilizer. During visit 2, participants repeated the olfactory threshold test, and underwent MRI scanning. Visit 1 and visit 2 were separated by 2–35 days (mean 15.68 +/- standard deviation 9.51).

Olfactory perceptual testing. During visit 1, subjects underwent olfactory perceptual testing using the Sniffin' Sticks threshold (n-butanol), discrimination, and identification tests (Rumeau et al., 2016), administered in the listed order. During visit 2, subjects repeated the olfactory threshold test, and the two threshold scores were averaged. Scores on each test range from 0 (worst) to 16 (best), with anosmic thresholds at scores of T = 1.0, D = 8, and I = 8. All subjects scored above anosmic thresholds for all three tests. We computed the composite threshold + discrimination + identification (TDI) score by adding the mean threshold score, the discrimination score, and the identification score (**Figure 2.1B**).

Personalized head stabilizers. Subjects wore personalized head stabilizers to prevent head motion for the duration of MRI scanning (Power et al., 2019). 3D renderings of each subject's face and head were created using a handheld camera and the Caseforge iOS application. The

head stabilizers were 3D-milled to fit the subject's face and head on the inside and the shape of the MRI scanner coil on the outside. An example is shown in **Figure 2.1C**.

MRI data acquisition. During visit 2, subjects underwent MRI scanning on a 3T Siemens Prisma scanner with a 64-channel head-neck coil. We collected a set of diffusion-weighted images, a T1-weighted image, and a T2-weighted image. Subjects wore their customized head stabilizers for the duration of the scans.

We used a high-resolution (1.5 mm isotropic) RESOLVE dMRI scan with seven readout segments (Porter & Heidemann, 2009) to collect the diffusion-weighted images. This sequence is different from typical single-shot echo planar imaging (SS-EPI) techniques in that it splits data collection into seven segments in the read-out direction and re-excites the tissue before each segment with a new radio frequency pulse. The readout segments are combined in the end to produce the full image. The shorter readout segment allows for a shorter TE than is possible in SS-EPI sequences. However, it takes more time to acquire a complete dataset, based on the number of segments. We also included a navigator echo to monitor between-segment motion, so that volumes were re-acquired if the motion was excessive (Porter & Heidemann, 2009). In addition, we used simultaneous multi-slice acquisition (Nunes et al., 2006) to allow for improved spatial coverage required when using such small voxels. This sequence was designed based on extensive pilot testing to provide high-resolution images with reduced blurring, and largely free of susceptibility artifacts compared with conventional SS-EPI techniques (**Figure 2.1D**). Imaging parameters were as follows: 92 slices; field of view (FoV) = 240 mm; matrix size = 240 x 240 x 138 mm; 90 diffusion-weighted directions at b = 1000 s/mm^2; 12 interspersed b0

volumes; phase encoding = A > P; TE1 (image echo) = 61 ms; TE2 (navigator echo) = 98 ms; repetition time (TR) = 6250 ms; flip angle = 180°; bandwidth = 897 Hz/Px, multiband factor = 2. The scan time for this RESOLVE dMRI sequence was approximately 1 hour and 30 minutes. An oblique slice angle (~30° relative to the AC–PC plane) was used to further reduce susceptibility artifacts (Weiskopf et al., 2006).

The parameters for the two anatomic scans were as follows: T1-weighted, 1.0 mm isotropic, TE = 2.94 ms, TR = 2300 ms, flip angle = 9°, FoV = 256 mm, matrix size = 256 x 256 x 176 mm; phase encoding = A > P, bandwidth = 240 Hz/Px; T2-weighted (Siemens ZOOMit protocol), 0.5 mm isotropic, TE=125ms, TR=1000ms, flip angle=100°, FoV=160 mm, matrix size=82 x 160 x 72 mm, phase encoding = A > P, bandwidth = 256 Hz/Px. The T2-weighted image covered the ventral frontal lobes and temporal poles, including the olfactory bulbs, orbitofrontal cortex, and lengths of the olfactory tracts. The scan duration was 5min for the T1-weighted image and 7min for the T2-weighted image.

MRI data preprocessing. All MRI data were converted to the Nifti file type using MRIcron's dcm2niix function (X. Li et al., 2016). The diffusion MRI data were corrected for motion and eddy current artifacts using FSL's function, eddy_openmp (Jenkinson et al., 2012; S. M. Smith et al., 2004; Woolrich et al., 2009). The T1-weighted and T2-weighted images were co-registered to the native diffusion space using SPM12 (SPM12 Software, 2014). All diffusion model fitting and tractography were performed in the native diffusion space to prevent registration-related errors in the alignment of the b-vectors with the diffusion-weighted data. MRtrix2 functions were used to fit the tensor model (dwi2tensor), create FA (tensor2FA) and eigenvector maps

(tensor2vector), estimate the fiber response function for use in spherical deconvolution (estimate_response), and fit the CSD model (csdeconv; lmax=8) (Tournier et al., 2007, 2008, 2012). The MRtrix3 function tensor2metric was used to generate mean diffusivity (MD) maps based on the estimated diffusion tensors (Basser et al., 1994; Tournier et al., 2019; Westin et al., 1997). The CSD model was used to perform probabilistic fiber tractography, using the MRtrix2 function streamtrack SD_PROB (Tournier et al., 2012), to delineate the paths traversed by the olfactory tracts.

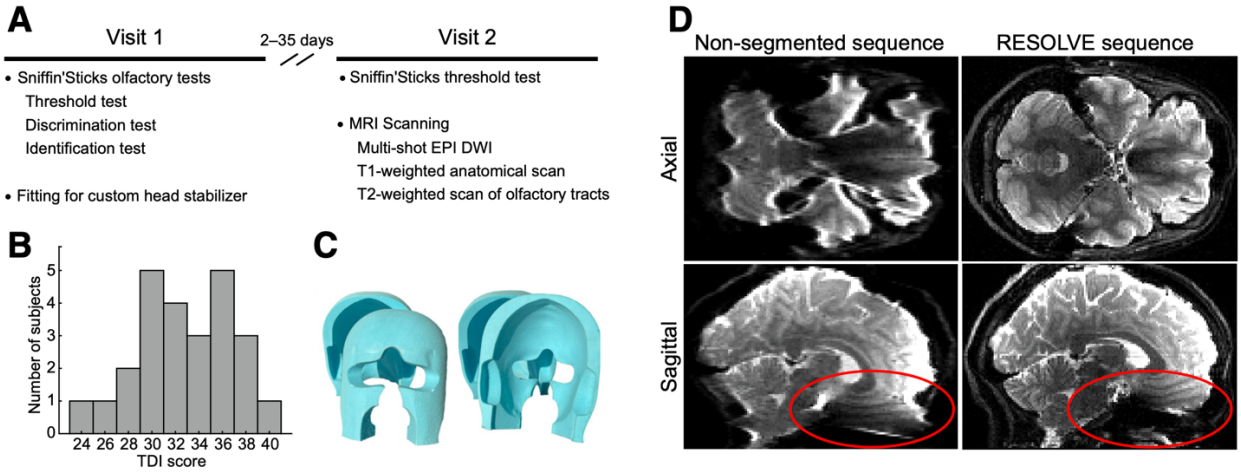

Figure 2.1. A, **Study timeline.** DWI = diffusion weighted imaging. **B**, Histogram of the summed TDI (Threshold, Discrimination, and Identification) scores across subjects. **C**, Example of a customized 3D-milled head stabilizer for preventing head motion during MRI scanning. **D**, Comparison of susceptibility artifacts and blurring at 1.5-mm isotropic resolution between a non-segmented Single-Shot Echo Planar Imaging (SS-EPI) sequence and the multi-shot Readout Segmentation of Long Variable Echo trains (RESOLVE) sequence (collected from the same pilot subject). Note that severe artifacts present in orbitofrontal regions in the non-segmented EPI images are absent in the RESOLVE images (red).

Regions of interest (ROIs). Olfactory ROIs were defined for use in tractography segmentation (**Figure 2.2**) using ITK-SNAP (Yushkevich et al., 2006). The ROIs were drawn for the left and right hemispheres separately on each individual's anatomic images. The olfactory bulbs were

outlined on each individual's 0.5-mm resolution T2-weighted image. Using both the 0.5-mm resolution T2- weighted and 1.0-mm resolution T1-weighted images, ROIs were placed in a midpoint region of the olfactory tracts in both hemispheres. This midpoint ROI was placed in the olfactory sulcus, anterior to the position of the olfactory trigones, and posterior and superior to the level where the optic nerves traverse below the olfactory sulci. In some subjects, a portion of the olfactory tract is visible at this location in the anatomic images and in the FA maps. Several cortical and subcortical ROIs were defined based on established targets of the olfactory tracts in rodents and nonhuman primates (Carmichael et al., 1994; Haberly & Price, 1978a, 1978b; Miyamichi et al., 2011; White, 1965). These regions included the AON, OT, FPC, TPC, AMY, and EC. These regions were defined for each subject, separately in the left and right hemispheres based on a published atlas (Mai et al., 2015), architectonic studies (Ongür et al., 2003a; Öngür & Price, 2000), and the results of an olfactory functional network study (Zhou et al., 2019). To generate probabilistic atlases for these olfactory ROIs, each subject's ROIs were normalized to MNI space and binarized, and the normalized ROIs were averaged across subjects, resulting a probability value for each voxel. These ROI atlases are available on NeuroVault (https://neurovault.org/collections/ZTCWDMII/) and BrainLife (https://brainlife.io/project/5ac2a489e182730027c55588).

Probabilistic tractography. The olfactory tracts were defined for each subject, separately in each hemisphere, with probabilistic tractography based on the CSD model, using the streamtrack SD_PROB algorithm (Lmax = 8, FA threshold = 0.1, curvature threshold = 1.5 mm) from MRtrix2 (Tournier et al., 2007, 2008, 2012). Three sets of fiber groups were generated in each

hemisphere (for details, see Results). For each fiber group, probabilistic tractography continued until 1000 streamlines were generated meeting the defined conditions. Brain masks were not used to constrain tracking, since most brain masking algorithms exclude the olfactory bulbs and probable locations of the olfactory tracts, because of the signal quality of conventional diffusion-weighted images. Fiber groups were then cleaned using the dtiCleanFibers and AFQ_removeFiberOutliers functions from Vistasoft and the Automated Fiber Quantification (AFQ) package (Pestilli et al., 2014; Yeatman et al., 2012). These functions remove any streamlines that are more than four standard deviations longer than the mean streamline length, or that are more than four standard deviations outside of the mean Gaussian distance from the "core" of the fiber tract, as defined in Yeatman et al. (2012).

In most subjects, the olfactory bulbs could not be continuously linked to cortex because of a small area of signal drop out near the sphenoid sinus. In these subjects, we used the MATLAB function cscvn (version R2020b) to produce natural cubic spline curves (Lee, 1989) to interpolate the path of the olfactory tracts across this gap, separately for each subject in each hemisphere. The five most posterior points (1 mm) of fiber group 1 and the five most anterior points (1 mm) of fiber group 2 were excluded, since the streamlines tended to splay out away from the core of the fiber tract near the ends. The next five most posterior points (1 mm) of the streamlines in fiber group 1 and the next five most anterior points (1 mm) of the streamlines in fiber group 2 were used as control points for interpolation.

In all subjects, the midpoint seeding regions of the olfactory tracts were linked to primary olfactory cortical ROIs via continuous streamlines, in fiber groups 2 and 3. These fiber groups were used to analyze connectivity between the olfactory tracts and individual cortical ROIs.

Connectivity was noted as present if streamlines existed connecting the seeding region in the olfactory tracts with the cortical ROI in question. Connection density values were calculated for each connection to describe the strength of each connection, defined as the number of streamlines connecting the seeding region to each cortical ROI, divided by the volume (mm^3) of that cortical ROI.

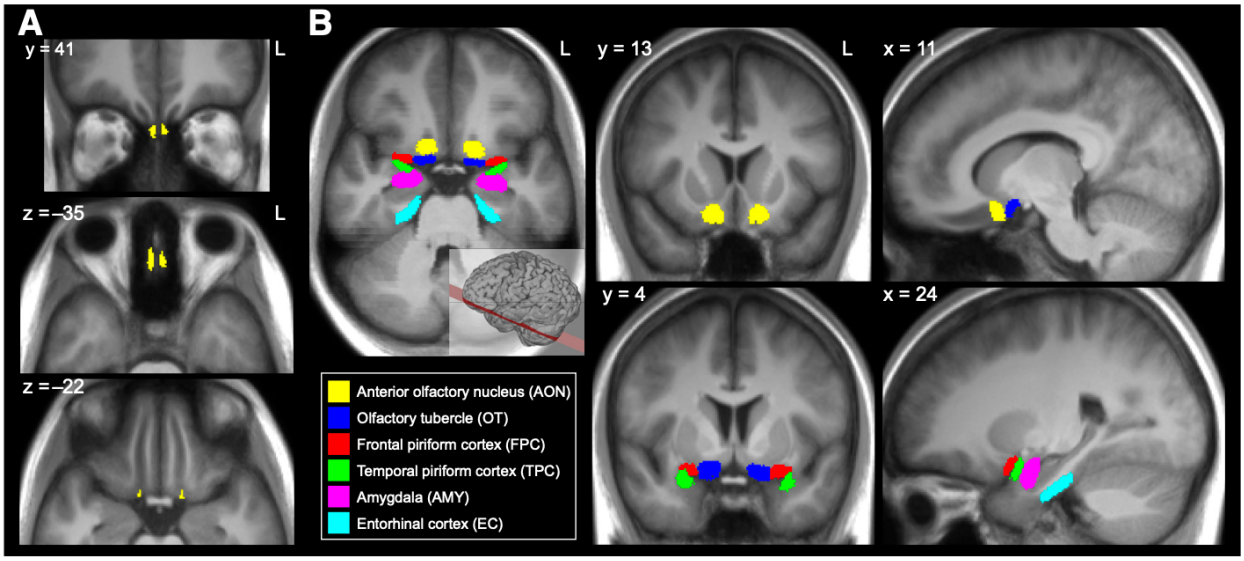

Figure 2.2. Atlases of the Regions of Interest in MNI space. **A**, Seed regions of the olfactory bulb (top and middle) and midpoint of the olfactory tract (bottom) used for segmentation of the olfactory tracts. **B**, Masks of the primary olfactory regions that were used as inclusionary regions investigated for connectivity with the olfactory tracts. Only voxels overlapping in .20% of sub- jects are shown for illustration. Masks are overlaid on a mean image of all subjects' MNI-normalized T1 images.

Generation of the olfactory tract atlas. We created binary masks in each subject's native space to index voxels traversed by the olfactory tracts, using the cleaned, interpolated, and combined fiber groups. We then normalized these masks into Montreal Neurological Institute (MNI) space using SPM12 (SPM12 Software, 2014) with deformation fields estimated based on the T1-weighted images. We averaged the masks in MNI space across subjects to create a probabilistic atlas of the olfactory tracts, where each voxel's value between 0 and 1 reflects the proportion of subjects in

which olfactory tract streamlines were present at that position. We truncated the posterior boundary of the olfactory tract atlases at MNI Y = –3, just posterior to the point where the lateral and medial striae enter cortex. The anterior boundary is located at MNI Y = 53, at the anterior edge of the olfactory bulbs. This atlas is publicly available on NeuroVault (https://neurovault.org/collections/ZTCWDMII/) and on BrainLife (https://brainlife.io/project/5ac2a489e182730027c55588).

Diffusion microstructure profiles of the olfactory tracts. We conducted analyses of local olfactory tract microstructural characteristics in individual subjects, using our probabilistic olfactory tract atlas. Fractional anisotropy (FA) and mean diffusivity (MD) estimates in a white matter tract of interest are known to be affected by partial volume effects with surrounding anatomy, inhomogeneities in the magnetic field, and noise. Local measures of FA and MD can thus be plotted along a white matter tract to account for these effects, and this method has been shown to produce replicable characteristic curves for specific white matter tracts across healthy subjects (Yeatman et al., 2012). Here, we used a similar approach in the olfactory tracts.

We first divided the olfactory tract atlas into eight equally-spaced anterior-posterior segments (width = 6.25 mm) in each hemisphere, in MNI space. We reasoned that averaging FA and MD measures within segments of this size would help to reduce noise while preserving local information about field inhomogeneities and neighboring anatomic features. We then then transformed the segmented masks into each subjects' native diffusion space, using SPM12 (SPM12 Software, 2014) with inverse deformation fields estimated based on the T1-weighted images. For each subject, we calculated voxel-wise values for FA and MD in each segment and

weighted these values by the probability values in the olfactory tract atlas. We then calculated the mean of the weighted FA and MD measures within each segment, for each subject.

Statistical analysis. To test correlations between microstructure measures and olfactory perceptual ability, we regressed the FA and MD values in each of the eight segments (averaged across hemispheres) against scores on each of the Sniffin' Sticks tests (threshold, discrimination, and identification). We controlled for potential effects of age and sex, by including these variables as covariates in multiple linear regression models. Bonferroni correction was used to correct for multiple comparisons (eight segments x three measures).

2.4. Results

Healthy subjects [N = 25, 13 female, age 24.98 6 4.38 (mean 6 SD) years] participated in olfactory perceptual testing and MRI scanning (**Figure 2.1A**). Summed Sniffin' Sticks TDI scores are shown in **Figure 2.1B**. During MRI scanning, subjects wore individualized head stabilizers (**Figure 2.1C**) to prevent motion. MRI scanning included 1.0-mm isotropic T1-weighted and 0.5-mm isotropic T2-weighted structural MRI scans, used to identify anatomic ROIs, and 1.5-mm isotropic dMRI RESOLVE scans. We chose the dMRI RESOLVE sequence based on extensive pilot testing in our lab to produce high-resolution images with reduced blurring, and largely free of susceptibility artifacts compared with conventional SS-EPI dMRI techniques (**Figure 2.1D**).

Tractography and connectivity results. We reconstructed olfactory tract streamlines in each subject using probabilistic tractography based on the CSD model (Tournier et al., 2007, 2012). In each hemisphere, we defined ROIs for each individual subject, including the olfactory bulb, several primary olfactory cortical regions (including the AON, FPC, TPC, OT, AMY, and EC), and a midpoint region of the olfactory tract located in the olfactory sulcus (**Figure 2.2**). We generated three sets of fiber groups in each hemisphere with the following conditions: (1) streamlines were seeded from the olfactory bulbs; (2) streamlines were seeded from the olfactory tract midpoint ROI, and olfactory cortical regions including the AON, FPC, TPC, OT, AMY, and EC were defined as inclusionary ROIs; (3) streamlines were seeded from the cortical ROIs listed in the second condition, and the olfactory tract midpoint ROI was defined as an inclusionary ROI. In all three conditions, exclusionary ROIs were placed to prevent streamlines from crossing the midline or entering the optic nerves, gyrus rectus, orbitofrontal cortex, or the surrounding cerebrospinal fluid. Fiber groups were cleaned to remove noisy and erroneous streamlines (see Materials and Methods), and the resulting fiber groups contained (mean +/- standard deviation) 952.64 +/- 24.98, 879.64 +/- 40.05, and 853.60 +/- 37.73 streamlines in the left hemisphere for fiber groups 1–3, respectively. The number of streamlines was 963.64 +/- 23.49, 873.48 +/- 30.75, and 864.92 +/- 31.91 for groups 1–3 in the right hemisphere. Fiber groups 2 and 3 were used to evaluate the connectivity of the olfactory tracts with primary olfactory cortex.

Most importantly, bilateral continuous streamlines between the olfactory bulb and primary olfactory cortex were found in one subject (**Figure 2.3**). In two other subjects, fiber group 1 overlapped with fiber groups 2 and 3 in the right hemisphere only. In many subjects, a small area of signal dropout near the sphenoid sinus prevented continuous tracking across the

entire length of the olfactory tracts. In these subjects, fiber group 1 was separated from fiber groups 2 and 3 by a small gap. The length of fiber group 1, measured from the olfactory bulbs to the point of signal drop out, was: left hemisphere, mean 24.04 mm +/- standard deviation 4.81 mm; and right hemisphere, mean 27.12 mm +/- standard deviation 6.99 mm. The Euclidean distances between the posterior end of fiber group 1 and the anterior-most end of fiber groups 2 and 3 were: left hemisphere, mean 10.1 mm +/- standard deviation 4.1 mm; and right hemisphere, mean 8.5 mm +/- standard deviation 4.7 mm. In these subjects, we used a natural cubic spline interpolation method (Lee, 1989) to estimate the path of the olfactory tracts across the gap (**Figure 2.4**).

Across subjects, streamlines in fiber group 1 projected posteriorly from the olfactory bulbs, following along the length of the olfactory sulci. Anterior projections of streamlines in fiber groups 2 and 3 followed along the olfactory sulcus and passed superiorly to the optic nerves before connecting to streamlines in fiber group 1, either directly or via interpolated segments. Posterior portions of streamlines in fiber groups 2 and 3 branched near the level of the optic chiasm to form the lateral, medial, and intermediate striae. Streamlines forming the intermediate striae curved sharply superiorly, entering AON gray matter, while those forming the lateral striae curved sharply laterally to meet FPC gray matter, and those forming the medial striae curved sharply medially to meet OT gray matter (**Figure 2.3C**). Some streamlines of the lateral branch continued through the uncinate fasciculus to meet the TPC, and through temporal lobe white matter to meet AMY. Only one streamline identified in one subject reached the EC.

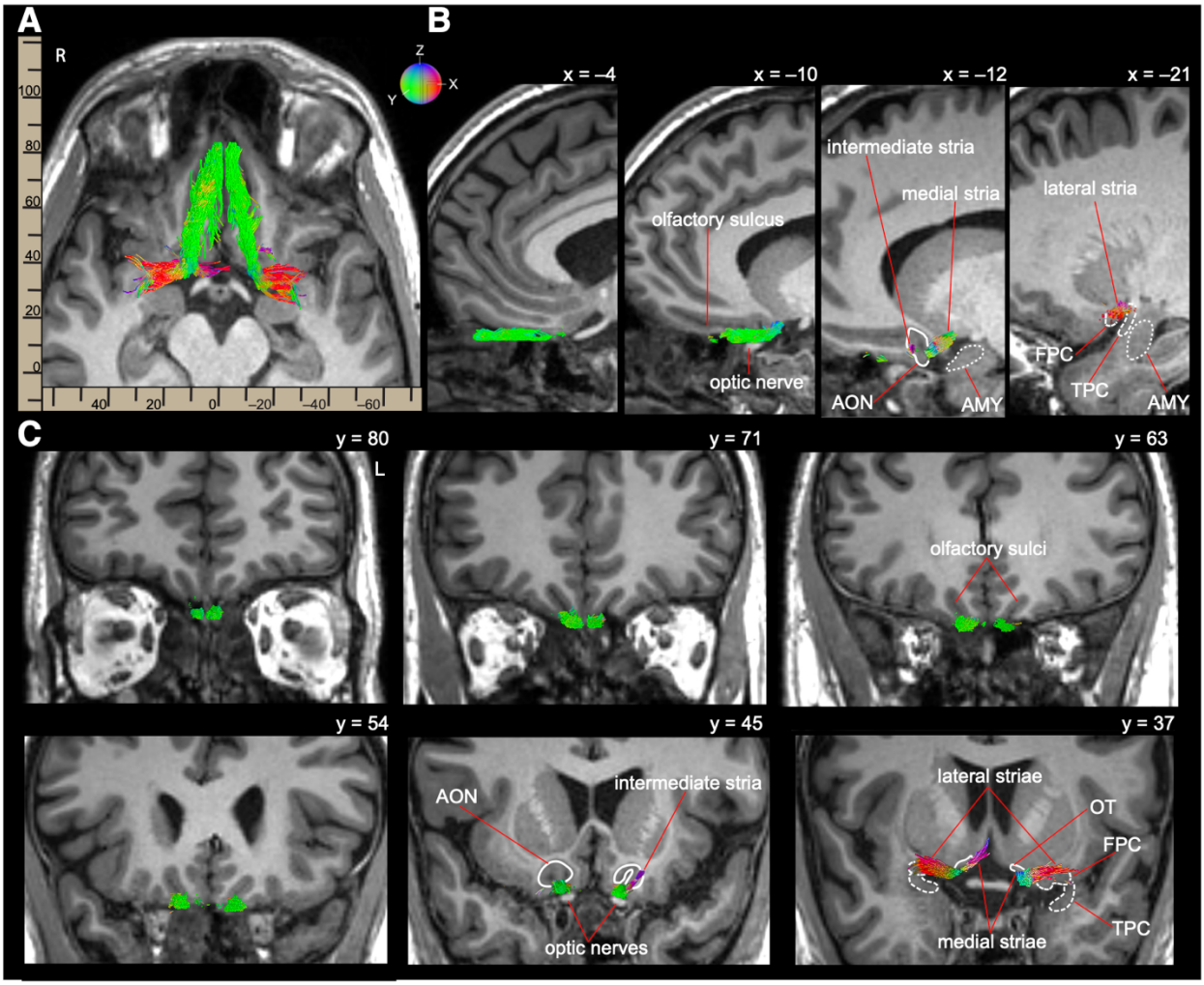

Figure 2.3. **Continuous streamlines connecting the olfactory bulbs with primary olfactory cortex in one subject** (Table 2, row 4), overlaid on the subject's T1 image. **A**, 3D fiber groups overlaid on an axial slice. **B**, Sagittal views of the fiber groups in the left hemisphere. **C**, Coronal views of the fiber groups indicating the trajectory of the olfactory tracts from bulb (y = 80) to the inter- mediate stria (left hemisphere, y = 45), and the medial (right hemisphere) and lateral striae (both hemispheres, y = 37). Red, green, and blue color scheme corresponds to lateral-medial (x), anterior-posterior (y), and superior-inferior (z) streamline trajectories, respectively. Primary olfactory cortical targets are labeled: AON, OT, FPC, TPC, AMY.

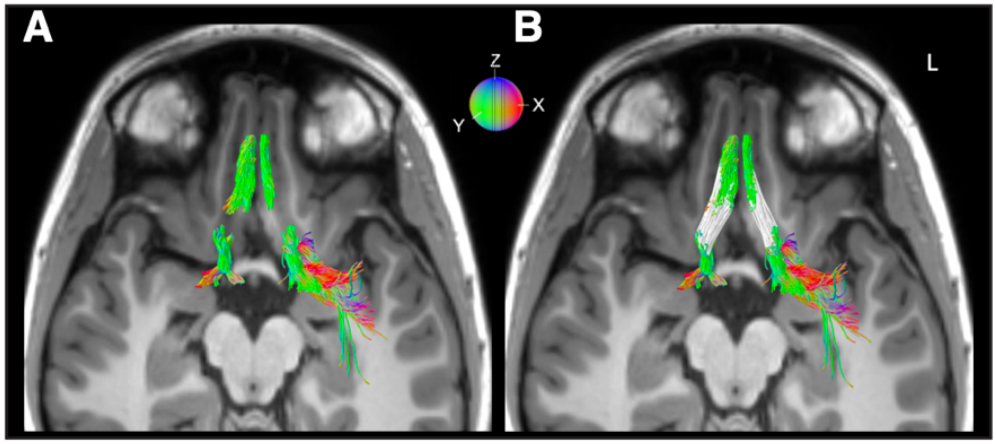

Figure 2.4. **Example of natural cubic spline interpolation in the lateral olfactory tracts**, overlaid on the subject's T1 image. **A**, Streamlines generated using probabilistic tractography, seeding in the olfactory bulb, olfactory tract midpoint, and cortical olfactory regions. **B**, The same streamlines as shown in **A**, with the interpolated streamlines included (white). Red, green, and blue color scheme corresponds to lateral-medial (x), anterior-posterior (y), and superior-inferior (z) streamline trajectories, respectively.

We quantified the connectivity of the olfactory tracts with each primary olfactory cortical region, defined as whether streamlines in fiber group 2 or 3 existed connecting the olfactory tract midpoint ROI with each cortical region. In all subjects, connectivity was present in at least one hemisphere between the olfactory tracts and the AON, the FPC, the TPC, and the OT. In 76% of subjects, connectivity with the AMY was also present in at least one hemisphere. Only one subject showed connectivity with the EC in the right hemisphere. Connection density, a measure of connection strength (Hagmann et al., 2008), was calculated for each connection by dividing the number of streamlines present by the volume (mm^3) of the target cortical ROI. Group connectivity and connection density results are listed in **Table 2.1.** Individual subjects' connectivity and connection density results are listed in **Table 2.2.**

Table 2.1. Connectivity and connection densities of the olfactory tracts.					
ROI	**Hemisphere**	**Streamlines (median)**	**Streamlines IQR (Q3 – Q1)**	**Connection density (mean +/– SEM)**	**Number of Subjects**
AON	Left	271	301	0.77 +/– 0.12	25
	Right	295	351	0.72 +/– 0.11	24
FPC	Left	104	247	0.89 +/– 0.16	22
	Right	15	54	0.22 +/– 0.07	19
TPC	Left	173	289	1.01 +/– 0.21	23
	Right	23	174	0.30 +/– 0.08	18
OT	Left	451	359	1.70 +/– 0.23	24
	Right	223	206	1.17 +/– 0.19	24
AMY	Left	1	22	0.06 +/– 0.03	14
	Right	2	36	0.03 +/– 0.01	14
ENT	Left	0	0	0	0
	Right	0	0	0.4e–5	1

Table 2.1. Connectivity and connection densities of the olfactory tracts. Columns depict the median and interquartile range [IQR (Q3 – Q1)] of the number of streamlines found between the olfactory tracts and the Regions of Interest (ROIs), the mean and Standard Error of the Mean (SEM) of connection density for each ROI, as well as the number of subjects in which the connectivity between the olfactory tracts and each ROI was identified.

The Olfactory Tract Atlas. Based on our tractography results, we created a normalized, probabilistic atlas to define the locations of the olfactory tracts in MNI space (**Figure 2.5**). We created a binarized mask for each subject that consisted of voxels traversed by olfactory tract streamlines. We then transformed the masks into MNI space and averaged them across subjects to create a probability map of voxels traversed by the olfactory tracts. The atlas captures the trajectory of the olfactory tracts, as they project posteriorly, slightly superiorly and slightly laterally toward the primary olfactory cortex. The three branches of the olfactory tracts (i.e., lateral, medial, and intermediate striae) are clearly visible in the atlas in both hemispheres.

Table 2.2. Individual streamlines and connection densities of the olfactory tracts

	AON (#/density)		FPC (#/density)		TPC (#/density)		OT (#/density)		AMY (#/density)		ENT (#/density)	
Subject	Left	Right	Left	Right	Left	Right	Left	Right	Left	Right	Left	Right
1	748/2.16	–	442/2.18	–	85/0.42	–	451/2.75	99/0.51	33/0.03	–	–	–
2	915/1.77	454/1.05	–	165/0.73	–	199/1.21	–	178/0.67	3/0.002	157/0.13	–	–
3	1/0.002	250/0.46	93/0.39	21/0.08	94/0.47	16/0.07	599/2.55	368/1.56	256/0.24	71/0.07	–	–
4	776/1.87	50/0.12	492/1.98	56/0.22	243/1.1	48/0.28	836/3.62	193/1.12	–	8/0.007	–	–
5	256/0.5	7/0.02	40/0.16	2/0.01	34/0.14	–	155/0.52	117/0.56	1/0.001	–	–	–
6	144/0.38	367/1.05	279/1.53	10/0.07	125/0.61	10/0.07	210/1.24	244/1.16	47/0.05	1/0.001	–	–
7	84/0.23	412/1.24	62/0.28	196/1.44	746/4.75	213/1.09	914/3.81	411/1.36	904/0.8	343/0.31	–	1/0.001
8	428/1.33	34/0.08	107/0.77	26/0.19	44/0.21	29/0.13	311/1.35	198/0.85	1/0.001	2/0.002	–	–
9	558/1.36	123/0.34	–	5/0.03	6/0.03	23/0.11	502/2.01	353/0.97	–	42/0.03	–	–
10	273/0.65	677/1.66	65/0.48	–	144/0.76	2/0.01	212/0.72	8/0.03	22/0.02	–	–	–
11	36/0.09	100/0.23	323/1.15	–	368/0.95	–	363/1.43	69/0.37	4/0.005	–	–	–
12	81/0.26	563/1.54	31/0.15	–	50/0.17	–	220/0.71	575/1.77	–	–	–	–
13	174/0.47	127/0.4	32/0.14	–	243/0.86	–	112/0.48	384/1.39	–	–	–	–
14	113/0.28	895/2.1	93/0.68	–	340/1.13	–	90/0.31	–	122/0.13	–	–	–
15	168/0.25	290/0.48	321/2.2	65/0.29	372/1.6	126/0.39	1269/3.59	536/2.59	–	4/0.004	–	–
16	373/0.8	315/0.71	293/1.98	89/0.7	499/2.01	241/0.92	531/2.03	309/0.96	146/0.13	2/0.002	–	–
17	570/2.11	215/0.79	186/1.19	102/0.36	454/2.24	188/0.65	54/0.2	865/2.59	–	–	–	–
18	36/0.13	64/0.22	462/2.73	42/0.36	572/2.59	224/1.04	569/2.4	206/1.14	21/0.02	78/0.1	–	–
19	386/0.92	518/0.94	–	2/0.01	–	12/0.02	309/0.98	23/0.08	–	–	–	–
20	147/0.22	78/0.13	240/1.59	16/0.1	173/0.76	59/0.23	781/2.54	346/1.38	–	19/0.02	–	–
21	346/0.94	307/1	116/0.63	3/0.02	229/1.01	–	499/1.88	1008/4.52	–	–	–	–
22	347/0.78	709/1.05	11/0.09	18/0.1	182/0.5	174/0.53	551/1.4	182/0.51	3/0.003	50/0.05	–	–
23	414/0.93	451/0.83	104/0.5	133/0.72	144/0.43	207/0.73	86/0.31	187/0.53	–	8/0.007	–	–
24	61/0.12	295/0.6	191/1.31	15/0.13	520/2.18	6/0.03	547/1.99	499/1.66	–	–	–	–
25	271/0.69	342/0.9	21/0.17	2/0.01	79/0.27	38/0.11	1068/3.6	223/0.9	3/0.003	36/0.04	–	–
Total *N*	25	24	22	19	23	18	24	24	14	14	0	1

Table 2.2. Individual streamlines and connection densities of the olfactory tracts. Individual subjects' data. #: number of streamlines identified between the LOT and each ROI; density: number of streamlines divided by ROI volume (mm^3); total N: total number of subjects with streamlines between the LOT and each ROI. – denotes no streamlines found.

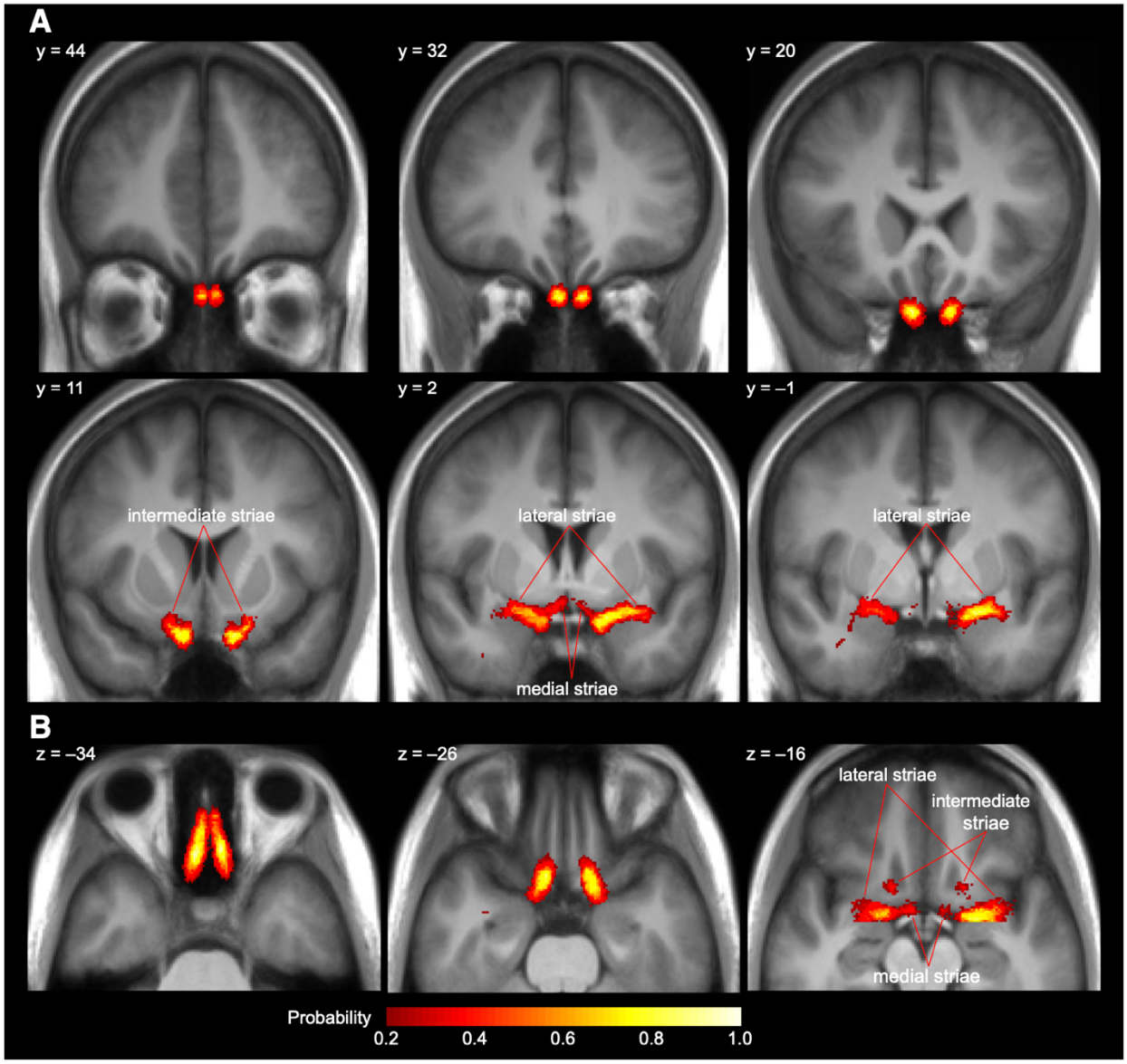

Figure 2.5. Probabilistic atlas of the olfactory tracts in MNI space. **A**, Coronal slices showing the trajectory of the olfactory tracts from the bulbs (y = 44) to the superior projections of the intermediate striae (y = 11), and the projections of the medial and lateral striae (y = 2 and y = –1). **B**, Axial slices showing the projections of the tracts from the bulbs (z = –34), the point where the tracts cross superiorly to the optic nerves (z = –26), and where all three striae are visible in each hemisphere (z = –16). Voxels overlapping in >20% of subjects are overlaid on a mean image of all subjects' MNI-normalized T1 images. This atlas is freely available on NeuroVault (https://neurovault.org/collections/ZTCWDMII/) and on BrainLife (https://brainlife.io/project/ 5ac2a489e182730027c55588).

Microstructure of the olfactory tracts. Next, we used our probabilistic olfactory tract atlas to extract measures of microstructure integrity (i.e., FA and MD) from the olfactory tracts of individual subjects. We first divided the normalized atlas into eight anterior-posterior segments (6.25-mm width) in each hemisphere (**Figure 2.6A**), and then transformed the segmented atlases into each subjects' native diffusion space and extracted the voxel-wise FA and MD values. Finally, we averaged the FA and MD values for each segment in each hemisphere across voxels, weighting FA and MD values by each voxel's probability value in the atlas, thus giving more weight to values closer to the core of the tract, and less weight to those near the edges of the tract that may have partial volume effects with surrounding cerebrospinal fluid. As expected, we found that FA and MD values varied by segment (**Figure 2.6B,C**), presumably driven by local anatomic features.

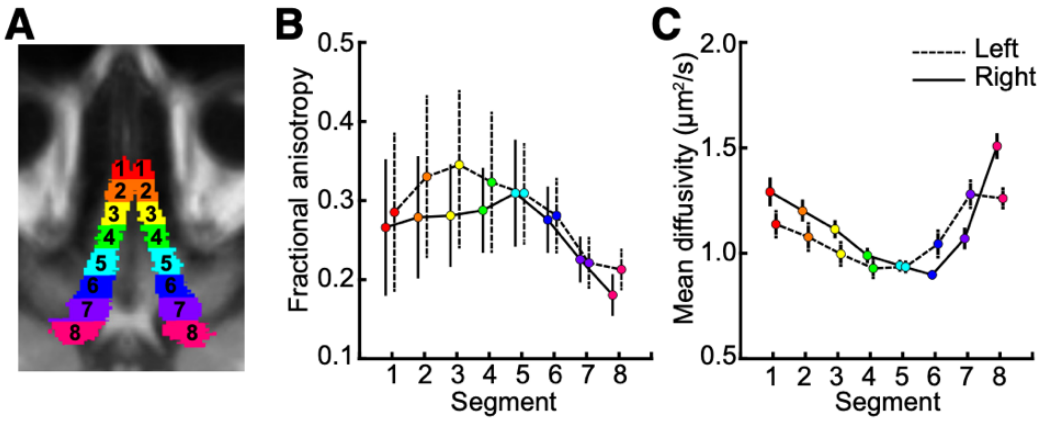

Figure 2.6. Diffusion microstructure profiles of the olfactory tracts. **A**, Segments (1–8) of the olfactory tract atlases in each hemisphere in MNI space. **B**, Fractional Anisotropy (FA) along the longitudinal axis of the olfactory tract. The FA values of each voxel were weighted by the probability of the olfactory tract atlas and averaged across all voxels for each segment. **C**, Same as **B** but for Mean Diffusivity (MD).

Tract microstructure integrity is related to olfactory function. To test whether microstructure integrity in the olfactory tracts is relevant for olfactory perceptual function, we next tested

correlations between the weighted mean FA and MD values for each segment (averaged across both hemispheres) and the three Sniffin' Sticks tests (threshold, discrimination, and identification). We found statistically significant correlations [Bonferroni corrected for multiple comparisons (eight segments x three measures)] between the MD values in segments 5 and 7 and the Sniffin' Sticks discrimination scores (**Figure 2.7**). Both correlations were significant when controlling for sex (Bonferroni corrected; segment 5: b = –0.57, p = 0.0021; segment 7: b = –0.54, p=0.0054) and age using multiple regression (Bonferroni corrected; segment 5: b = –0.65, p = 0.0004; segment 7: b = –0.62, p = 0.0012). We found no significant (Bonferroni corrected) correlations with FA, and no significant correlations between MD and the threshold or identification tests.

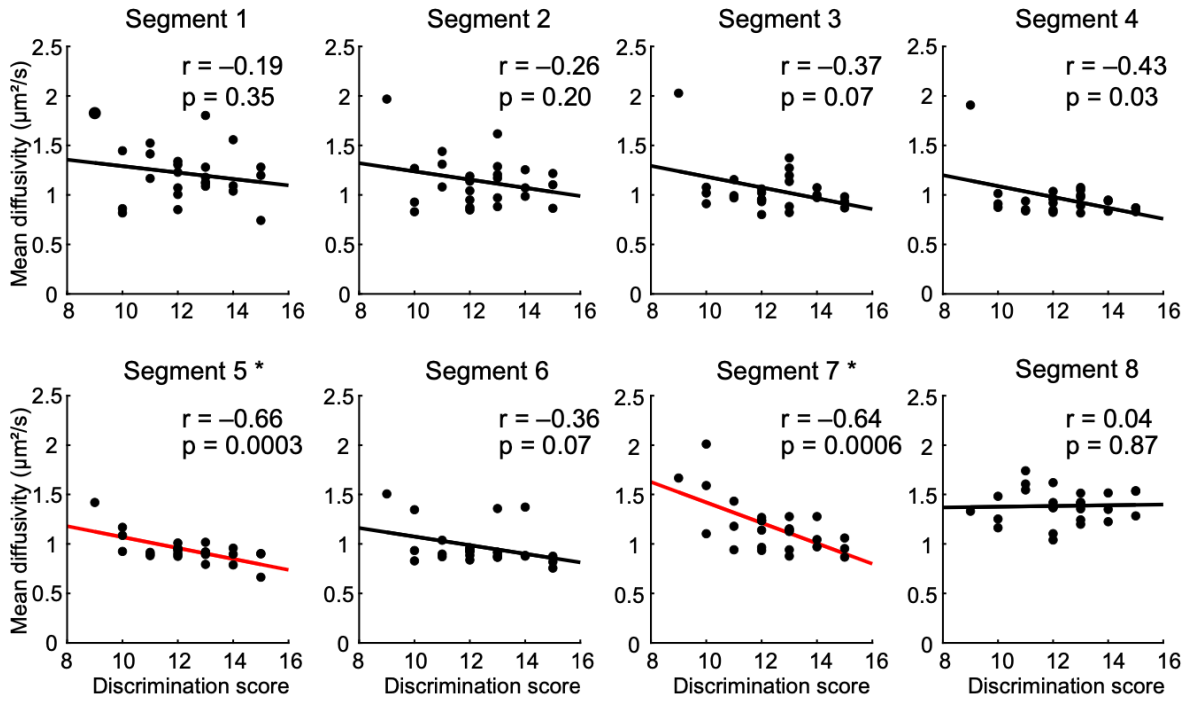

Figure 2.7. Pearson correlations between Mean Diffusivity in the olfactory tracts and olfactory discrimination scores. MD values were averaged across hemispheres for each segment. The straight line indicates least squares fit. Asterisks indicate statistically significant correlations (Bonferroni corrected for eight segments x three measures).

2.5. Discussion

The likely cortical endpoints of the human olfactory tracts were first outlined nearly 70 years ago using silver myelin staining in post mortem brains (Allison, 1954). More recently, several groups have attempted to delineate these projections using modern dMRI methods *in vivo* (Fjaeldstad et al., 2017; Milardi et al., 2017; Skorpil et al., 2011). However, because of methodological limitations, these studies were unable to provide a comprehensive characterization of the striae and their cortical connectivity. In the present study, we implemented innovative imaging and tractography techniques to accomplish this goal. We identified the three striae of the olfactory tracts in 25 subjects, and discovered in vivo connectivity patterns matching those identified in post mortem data by Allison (1954). Based on these results, we have created the first publicly available probabilistic atlas of the olfactory tracts in MNI space. Additionally, we investigated microstructural properties of the tracts, and found that MD correlates with olfactory discrimination scores. In summary, our results provide the first comprehensive characterization of in vivo human olfactory tract connectivity, along with evidence for a relationship between olfactory tract microstructure and olfactory perceptual function.

In our data, the lateral, medial, and intermediate stria were identified in all subjects in at least one hemisphere. The lateral striae were the largest, and curved sharply laterally to meet FPC, TPC, and AMY. The medial striae curved medially to meet the OT, located at the base of the nucleus accumbens. The intermediate striae were the smallest, and projected superiorly to meet AON near the olfactory trigone. All three striae are clearly visible in both hemispheres within our probabilistic olfactory tract atlas.

We found reliable connectivity between the olfactory tracts and FPC, TPC, the AON, and the OT, with all subjects showing these connections in at least one hemisphere. In addition, 76% of subjects showed relatively sparse connectivity with the AMY in at least one hemisphere. This is consistent with Allison (1954)'s findings, wherein the majority of lateral striae fibers were found to reach FPC and TPC, with relatively few fibers continuing to meet AMY. Connectivity with EC, observed in both rodents and macaques (Carmichael et al., 1994; Haberly & Price, 1978a, 1978b; Miyamichi et al., 2011), was nearly absent in our data. This could be because of one of two reasons. First, while Haberly and Price note connectivity with the entire extent of the lateral EC in the rodent, Carmichael and colleagues report that only Layer I of the rostral EC receives sparse olfactory tract inputs in the macaque, and Allison reports no olfactory tract connectivity with EC in the human. In both rats and macaques, association fibers between the EC and piriform cortex are much denser than fibers projecting directly between the EC and the olfactory bulb (Carmichael et al., 1994; Haberly & Price, 1978a, 1978b; White, 1965). While the human EC is likely involved in olfactory processing (Bao et al., 2016, 2019; Poellinger et al., 2001), it may be two synapses away from the olfactory bulb rather than directly connected. Further investigation is warranted to determine the specific olfactory connectivity patterns of the human EC. Second, the lack of connectivity observed in our data may be because of known limitations with diffusion tractography methods. Tracking directly from the olfactory tracts to EC requires streamlines to cross piriform gray matter, where the diffusion signal tends to be more isotropic, and thus not conducive to tractography. Additionally, where direct streamlines are found, it is impossible to tell whether they represent direct synaptic connectivity with the olfactory bulb, or rather secondary synaptic connections with the piriform cortex. This may also

explain the reduced number of subjects and the reduced density of streamlines found connecting the olfactory tracts with the AMY. Thus, diffusion tractography may not be an appropriate method for evaluating these particular connections. Further methodological innovation will be necessary to identify the presence or absence of these pathways in the human.

In addition to connectivity analyses, we characterized diffusion-based measures of tissue microstructure in the olfactory tracts. Fractional anisotropy (FA) and Mean Diffusivity (MD) are calculated from the diffusion signal and serve as non-invasive proxy measures of microstructural tissue properties, such as cell body or axon density, thickness of myelination, and the spatial organization of the underlying fiber architecture (Basser & Pierpaoli, 1996; Song et al., 2003, 2005). In segment 1, comprising the olfactory bulbs (gray matter), we found relatively low FA and relatively high MD values. In successive segments 2–5, comprised of the myelinated, single-trajectory core of the olfactory tracts, we see increasing FA and decreasing MD. Segments 6–8 comprise portions of the olfactory tracts that cross over the optic nerves and branch into several striae, including multiple fiber orientations and partial volume effects with neighboring gray matter. Accordingly, we see decreasing FA and increasing MD in these segments. FA and MD measures have been correlated with learning and skills training (Bengtsson et al., 2005; Hofstetter et al., 2013; Scholz et al., 2009), perceptual performance (Yeatman et al., 2011), and neurodegeneration-related loss of function (Song et al., 2003, 2005) in functionally-specific white matter pathways. An open question is whether olfactory tract microstructure is similarly related to olfactory perceptual performance. We observed significant correlations between odor discrimination scores and MD measures in segments 5 and 7 of the olfactory tracts, and most other olfactory tract segments showed similar nonsignificant trends. Differences between

segments are likely because of varying noise levels along the lengths of the tracts, driven by magnetic field inhomogeneities, and partial volume effects with surrounding anatomic structures. However, the general direction of these effects suggests that tissue integrity in the human olfactory tracts supports olfactory perceptual function. We speculate that MD measures in the olfactory tracts may in part reflect individual variations in myelination or axon density, thus affecting the speed or bandwidth of olfactory information transfer. We note that our subject sample (25 healthy young adults who scored above anosmic thresholds) may be too limited to fully capture microstructure-function relationships. We suggest that future investigations include larger sample sizes, and consider wider age ranges, varied olfactory ability, and clinical populations with olfactory deficits.

In our study, we used modern technological innovations to provide a comprehensive characterization of human olfactory tract connectivity in vivo. Two previous dMRI studies (Fjaeldstad et al., 2017; Skorpil et al., 2011) attempted to reconstruct the olfactory tracts using the tensor model, and while they were able to reconstruct portions of the tracts, they were unable to characterize the branching and curving striae or the cortical connectivity of the tracts. Our study and one previous study (Milardi et al., 2017) used a CSD model to address this issue. While Milardi and colleagues identified the larger lateral striae, they were unable to identify the intermediate and medial striae, likely because of a combination of susceptibility artifacts and low voxel resolution. In the present study, we applied an optimized RESOLVE sequence (Porter & Heidemann, 2009), designed specifically to reduce susceptibility artifacts and achieve a higher scanning resolution (1.5 mm) than has been used before to investigate the human olfactory system. Additionally, our subjects wore individualized head stabilizers during scanning to

prevent motion. With these data, we were able to characterize all three striae of the olfactory tracts and identify their connectivity with primary olfactory cortex. We also provide the first in-depth description of the functionally-relevant microstructural properties of the tracts and their relationships with olfactory function.

While the RESOLVE sequence greatly improves image quality with relatively little susceptibility artifact, it requires a 7-fold increase in scan-time, making it less suitable for clinical settings. Additionally, we still observed a small region of signal drop-out near the sphenoid sinus in most subjects, preventing continuous tractography across the entire lengths of the olfactory tracts. However, based on *post mortem* observations, we are confident that interpolating between the two fiber groups accurately describes the trajectory of these white matter fibers. Additionally, when reconstructing the olfactory tracts, it is important to watch for streamline "jumping," where streamlines may progress in anatomically impossible directions, especially in regions with low signal (Mori, 2007). When exclusionary ROIs were not placed to constrain tracking, we found that streamlines seeded in the olfactory bulb would jump into the parallel fibers of the gyrus rectus. To prevent such jumping resulting in erroneous streamlines, we placed extensive exclusionary ROIs in the gyrus rectus.

In summary, our results offer an in depth look at the in vivo anatomy of the human olfactory tracts. They provide the first step toward in vivo investigations of human olfactory tract structure-function relationships, which could be extended to address questions regarding microstructural changes following olfactory perceptual training (Haehner et al., 2013; Jiramongkolchai et al., 2021). In addition, our methods may be used in combination with our

atlas to investigate olfactory tract integrity in clinical populations presenting with anosmia, such as those with Alzheimer's disease, Parkinson's disease, or multiple sclerosis.

2.6. Acknowledgements and Author Contributions

This thesis chapter was published in the Journal of Neuroscience in January, 2022:

Echevarria-Cooper, S. L., Zhou, G., Zelano, C., Pestilli, F., Parrish, T. B., & Kahnt, T. (2022). Mapping the Microstructure and Striae of the Human Olfactory Tract with Diffusion MRI. *Journal of Neuroscience*, *42*(1), 58–68. https://doi.org/10.1523/JNEUROSCI.1552-21.2021

This work was supported by the Northwestern Parkinson's Disease and Movement Disorders Advisory Council, National Institute on Deafness and Other Communication Disorders Grant R01 DC015426 (to T.K.), and National Institutes on Aging Grants P30 AG013854 (to T.K.) and the Mechanisms of Aging and Dementia Training Program T32 AG020506 (to S.L.E.-C.).

Shiloh L. Echevarria-Cooper, Franco Pestilli, Todd B. Parrish, and Thorsten Kahnt designed the research approach. Shiloh L. Echevarria-Cooper collected data and performed research. Guangyu Zhou and Christina Zelano contributed unpublished analytic tools including reference maps of primary olfactory cortical regions of interest. Shiloh L. Echevarria-Cooper analyzed data. Shiloh L. Echevarria-Cooper wrote the first draft of the paper. Thorsten Kahnt contributed to writing and editing the paper. Guangyu Zhou, Christina Zelano, Franco Pestilli, and Todd B. Parrish discussed, provided commentary, and edited the manuscript.

Chapter 3: Anatomical Parcellation of the Human Orbitofrontal Cortex using Diffusion MRI

3.1. Abstract & Significance

The orbitofrontal cortex (OFC) is an important brain region involved in multimodal sensory integration, visceromotor and emotional regulation, reward learning, and decision making. To fully understand the complex functional role of the human OFC, we must develop a detailed understanding of its anatomical organization and connectivity with the rest of the brain. In the current study, we used an optimized diffusion MRI and tractography approach to investigate the whole-brain connectivity of the human OFC in N=25 adult subjects. We then applied K-means clustering (K=2-6) to identify subregions of the OFC based on distinct anatomical connectivity patterns. We found that the OFC shares widespread, bilateral connectivity with prefrontal, temporal, and limbic cortex, subcortical limbic structures including the hippocampus and amygdala, and dense connectivity with the ventral striatum and nucleus accumbens. K-means clustering, performed separately in each hemisphere, identified robust symmetric clustering solutions for each tested value of K. For K=2, we replicated the well-known medial-lateral division previously identified in the macaque. For K=3, the medial cluster was preserved, while the lateral cluster split into anterior and posterior clusters, suggesting an anterior-posterior organization of the human OFC. For higher values of K, clusters roughly corresponded to OFC sulcogyral morphology (K=5), and diverse cytoarchitectural regions previously identified in the human OFC (K=6). Here, we present a detailed characterization of the whole brain connectivity of the human OFC, alongside descriptions of our K-means clustering results and notable differences in connectivity across clusters in the K=2 and K=3

solutions. Further, we consider the diverse functional roles of the human OFC that may be supported by its anatomical involvement in diverse brain networks.

3.2. Introduction

The orbitofrontal cortex (OFC), located on the ventral surface of the frontal lobes, is a complex brain area that plays a role in many functions related to perception and behavior. It is involved in multimodal sensory integration, representation of motivationally salient memories, flexible updating of reward values for specific stimuli based on context and experience, visceromotor and emotional regulation, and coordinating adaptive goal-directed behaviour (Howard & Kahnt, 2021; Rudebeck & Rich, 2018; Stalnaker et al., 2015; Wallis, 2012). To support a full mechanistic understanding of the OFC's role in these complex functions, we must develop a strong understanding of its anatomical organization and connectivity with the rest of the brain.

The detailed white matter connectivity of the macaque OFC has been characterized with axon tracing methods and electrophysiological techniques (Carmichael & Price, 1995b, 1995a, 1996; Cavada et al., 2000; Giguere & Goldman-Rakic, 1988; Haber et al., 1995; Rempel-Clower & Barbas, 1998; Yarita et al., 1980). The macaque OFC has widespread connectivity with sensory, premotor, limbic, and visceromotor brain regions. Distinct medial and lateral regions of the macaque OFC have been defined based on their brain-wide connectivity and intrinsic connectivity between distinct cytoarchitectural regions within the OFC (Carmichael & Price, 1996). The lateral OFC receives heavy inputs from sensory and premotor regions, and is thought to be involved in multimodal sensory integration (Carmichael & Price, 1995b). The medial OFC,

conversely, sends heavy outputs to limbic and visceromotor regions, and is likely involved in regulating emotion and coordinating motivated behaviors (Carmichael & Price, 1995a; Öngür et al., 1998).This medial-lateral distinction has also been demonstrated in the human OFC using measures of resting-state functional connectivity between the OFC and the rest of the brain (Kahnt et al., 2012). In addition to a medial-lateral distinction, the macaque and human OFC have both been shown to have a distinct rostro-caudal organization (Carmichael & Price, 1994; Ongür et al., 2003b). More rostral regions of the OFC are characterized by six-layered cortex with a dense granule cell layer, while more caudal regions are characterized by dysgranular and agranular cortex with very sparse granule cell layers. In general, cortico-cortical white matter connections of the macaque OFC have been shown to match in terms of granularity. More rostral OFC regions share heavier connectivity with other granular cortical regions, including visual, auditory, and somatosensory cortex. More caudal OFC regions share heavier connectivity with other agranular and dysgranular regions, including olfactory, visceral, and gustatory cortex (Cavada et al., 2000; Kringelbach & Rolls, 2004).

In the human, the major OFC white matter pathways have been documented with Klingler dissection (Ebeling & Cramon, 1992; Martino et al., 2010) and diffusion magnetic resonance imaging (dMRI) (Croxson et al., 2005; Heather Hsu et al., 2020; Thiebaut de Schotten et al., 2012). These include the pathways of the uncinate fasciculus, the inferior fronto-occipital fasciculus, the orbito-polar tract, the extreme capsule, the fornix, the cingulum, amygdala fibers, and ventral striatal fibers. However, the precise connectivity of these pathways, their topographic organization, and the identification of OFC subregions with distinct anatomical connectivity patterns has not been done in the human brain, largely due to methodological limitations.

In vivo investigations of the human OFC white matter are possible with dMRI. However, typical methods employ single-shot echo planar imaging techniques, which leave the OFC region substantially affected by susceptibility artifacts, hyperintense signals, and blurring (Porter & Heidemann, 2009). These artifacts prevent an accurate characterization of the local diffusivity, and may lead to inaccurate reconstructions of local white matter pathways. In the present study we used an optimized dMRI protocol to image the human OFC with very few artifacts in N=25 young adult subjects (Echevarria-Cooper et al., 2022). With these data, we have characterized the whole brain connectivity of the OFC using probabilistic tractography, based on a constrained spherical deconvolution model (Tournier et al., 2007). We then used a data-driven k-means parcellation approach to identify unique OFC subregions with distinct anatomical connectivity patterns. Here, we describe the brain-wide anatomical connectivity of the human OFC, parcellation results for K=2-6, and the distinct anatomical connectivity patterns of each identified OFC subregion for select clustering solutions. We then consider the potential functional roles of each subregion in consideration of our results alongside the broader OFC literature.

3.3. Materials & Methods

The dMRI data and T1-weighted volumes used for these analyses are from the same dataset described above in Chapter 2 of this thesis, originally collected by Echevarria-Cooper et al. (2022). The following sections "*Subjects*", "*Personalized head stabilizers",* "*MRI data acquisition",* and portions of "*MRI data preprocessing*" are adapted from Echevarria-Cooper et al. (2022), and also appear in Chapter 2 of this thesis.

Subjects. A total of 27 right-handed subjects (14 male and 13 female; age: mean 25.76 +/- standard deviation 4.01 years), with no neurologic disorders, psychiatric disorders, or MRI contraindications, were enrolled in this study. Two subjects, both males, were excluded from final analyses because they did not complete the MRI scanning protocol. The study was approved by the Northwestern IRB (STU00098371), and all subjects gave written informed consent for participation.

Personalized head stabilizers. Subjects wore personalized head stabilizers to prevent head motion for the duration of MRI scanning (Power et al., 2019). 3D renderings of each subject's face and head were created using a handheld camera and the Caseforge iOS application. The head stabilizers were 3D-milled to fit the subject's face and head on the inside and the shape of the MRI scanner coil on the outside. An example is shown in **Figure 2.1C** (see Chapter 2, Figure 2.1).

MRI data acquisition. Subjects underwent MRI scanning on a 3T Siemens Prisma scanner with a 64-channel head-neck coil. We collected a set of diffusion-weighted images and a T1-weighted image. Subjects wore their customized head stabilizers for the duration of the scans.

We used a high-resolution (1.5 mm isotropic) RESOLVE dMRI scan with seven readout segments (Porter & Heidemann, 2009) to collect the diffusion-weighted images. This sequence is different from typical single-shot echo planar imaging (SS-EPI) techniques in that it splits data collection into seven segments in the read-out direction and re-excites the tissue before each segment with a new radio frequency pulse. The readout segments are combined in the end to

produce the full image. The shorter readout segment allows for a shorter TE than is possible in SS-EPI sequences. However, it takes more time to acquire a complete dataset, based on the number of segments. We also included a navigator echo to monitor between-segment motion, so that volumes were re-acquired if the motion was excessive (Porter & Heidemann, 2009). In addition, we used simultaneous multi-slice acquisition (Nunes et al., 2006) to allow for improved spatial coverage required when using such small voxels. This sequence was designed based on extensive pilot testing to provide high-resolution images with reduced blurring, and largely free of susceptibility artifacts compared with conventional SS-EPI techniques (**Figure 2.1D**; see Chapter 2, Figure 2.1). Imaging parameters were as follows: 92 slices; field of view (FoV) = 240 mm; matrix size = 240 x 240 x 138 mm; 90 diffusion-weighted directions at b = 1000 s/mm^2; 12 interspersed b0 volumes; phase encoding = A > P; TE1 (image echo) = 61 ms; TE2 (navigator echo) = 98 ms; repetition time (TR) = 6250 ms; flip angle = 180°; bandwidth = 897 Hz/Px, multiband factor = 2. The scan time for this RESOLVE dMRI sequence was approximately 1 hour and 30 minutes. An oblique slice angle (~30° relative to the AC–PC plane) was used to further reduce susceptibility artifacts (Weiskopf et al., 2006).

The parameters for the T1-weighted anatomical scan were as follows: 1.0 mm isotropic, TE = 2.94 ms, TR = 2300 ms, flip angle = 9°, FoV = 256 mm, matrix size = 256 x 256 x 176 mm; phase encoding = A > P, bandwidth = 240 Hz/Px, scan duration = 5 minutes.

MRI data preprocessing and fitting the constrained spherical deconvolution model. All MRI data were converted to the Nifti file type using MRIcron's dcm2niix function (X. Li et al., 2016). The diffusion MRI data were corrected for motion and eddy current artifacts using FSL's function,

eddy_openmp (Jenkinson et al., 2012; S. M. Smith et al., 2004; Woolrich et al., 2009). As the multi-shot RESOLVE sequence was designed to prevent susceptibility artifacts, additional susceptibility correction was not applied. The T1-weighted images were co-registered to the native diffusion space using SPM12 (SPM12 Software, 2014). All diffusion model fitting and tractography were performed in the native diffusion space to prevent registration-related errors in the alignment of the b-vectors with the diffusion-weighted data. MRtrix3 software was used to fit the constrained spherical deconvolution (CSD) model (Tournier et al., 2019). First, the response function for spherical deconvolution was estimated using the dwi2response tournier function (Tournier et al., 2013). Then, the CSD fiber orientation distribution (FOD) functions were fit using the dwi2fod function (Tournier et al., 2007).

Tissue Masks and Regions of Interest. Probabilistic tissue masks, including white matter, cortical gray matter, subcortical gray matter, and cerebrospinal fluid (CSF) masks, were created from each subject's T1-weighted image using the MRtrix3 function 5ttgen with the fsl algorithm (Patenaude et al., 2011; R. E. Smith et al., 2012; S. M. Smith, 2002; S. M. Smith et al., 2004; Zhang et al., 2001). A mask of the gray matter-white matter interface (GMWMI) was then created using the MRtrix3 function 5tt2gmwmi (R. E. Smith et al., 2012), including overlapping voxels between the gray matter and white matter masks. The GMWMI mask and the subcortical gray matter mask (GMWMI+SCGM) were then combined and re-sampled to 3mm isotropic resolution. For each subject, an indexed integer value was assigned to each 3mm voxel in the GMWMI+SCGM mask, and used to reference each voxel as an individual node in the final connectome matrix for each subject.

The Automated Anatomical Parcellation atlas (AAL3v1, June 2020 release) (Rolls et al., 2015, 2020; Tzourio-Mazoyer et al., 2002) was used to identify voxels within the OFC, and to reference regions of interest (ROIs) that share connectivity with the OFC. The 1mm resolution atlas was downloaded and inverse normalized using the nearest neighbor algorithm to each subject's T1-weighted image (previously co-registered to the native space diffusion-weighted images) using the SPM deformations toolbox (SPM12 Software, 2014). The inverse-normalized atlases were then resliced to 3mm resolution matching the 3mm GMWMI+SCGM masks for each subject. Voxels in the GMWMI+SCGM mask for each subject that overlapped with AAL3 regions 23-32, including the left and right gyri rectus, medial orbital gyri, lateral orbital gyri, anterior orbital gyri, and posterior orbital gyri, were defined as OFC voxels. A mask of these OFC GMWMI voxels was created for both 1mm and the 3mm resolution.

Tractography and Generating the Voxelwise OFC Connectome Matrix. Tractography was carried out in each individual subject's native space and then used to create a unique OFC connectome matrix for each subject. Anatomically constrained tractography (R. E. Smith et al., 2012) was carried out using the MRtrix3 function tckgen, with the iFOD2 probabilistic tractography algorithm (Tournier et al., 2010). Two sets of 10 million streamlines were generated for each subject. For the first set, streamlines were seeded from the 1mm resolution whole brain GMWMI-SCGM mask. For the second set, streamlines were seeded from the 1mm resolution OFC GMWMI mask. For both sets, streamlines were only allowed to terminate in the gray matter-white matter interface or in subcortical gray matter regions. The two sets of streamlines were then combined to create a 20 million streamline tractogram for each subject.

Streamlines were then assigned weights based on the updated spherical-deconvolution informed filtering of tractograms (SIFT2) method (R. E. Smith et al., 2013, 2015b). This method compares the number of streamlines and their major orientations in each voxel with the CSD FOD for that voxel. The amplitude of the FOD lobes along each major direction of diffusion is related to the magnitude of diffusivity along that direction, and proportional to the volume compartment of white matter fibers oriented along that direction. The SIFT2 algorithm weights the streamlines in the tractogram such that the weighted number of streamlines in each direction is proportional to the FOD lobe amplitudes, providing a more anatomically correct representation of the volume of white matter fibers traversing in that direction. This helps to produce more anatomically-informed connectomes by preventing large white matter pathways from being over-represented in the voxel-to-voxel connectivity estimates.

The SIFT2-weighted streamlines were then used to create a voxel-wise connectome matrix for each subject, using the MRtrix3 function tck2connectome (R. E. Smith et al., 2015a). The indexed voxels of the 3mm resolution GMWMI-SCGM mask were used as nodes in the connectome matrix, and for each pair of nodes the sum of the SIFT2 streamline weights between them was recorded as the measure of connectivity. The whole-brain connectome matrices were then read into Matlab (version R2020b). This matrix was then reduced to create two separate connectome matrices for the two hemispheres. Rows were reduced in each matrix so that only rows corresponding to 3mm resolution OFC GMWMI voxels for that hemisphere were retained. Empty columns, referring to voxels outside the OFC that had zero streamlines connecting to an OFC voxel, were removed. The two resulting matrices thus had single hemisphere (left or right)

OFC voxels across the rows, and non-empty 3mm resolution GMWMI-SCGM voxels across both the ipsilateral and contralateral hemispheres in the columns.

K-Means Parcellation. K-means parcellation was carried out separately for each hemisphere in each subject. The connectome matrices described above were used as input to the Matlab (version R2020b) function kmeans, from the Statistics and Machine Learning package. The correlation between two OFC voxel's connectivity patterns was used as the distance measure. Kmeans was run for K=2-6, with 1000 iterations and 100 replicates for each value of K. The cluster assignments for each OFC voxel (row in the connectome matrix) were then written out in 3mm resolution Nifti masks for each hemisphere for each subject.

All cluster assignment masks were normalized to MNI space with the nearest neighbors algorithm using SPM (SPM12 Software, 2014). Since the k-means algorithm begins with randomly placed cluster centers, the resulting cluster number labels do not necessarily correspond in brain-space across subjects. To better compare clusters across subjects, cluster number labels for 24 subjects were re-labeled based on spatial similarity with one randomly selected subject designated as the "template". (Only the numbers used to label each cluster in the cluster map were changed – voxel membership to a particular cluster was preserved.) The template subject's voxel-wise cluster labels were first read into Matlab. For each remaining subject, their voxel-wise cluster labels were read in, and every possible combination of cluster-labeling was compared to the template subject. The numbering scheme that shared the most overlap with the template subject was retained. This was repeated for the cluster maps for every

value of K. The re-labeled cluster maps were then averaged to produce probability maps for each cluster in each hemisphere for each value of K.

Evaluation of Cluster Connectivity. For the entire OFC (equivalent to K=1) and for the K=2 and K=3 clustering solutions, we extracted tracts from the whole-brain tractogram that intersected with the 3mm GMWMI voxels assigned to each individual cluster in each hemisphere, for each subject. Tract density maps were then created in the T1 native space (1mm resolution) for each set of extracted streamlines, using the MRtrix3 tckmap function (Calamante et al., 2010). Tract density values were recorded as the sum of SIFT2-weighted streamlines in each voxel that intersected with a voxel in the 3mm OFC GMWMI masks for each cluster. Voxels in the tract density maps that intersected with the 1mm resolution GMWMI-SCGM mask were saved, and then normalized to MNI space; voxels deep to the GMWMI-SCGM mask in the white matter were not included or used to evaluate cortico-cortical or cortico-subcortical connectivity. Normalized GMWMI-SCGM tract density maps from each subject were then averaged together, producing one averaged track density map for each cluster in each hemisphere. Voxels from these normalized tract density maps with a weighted streamline count greater than 1.0 that intersected with a labeled region in the 1mm resolution AAL3 atlas were used to evaluate OFC cluster connectivity with each AAL3 region.

3.4. Results

Whole-Brain OFC Connectivity. Ipsilateral and contralateral connectivity of the OFC with regions defined in the AAL3 atlas (Rolls et al., 2020) were evaluated using probabilistic

tractography based on a constrained spherical deconvolution model. SIFT2-weighted streamline counts (R. E. Smith et al., 2015b) were averaged across voxels in each AAL3 region that received streamlines from the OFC, and are listed in **Table 3.1**.

We found that the connectivity patterns of the left and right OFC were largely symmetric. Cortico-cortical connections included widespread connectivity with the frontal and temporal lobes and with limbic cortex, as well as a few connections in the parietal and occipital lobes. In the frontal lobes (**Figure 3.1A**), the OFC shared strong connectivity with the ipsilateral superior frontal gyrus (dorsolateral, medial, and medial orbital parts), the middle frontal gyrus, and the inferior frontal gyrus (opercular, triangular, and pars orbitalis). Connectivity with the superior and middle frontal gyri was constrained to the anterior portions of these gyri, while connectivity was observed throughout the inferior frontal gyrus. The regions of strongest connectivity (>100 streamlines/voxel) included the medial orbital part of the superior frontal gyrus and pars orbitalis of the inferior frontal gyrus. In the left hemisphere, we found a weak connection with the ipsilateral Rolandic operculum. The left and right OFC each shared connectivity with all contralateral OFC gyri except the lateral orbital gyrus, with the strongest contralateral OFC-to-OFC connectivity in the gyrus rectus. We also observed contralateral connectivity with the superior frontal gyrus (dorsolateral, medial, and medial orbital parts), middle frontal gyrus, and the inferior frontal gyrus pars orbitalis.

In the temporal lobes, the OFC shared ipsilateral connectivity with the superior and middle parts of the temporal pole, the superior temporal gyrus, the middle temporal gyrus, the inferior temporal gyrus, and a few voxels in the anterior fusiform gyrus. Though not defined in the AAL3 atlas, we observed very strong connectivity (>100 streamlines/voxel) with the

Table 3.1: Whole Brain OFC Connectivity					
		Left Hemisphere Connectivity		Right Hemisphere Connectivity	
AAL Region Name	**AAL Label**	**Left OFC, Ipsilateral**	**Right OFC, Contra-lateral**	**Right OFC, Ipsilateral**	**Left OFC, Contra-lateral**
Gyrus rectus	23,24		6.0		65.6
Medial orbital gyrus	25,26		2.0		2.6
Anterior orbital gyrus	27,28		2.7		2.8
Posterior orbital gyrus	29,30		1.1		1.2
Lateral orbital gyrus	31,32				
Superior frontal gyrus, dorsolateral	3,4	46.1	2.2	41.7	2.5
Superior frontal gyrus, medial	19,20	13.3	4.2	12.5	4.7
Superior frontal gyrus, medial orbital	21,22	171.2	7.9	152.3	22.3
Middle frontal gyrus	5,6	59.5	1.4	41.8	1.5
Inferior frontal gyrus, opercular part	7,8	1.4		1.4	
Inferior frontal gyrus, triangular part	9,10	10.8		8.6	
Inferior frontal gyrus, pars orbitalis	11,12	189.0	1.2	181.5	1.2
Superior temporal gyrus	85,86	2.2		2.3	
Temporal pole: superior temporal gyrus	87,88	7.9		13.1	
Middle temporal gyrus	89,90	1.8		2.0	
Temporal pole: middle temporal gyrus	91,92	4.0		3.7	
Inferior temporal gyrus	93,94	1.8		1.5	
Fusiform gyrus	59,60	1.7		2.1	
Insula	33,34	35.5		33.0	1.3
Rolandic operculum	13,14	1.1			
Olfactory cortex	17,18	91.1	12.9	77.7	16.8
Calcarine fissure	47,48	1.1			
Lingual gyrus	51,52	2.0		1.8	
Precuneus	71,72	1.4		1.2	
Middle cingulate & Paracingulate Gyri	37,38	4.9	1.1	2.6	1.3

Posterior cingulate gyrus	39,40	1.8		1.2	
Anterior cingulate cortex, subgenual	151,152	76.4	4.0	34.7	7.4
Anterior cingulate cortex, pregenual	153,154	17.0	3.9	5.3	2.8
Anterior cingulate cortex, supracallosal	155,156	17.5	2.2	9.6	3.5
Amygdala	45,46	3.7		8.5	
Hippocampus	41,42	2.7		3.0	1.3
Parahippocampal gyrus	43,44	4.1		2.5	
Caudate nucleus	75,76	28.6	13.3	27.1	7.6
Lenticular nucleus, Putamen	77,78	28.7	1.6	32.2	1.7
Lenticular nucleus, Pallidum	79,80	5.9		5.3	1.0
Nucleus accumbens	157,158	135.3	10.2	104.2	9.6
Thalamus, Anteroventral Nucleus	121,122	11.5		5.5	
Lateral posterior	123,124	2.2		3.9	
Ventral anterior	125,126	13.4		16.9	
Ventral lateral	127,128	2.9		4.7	
Ventral posterolateral	129,130	1.2		1.9	
Intralaminar	131,132	9.8		5.6	
Reuniens	133,134	7.6		7.0	
Mediodorsal medial magnocellular	135,136	6.9		4.9	1.7
Mediodorsal lateral parvocellular	137,138	4.1		8.0	
Lateral geniculate	139,140	2.6		2.8	
Medial Geniculate	141,142	1.4		1.3	
Pulvinar anterior	143,144	2.1		2.2	
Pulvinar medial	145,146	1.8		2.3	
Pulvinar lateral	147,148	2.2		3.0	
Pulvinar inferior	149,150			1.6	

Table 3.1. **Connectivity of the left and right OFC with regions in the AAL3 Atlas**. Recorded values are tract density measures calculated by averaging SIFT2-weighted streamline counts (R. E. Smith et al., 2015b) across voxels in each AAL3 region that received streamlines from the OFC. Darker blue cells indicate regions with higher tract density, reflecting stronger anatomical connectivity.

temporal opercular cortex, including auditory cortex. We also observed very strong ipsilateral connectivity between the OFC and the insula. Connectivity was strongest in the anterior insula, including regions likely involved in taste, interoception, and visceral sensory function (**Figure 3.1B**). We found that the OFC shared very strong ipsilateral and contralateral connectivity with the primary olfactory cortex, located at the junction of the frontal and temporal lobes.

We observed weak connectivity with parietal regions, including the precuneus, the middle cingulate and paracingulate gyri, and the posterior cingulate gyrus. These regions are likely involved in visuospatial processing (precuneus) and regulating attention as part of the default mode network (posterior cingulate). We also observed weak bilateral connectivity with visual areas in the lingual gyrus of the occipital lobe, and in the left hemisphere with cortex surrounding the calcarine fissure (**Figure 3.1C**).

Limbic connectivity of the OFC includes both cortical and subcortical targets. We found a topographic pattern in the strength of connectivity between the OFC and the ipsilateral anterior cingulate cortex (**Figure 3.1A**). Connectivity was strongest with the subgenual portion of the anterior cingulate cortex, followed by the pregenual and supracallosal portions of the anterior cingulate cortex. Contralateral connectivity with the anterior cingulate cortex was much weaker, but this same topographical pattern was preserved with stronger connections with the subgenual regions than with the pregenual and supracallosal regions. In both hemispheres, we additionally found ipsilateral connectivity with the hippocampus, amygdala, and parahippocampal gyrus. Connectivity with the ipsilateral nucleus accumbens was very strong (>100 streamlines/voxel) in both hemispheres (**Figure 3.2**), and strong contralateral projections were also observed in both

hemispheres. In addition, although the hypothalamus is not included in the AAL3 atlas, we observed bilateral ipsilateral connectivity with GMWMI voxels adjacent to the hypothalamus.

We observed strong connectivity between the OFC and the basal ganglia. Very strong ipsilateral connectivity was observed with the caudate and the putamen, and weaker ipsilateral connectivity was observed with the globus pallidus (pallidum). We further observed contralateral connectivity with the caudate, putamen, and globus pallidus. Connectivity was observed throughout the caudate, putamen, and globus pallidus, but voxels with the strongest connectivity were located in the anterior-most and ventral-most regions of these nuclei (**Figure 3.2**).

We further observed ipsilateral OFC connectivity with a variety of thalamic nuclei (**Figure 3.3**), including the anteroventral nucleus, the lateral posterior nucleus, the ventral anterior nucleus, the ventral lateral nucleus, the ventral posterolateral nucleus, the intralaminar nucleus, the reuniens, the mediodorsal nucleus, the lateral geniculate nucleus, the medial geniculate nucleus, and the pulvinar. The nuclei with the densest connectivity included the mediodorsal nucleus, the reuniens, the intralaminar nucleus, the ventral anterior nucleus and the anteroventral nucleus.

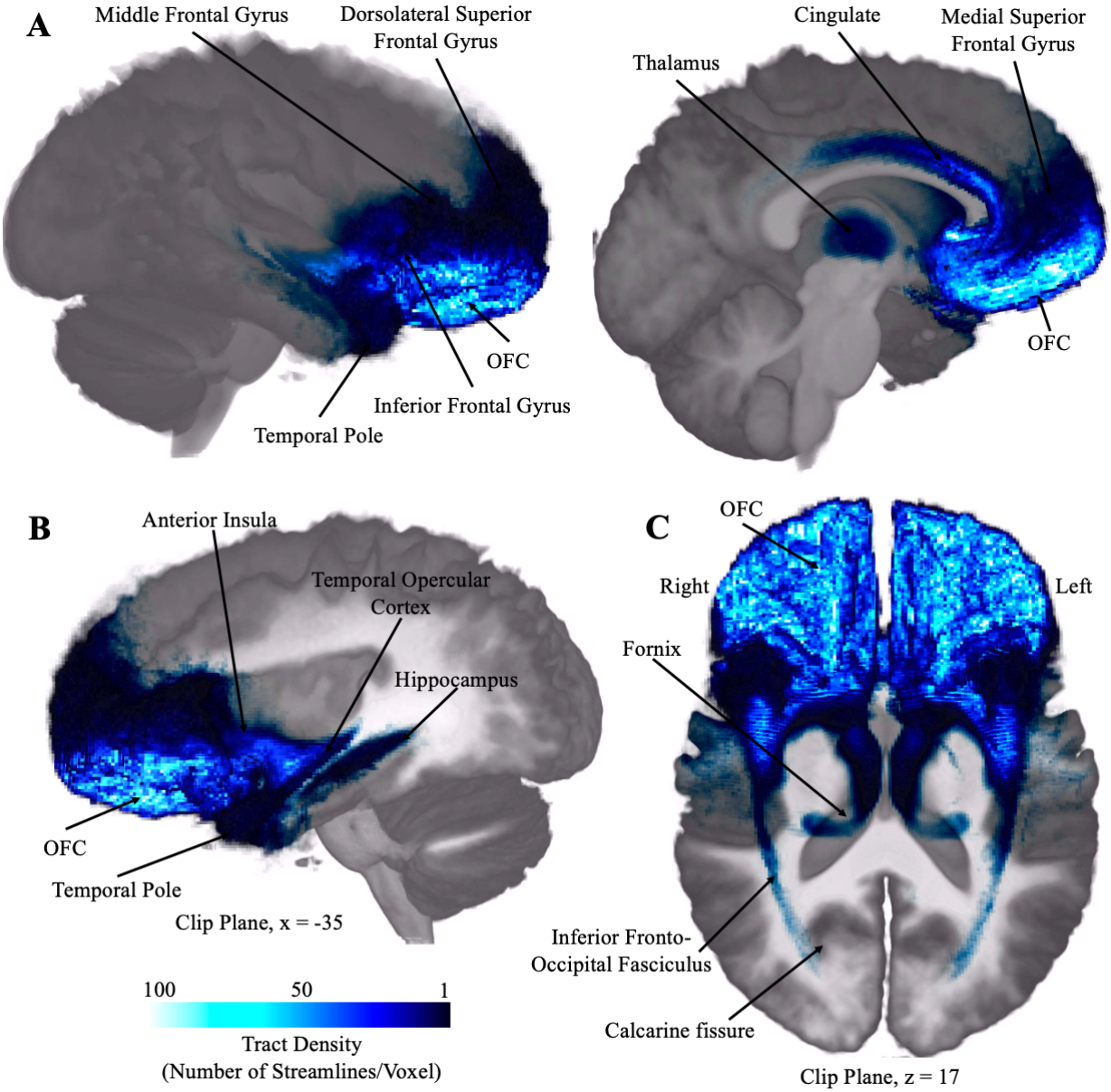

Figure 3.1. Cortical and hippocampal connectivity of the OFC. 3D-rendered average tract density maps are shown on the subjects' mean T1 image in MNI space, with partially transparent gray matter for visualization. **A**. Frontal, temporal, and cingulate connectivity, shown for the lateral side of the right hemisphere (left) and the medial wall of the left hemisphere (right). **B**. Insular, opercular, and hippocampal connectivity, shown in the left hemisphere. **C.** Axial view showing bilateral connectivity, featuring the inferior fronto-occipital fasciculus and the fornix.

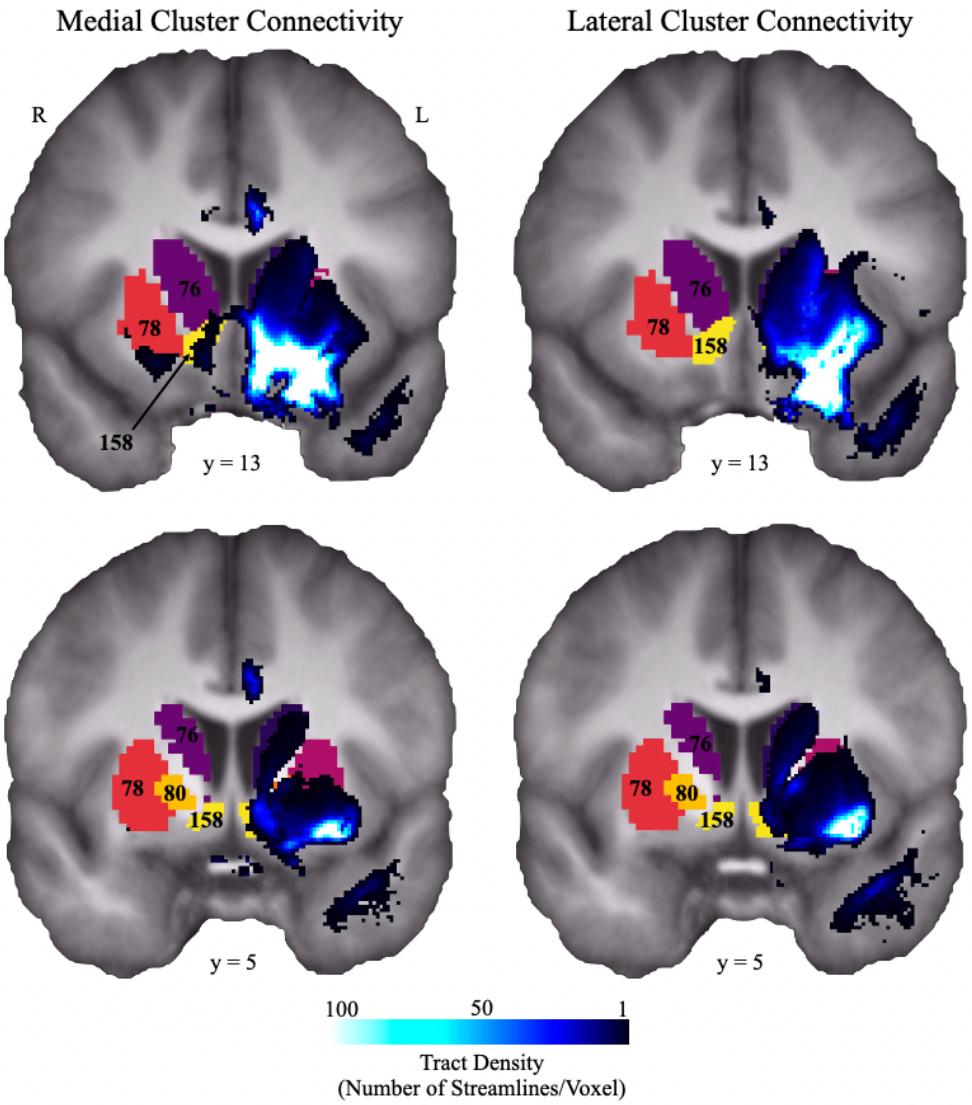

Figure 3.2. OFC connectivity with the basal ganglia. Average tract density maps show ipsilateral and contralateral basal ganglia connectivity with the left OFC, overlaid on a mean T1 image for all subjects. The AAL3 Atlas basal ganglia regions, including the caudate (76), putamen (78), globus pallidus (80), and nucleus accumbens (158) are labelled in the right hemisphere for reference. Left panels show K=2 Medial cluster connectivity, while right panels show K=2 Lateral cluster connectivity. The brightest regions (highest tract density, >100 streamlines per voxel) in the anterior (y=13) slices include voxels in the nucleus accumbens, ventral caudate, ventral putamen, olfactory cortex, anterior insula, and the external and extreme capsules. The brightest regions (highest tract density, >100 streamlines per voxel) in the posterior (y=5) slices include voxels in the ventral putamen and the external and extreme capsules.

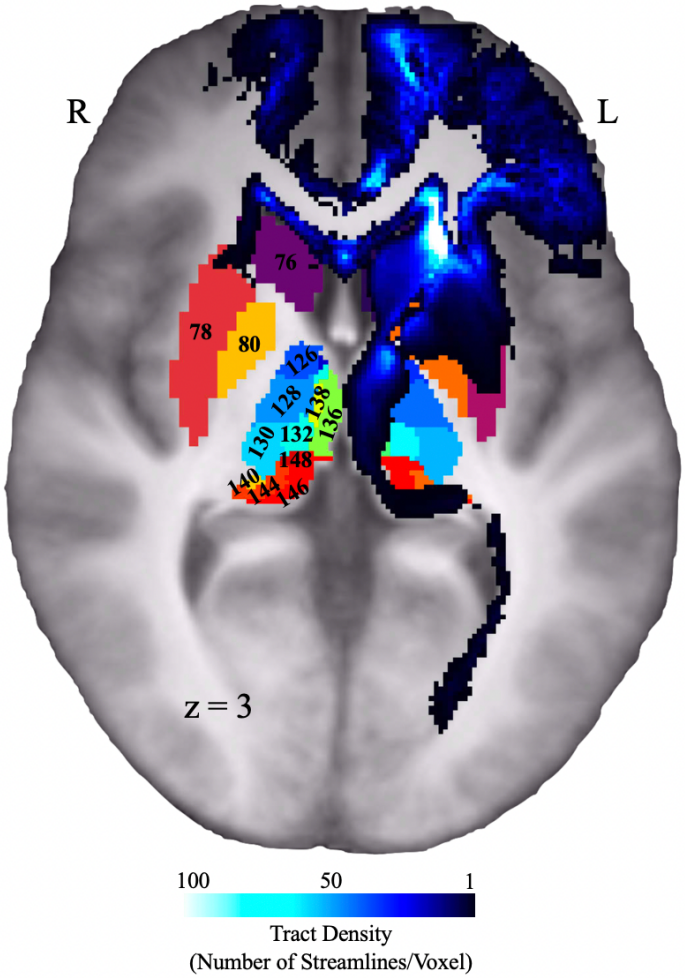

Figure 3.3. OFC connectivity with the thalamus and basal ganglia. Average tract density maps show ipsilateral and contralateral connectivity with the left OFC, overlaid on a mean T1 image for all subjects. The AAL3 Atlas regions of the basal ganglia (76, 78, & 80) and thalamus are labelled on the right hemisphere for reference. Labelled thalamic nuclei include the ventral anterior nucleus (126), ventral lateral nucleus (128), ventral posterolateral nucleus (130), intralaminar nucleus (132), medial and lateral divisions of the mediodorsal nucleus (136 & 138), lateral geniculate nucleus (140), and the anterior, medial, and lateral divisions of the pulvinar (144, 146, & 148).

K-means Clustering Results. We subdivided the OFC into clusters based on distinct anatomical connectivity patterns using a k-means clustering approach. We tested K=2-6 separately in each hemisphere and subject, and then for each clustering solution we generated normalized probabilistic maps of each cluster. The resulting probability maps for each clustering solution were largely similar across the two hemispheres (**Figure 3.4**). Probability maps for each cluster

were thresholded to include voxels that were assigned to that cluster in >20% of subjects, minimizing overlap between cluster probability maps.

For the K=2 solution, distinct medial and lateral clusters were identified. The medial clusters in both hemispheres covered gyrus rectus and the medial orbital gyrus in each hemisphere, while the lateral clusters covered the anterior orbital gyrus, posterior orbital gyrus, and lateral orbital gyrus.

For the K=3 solution, we identified distinct medial, lateral anterior, and lateral posterior clusters. In this clustering solution, the medial cluster was largely confined to gyrus rectus. The lateral anterior cluster covered the anterior orbital gyrus and the anterior portion of the medial orbital gyrus in each hemisphere. The lateral posterior cluster covered the lateral orbital gyrus, the posterior orbital gyrus, and the posterior portion of the medial orbital gyrus in each hemisphere.

For the K=4 solution, we identified medial, posterior, anterior, and lateral clusters in each hemisphere. In each hemisphere, the medial clusters covered gyrus rectus, the posterior clusters covered the posterior orbital gyrus and the posterior portion of the medial orbital gyrus, the anterior clusters covered the anterior orbital gyrus and the anterior portion of the medial orbital gyrus, and the lateral clusters covered the lateral orbital gyrus.

For the K=5 solution, we identified a medial cluster, lateral cluster, anterior cluster, posterior cluster, and central cluster. In each hemisphere, the medial cluster covered gyrus rectus. The lateral clusters covered the lateral portions of the anterior orbital gyrus. The anterior clusters covered the anterior-most portions of the medial orbital gyrus and the anterior orbital gyrus. The

posterior cluster covered the posterior orbital cluster and the posterior portion of the lateral orbital gyrus. The central cluster covered the posterior extend of the medial orbital gyrus.

For the K=6 solution, we identified an anterior medial cluster, a posterior medial cluster, a lateral cluster, an anterior cluster, a posterior cluster, and a central cluster. The posterior medial clusters covered the posterior half of gyrus rectus, while the anterior medial clusters covered the anterior half of gyrus rectus. The central clusters covered the posterior two-thirds of the medial orbital gyrus. The anterior clusters covered the anterior orbital gyrus and the anterior third of the medial orbital gyrus. The lateral clusters covered the lateral orbital gyrus, and the posterior clusters covered the posterior orbital gyrus.

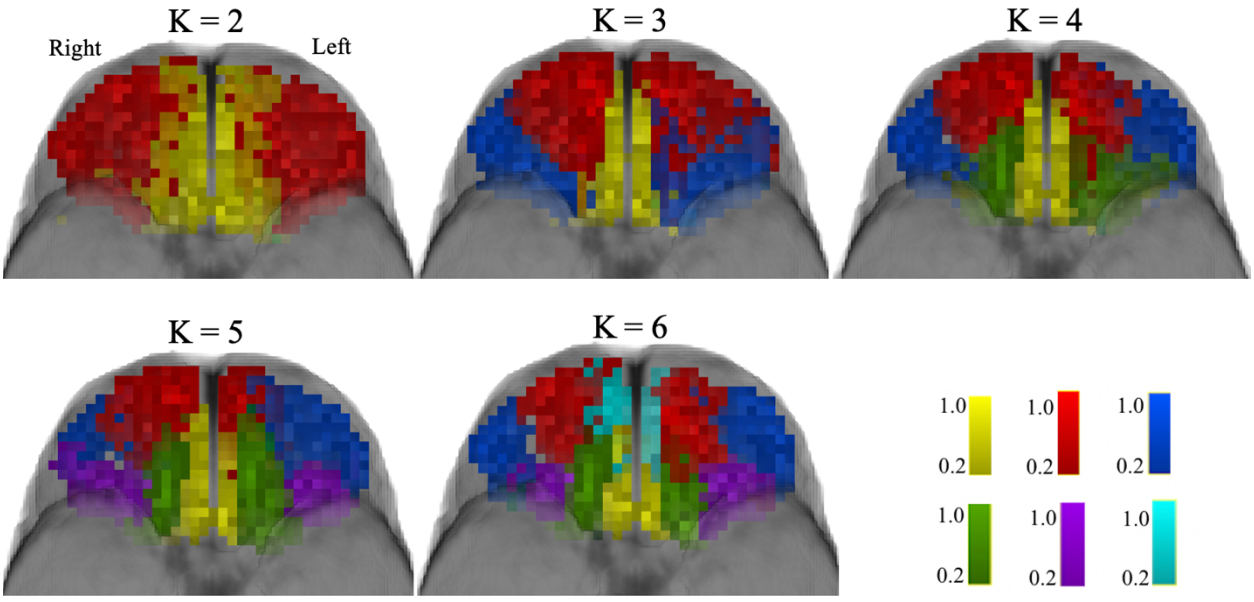

Figure 3.4. 3D-rendered probabilistic maps showing the OFC K-means clustering solutions for K=2-6. Maps are thresholded at 0.2, so that each voxel shown is a part of the indicated cluster in at least 20% of subjects. **K=2**: lateral cluster, red; medial cluster, yellow. **K=3**: lateral anterior cluster, red; lateral posterior cluster, dark blue; medial cluster, yellow. **K=4**: lateral cluster, dark blue; anterior cluster, red; posterior cluster, green; medial cluster, yellow. **K=5**: lateral cluster, dark blue; anterior cluster, red; posterior cluster, purple; central cluster, green; medial cluster, yellow. **K=6**: lateral cluster, dark blue; posterior cluster, purple; anterior cluster, red; central cluster, green; anterior medial cluster, cerulean; posterior medial

Ipsilateral Connectivity of OFC Subregions. The connectivity patterns of the K=2 cluster solution medial and lateral clusters are provided in **Table 3.2**, and of the K=3 cluster solution medial, anterior, and posterior clusters are provided in **Table 3.3**. It is worth nothing that although two clusters may have a similar degree of connectivity with an AAL3 region, this does not necessarily mean that they share connectivity with the same voxels within that region, or have the same topographical organization in their connections. An example of this is shown in **Figure 3.2**, where the medial and lateral clusters have similar connection strengths with the striatum, but their strongest projections are to different regions within the striatum.

Table 3.2: Ipsilateral Connectivity of the K=2 Medial and Lateral OFC Clusters

		Medial Clusters		Lateral Clusters	
AAL Region Name	**AAL Label**	**Left**	**Right**	**Left**	**Right**
Superior frontal gyrus, dorsolateral	3,4	28.0	20.6	33.1	37.6
Superior frontal gyrus, medial	19,20	11.5	10.5	7.9	6.8
Superior frontal gyrus, medial orbital	21,22	142.6	115.8	71.3	72.4
Middle frontal gyrus	5,6	23.7	14.9	52.9	38.1
Inferior frontal gyrus, opercular part	7,8			1.4	1.4
Inferior frontal gyrus, triangular part	9,10	4.2	4.3	10.1	7.7
Inferior frontal gyrus, pars orbitalis	11,12	21.9	42.3	177.3	151.4
Superior temporal gyrus	85,86	2.0	1.9	2.2	1.9
Temporal pole: superior temporal gyrus	87,88	3.1	10.4	7.7	6.9
Middle temporal gyrus	89,90	1.5	1.5	1.7	1.8
Temporal pole: middle temporal gyrus	91,92	2.6	2.7	3.4	3.0
Inferior temporal gyrus	93,94	1.3	1.2	1.7	1.5

Fusiform gyrus	59,60	1.3	1.5	1.7	1.9
Insula	33,34	12.8	21.5	34.0	29.5
Rolandic operculum	13,14			1.1	
Olfactory cortex	17,18	86.0	69.1	15.0	18.7
Calcarine fissure	47,48	1.1			
Lingual gyrus	51,52	1.4	1.3	1.9	1.5
Precuneus	71,72	1.4	1.1		
Middle cingulate & Paracingulate Gyri	37,38	4.8	2.5	1.4	1.4
Posterior cingulate gyrus	39,40	1.7	1.2		
Anterior cingulate cortex, subgenual	151,152	75.2	31.1	2.9	7.5
Anterior cingulate cortex, pregenual	153,154	16.6	4.9	5.3	2.0
Anterior cingulate cortex, supracallosal	155,156	17.5	9.6	2.6	2.8
Amygdala	45,46	3.5	6.8	3.2	6.7
Hippocampus	41,42	1.8	2.0	2.4	2.6
Parahippocampal gyrus	43,44	3.7	2.2	3.0	2.0
Caudate nucleus	75,76	20.6	18.8	17.5	17.5
Lenticular nucleus, Putamen	77,78	16.9	21.3	22.2	21.9
Lenticular nucleus, Pallidum	79,80	3.6	3.2	4.6	4.3
Nucleus accumbens	157,158	122.5	90.5	28.7	22.1
Thalamus, Anteroventral Nucleus	121,122	3.5	2.5	8.8	4.4
Lateral posterior	123,124	1.2	1.3	1.9	3.1
Ventral anterior	125,126	4.3	4.9	11.2	13.7
Ventral lateral	127,128	1.5	1.9	2.6	4.1
Ventral posterolateral	129,130		1.1		1.7
Intralaminar	131,132	3.7	3.8	9.9	4.6
Reuniens	133,134	2.3	2.9	6.1	5.2
Mediodorsal medial magnocellular	135,136	2.6	2.1	5.2	4.0
Mediodorsal lateral parvocellular	137,138	1.7	2.4	3.5	6.4
Lateral geniculate	139,140	1.5	1.6	2.2	2.3
Medial geniculate	141,142	1.1		1.4	1.0
Pulvinar anterior	143,144	1.3	1.3	1.9	1.9

Pulvinar medial	145,146	1.2	1.3	1.7	2.0
Pulvinar lateral	147,148	1.1	1.3	1.8	2.5
Pulvinar inferior	149,150				1.4

Table 3.2. Ipsilateral connectivity of the medial and lateral OFC clusters, from the K=2 cluster solution. Connectivity of each OFC cluster with regions in the AAL3 Atlas were assessed using probabilistic tractography. SIFT2-weighted streamline counts (R. E. Smith et al., 2015b) were averaged across voxels in each AAL3 region that received streamlines from the OFC to produce these recorded tract density values. Darker blue cells indicate regions with higher tract density, reflecting stronger anatomical connectivity.

In the K=2 cluster solution, the medial-lateral OFC divide is apparent. In the frontal cortex, both medial and lateral clusters show strong connectivity with the superior frontal gyrus (dorsolateral, medial, and medial orbital parts), middle frontal gyrus, and inferior frontal gyrus (triangular part and pars orbitalis). The medial clusters show stronger connectivity than the lateral clusters with the medial and medial orbital parts of the superior frontal gyrus. The lateral clusters, however, show stronger connectivity with the dorsolateral superior frontal gyrus, the middle frontal gyrus, and the inferior frontal gyrus.

In the temporal cortex, we found that connectivity with the fusiform gyrus, superior temporal gyrus, temporal pole, middle temporal gyrus, and inferior temporal gyrus were comparable across both the medial clusters and the lateral clusters. Both clusters showed strong connectivity with the temporal opercular cortex and the anterior insular cortex, though the connectivity with the lateral clusters was stronger for both of these regions than with the medial clusters. Conversely, while both clusters showed strong connectivity with the primary olfactory cortex, the medial clusters had much stronger connectivity with this region than the lateral clusters.

In the parietal cortex, the medial clusters shared weak connectivity with the precuneus, middle cingulate, and the posterior cingulate gyrus. The middle cingulate also shared weak

connectivity with the lateral clusters. In the occipital cortex, both clusters shared weak connectivity with the lingual gyrus, while only the left medial cluster shared weak connectivity with the cortex of the calcarine fissure.

In the anterior cingulate cortex, connectivity was very strong with the medial OFC clusters, especially in the left hemisphere, though weaker connections were also present with the lateral OFC clusters. Connections with the hippocampus, amygdala, and parahippocampal gyrus were comparable across medial and lateral clusters. The nucleus accumbens showed strong connectivity with the lateral clusters, but much stronger connectivity with the medial clusters (**Figure 3.2**). Connectivity with the GMWMI voxels adjacent to the hypothalamus was only observed from the medial clusters.

In the basal ganglia, the strength of connectivity was comparable between the medial and lateral clusters across the caudate, putamen, and globus pallidus. However, we found that the medial clusters projected to more ventromedial parts of the caudate and putamen, while the lateral clusters projected to more ventrolateral parts of the caudate and putamen (**Figure 3.2**). The thalamic nuclei with strongest OFC connectivity, including the mediodorsal nucleus, reuniens, intralaminar nucleus, ventral anterior nucleus, and anteroventral nucleus, all had stronger connectivity with the lateral clusters compared to the medial clusters.

In the K=3 clustering solution, the medial cluster is narrowed, while the lateral cluster is divided into anterior and posterior parts, illustrating the rostro-caudal organization of the OFC. In the following text, emphasis will be placed on differences between the anterior and posterior clusters of the lateral OFC.

In the frontal cortex, connectivity with the superior frontal gyrus is much stronger for the anterior cluster compared to the posterior cluster. For the anterior clusters, connectivity is strongest in the medial orbital part of the superior frontal gyrus, followed by the dorsolateral part, and the medial part. The posterior clusters show stronger connectivity with the dorsolateral and medial orbital parts than with the medial part. Connectivity with the middle frontal gyrus is comparable across anterior and posterior clusters. In contrast to the superior frontal gyrus, connectivity with the inferior frontal gyrus is much stronger for the posterior clusters compared to the anterior clusters. Connectivity is strongest across both clusters for pars orbitalis of the inferior frontal gyrus, followed by the triangular part. Both anterior and posterior clusters share weak connectivity with the opercular part of the inferior frontal gyrus.

In the temporal cortex, the anterior and posterior clusters share comparable connectivity with the superior temporal gyrus, the temporal pole, the middle temporal gyrus, the inferior temporal gyrus, and the fusiform gyrus. The posterior cluster showed slightly stronger connectivity with the temporal polar portion of the superior temporal gyrus compared to the anterior clusters. In addition, the posterior cluster had much stronger connectivity with the insula and the temporal opercular cortex compared with the anterior clusters. The anterior and posterior clusters had comparable connectivity with the primary olfactory cortex, although olfactory connectivity with the medial cluster was much stronger than for either of the lateral clusters. In the parietal and occipital regions, neither of the lateral clusters showed connectivity with the precuneus, posterior cingulate gyrus, or calcarine fissure cortex. Weak connectivity with the lingual gyrus was present for both the anterior and posterior clusters. Weak bilateral connectivity

with the middle cingulate was present in the anterior clusters, and unilaterally in the left posterior cluster.

While much weaker than with the medial clusters, connectivity with the anterior cingulate cortex was generally higher for the anterior cluster than for the posterior cluster. In the posterior cluster, connectivity with the anterior cingulate was stronger in the left hemisphere than in the right hemisphere. Connectivity with the hippocampus, parahippocampal gyrus, and amygdala was comparable across anterior and posterior clusters. Connectivity with the nucleus accumbens was comparable across both anterior and posterior clusters, while nucleus accumbens connectivity with the medial cluster was much stronger in comparison. Connectivity with each of the thalamic nuclei and with each of the basal ganglia nuclei was comparable across anterior and posterior clusters.

Table 3.3: Ipsilateral Connectivity of the K=3 Medial, Anterior, and Posterior OFC Clusters

		Medial Cluster		Anterior Cluster		Posterior Cluster	
AAL Region Name	**AAL Label**	**Left**	**Right**	**Left**	**Right**	**Left**	**Right**
Superior frontal gyrus, dorsolateral	3,4	12.8	6.3	45.1	48.9	11.1	8.4
Superior frontal gyrus, medial	19,20	10.0	10.2	9.9	8.3	3.6	2.6
Superior frontal gyrus, medial orbital	21,22	125.7	112.9	105.4	94.2	14.7	8.4
Middle frontal gyrus	5,6	2.3	2.1	47.6	31.4	35.4	30.0
Inferior frontal gyrus, opercular part	7,8			1.2	1.2	1.3	1.3
Inferior frontal gyrus, triangular part	9,10	1.3	1.4	6.4	3.2	8.1	8.3
Inferior frontal gyrus, pars orbitalis	11,12	2.7	2.2	87.0	24.4	122.9	171.0
Superior temporal gyrus	85,86	2.0	1.6	1.9	1.5	2.2	1.9

Temporal pole: superior temporal gyrus	87,88	2.8	7.7	4.6	5.5	7.1	7.5
Middle temporal gyrus	89,90	1.5	1.4	1.6	1.4	1.5	1.7
Temporal pole: middle temporal gyrus	91,92	2.2	2.3	2.5	2.4	3.2	2.9
Inferior temporal gyrus	93,94	1.2	1.3	1.4	1.2	1.6	1.4
Fusiform gyrus	59,60	1.5	1.2	1.3	1.5	1.6	1.8
Insula	33,34	10.7	15.1	14.3	21.5	31.6	29.6
Olfactory cortex	17,18	83.9	68.6	9.1	20.2	20.7	11.8
Calcarine fissure	47,48	1.0					
Lingual gyrus	51,52	1.2	1.2	1.4	1.3	1.8	1.5
Precuneus	71,72	1.4	1.1				
Middle cingulate & Paracingulate Gyri	37,38	4.8	2.5	1.3	1.5	1.3	
Posterior cingulate gyrus	39,40	1.7	1.2				
Anterior cingulate cortex, subgenual	151,152	75.9	33.4	3.1	5.8	3.9	1.4
Anterior cingulate cortex, pregenual	153,154	16.7	5.2	5.9	1.7	3.0	1.3
Anterior cingulate cortex, supracallosal	155,156	17.6	9.7	2.7	3.2	2.7	1.2
Amygdala	45,46	3.5	5.9	3.0	5.9	3.2	6.1
Hippocampus	41,42	1.5	1.6	1.7	1.9	2.2	2.4
Parahippocampal gyrus	43,44	1.8	2.1	1.7	1.7	3.8	1.9
Caudate nucleus	75,76	20.4	17.7	15.4	17.2	11.9	9.5
Lenticular nucleus, Putamen	77,78	14.7	17.2	15.7	17.6	17.1	18.1
Lenticular nucleus, Pallidum	79,80	3.4	2.9	3.8	3.1	3.1	3.5
Nucleus accumbens	157,158	113.1	75.0	20.4	33.6	39.0	13.9
Thalamus, Anteroventral Nucleus	121,122	1.9	1.8	6.5	2.8	4.7	3.3
Lateral posterior	123,124		1.0	1.5	1.7	1.3	2.4
Ventral anterior	125,126	2.8	2.7	8.4	6.7	6.4	10.1
Ventral lateral	127,128	1.1	1.3	2.2	2.4	1.9	3.4

Ventral posterolateral	129,130				1.1		1.6
Intralaminar	131,132	2.4	2.9	7.5	3.6	5.6	3.5
Reuniens	133,134	1.8	2.7	3.8	3.1	3.5	3.3
Mediodorsal medial magnocellular	135,136	1.8	1.7	3.9	2.4	3.1	2.8
Mediodorsal lateral parvocellular	137,138	1.1	1.5	2.8	3.2	2.3	4.6
Lateral geniculate	139,140	1.4	1.2	1.5	1.6	1.9	2.1
Medial Geniculate	141,142	1.1				1.3	
Pulvinar anterior	143,144	1.3	1.1	1.3	1.3	1.7	1.7
Pulvinar medial	145,146	1.1	1.1	1.6	1.5	1.4	1.7
Pulvinar lateral	147,148			1.5	1.4	1.2	2.1
Pulvinar inferior	149,150						1.3

Table 3.3. Ipsilateral connectivity of the medial, anterior, and posterior OFC clusters, from the K=3 cluster solution. Connectivity of each OFC cluster with regions in the AAL3 Atlas were assessed using probabilistic tractography. SIFT2-weighted streamline counts (R. E. Smith et al., 2015b) were averaged across voxels in each AAL3 region that received streamlines from the OFC to produce these recorded tract density values. Darker blue cells indicate regions with higher tract density, reflecting stronger anatomical connectivity.

3.5 Discussions

In the present study, we characterized the widespread cortical and subcortical connectivity of the human OFC, and then used a K-means clustering approach to divide the OFC into distinct subregions based on differences in anatomical connectivity patterns across voxels. We found that the human OFC shares strong connectivity with multimodal sensory cortex, prefrontal cortex, cortical and subcortical limbic regions, the basal ganglia, and the thalamus.

The connectivity of the human OFC shares many similarities with that of the macaque, and our results are in alignment with theories regarding human OFC involvement in multimodal sensory integration, memory for motivationally-salient stimuli, encoding of reward values across contexts, visceral and emotional regulation, and coordinating goal-oriented behavior.

For the K=2 clustering solution, we identified distinct, symmetrical medial and lateral OFC clusters in each hemisphere. This finding is in agreement with previous literature on the macaque OFC anatomical connectivity, wherein distinct medial and lateral OFC networks have been described and dissociable roles for each network have been proposed (Carmichael & Price, 1996). The lateral OFC network of the macaque receives heavy sensory inputs from every sensory modality, and is thought to be involved in multimodal sensory integration and encoding the specific identity and valence of motivationally-salient stimuli. The macaque medial OFC network, in contrast, was found to share much stronger connectivity with limbic and visceromotor regions, and is likely involved in regulating visceral and emotional responses. In our K=3 clustering solution, we found that the medial cluster was preserved, but narrowed, and the lateral cluster split into anterior and posterior clusters. This anterior-posterior division appears to mirror the cytoarchitectonic organization between anterior and posterior OFC, observed in both the human and the macaque (Carmichael & Price, 1994; Ongür et al., 2003b; Petrides & Pandya, 2002). Anterior OFC cortex has a denser granule cell layer, and tends to share connectivity with other regions of granular cortex, while posterior OFC cortex is dysgranular and agranular, and tends to share connectivity with other dysgranular and agranular cortical regions. For K=4-6, we identified increasingly more complex, but still symmetrical clustering solutions across each OFC hemisphere. In our K=5 clustering solution, we found five

clusters that corresponded roughly to the five major OFC gyri, including the gyrus rectus, medial orbital gyrus, lateral orbital gyrus, anterior orbital gyrus, and posterior orbital gyrus. This suggests that the sulcogyral morphology of this region may indeed be related to this region's anatomical connectivity. Variability in OFC sulcogyral morphology has been identified in humans, and participants can be classed into four major OFC sulcogyral subtypes (Chiavaras et al., 2001). Further research investigating differences in anatomical connectivity across participants with differing OFC sulcogyral subtypes may provide insight into individual differences in OFC organization and function. In our K=6 clustering solution, we identified a more complex organization that roughly corresponds to identified cytoarchitectural boundaries in the human OFC (Ongür et al., 2003b). The lateral clusters (dark blue, **Figure 3.4**) corresponded roughly to area 47/12 along the posterior-lateral edge of the OFC. The posterior clusters (purple) corresponded to agranular insular cortex. The anterior clusters (red) encompassed the lateral portions of areas 10 and 11, while the medial anterior clusters (cerulean) encompassed the medial portions of these two areas. The central cluster (green) and the posterior medial cluster (yellow) then each encompassed areas 13 and 14, respectively. These results suggest that the previously identified cytoarchitectural regions of the human OFC can additionally be dissociated by differing patterns of anatomical connectivity with the rest of the brain.

In our data, we identified widespread OFC connectivity with sensory cortex. Connectivity with primary olfactory cortex, primary gustatory cortex, insular visceral cortex, and temporal opercular auditory cortex was substantial. The OFC also shared strong connectivity with temporal visual areas, including regions in the inferior temporal gyrus and fusiform gyrus involved in the visual "what" pathway, as well as weaker connections between the OFC and

earlier visual cortex in the lingual gyrus and calcarine fissure. Similar to the macaque, we found that sensory connections are generally denser in the lateral OFC compared to the medial OFC, with exceptions for olfaction and vision. In our study, we found that connectivity with auditory cortex, gustatory cortex, and anterior insular cortex related to visceral sensation and interoception was much stronger with the lateral OFC clusters than the medial OFC clusters. In contrast, we found that the primary olfactory cortex had very strong connectivity with both medial and lateral clusters, but connectivity with the medial clusters was stronger. Temporal lobe visual areas and the occipital lobe lingual gyrus had roughly equal connectivity with both the medial and lateral OFC clusters. Medial parietal areas involved in visuospatial processing, including the precuneus and posterior cingulate cortex, shared weak connectivity with the medial OFC clusters, but not the lateral OFC clusters. Surprisingly, we did not find any OFC connectivity with primary somatosensory cortex or parietal somatosensory association cortex, although these regions share connectivity with area 12o in the posterior lateral OFC of the macaque (Carmichael & Price, 1995b). Another recent dMRI study investigating connectivity of the human OFC also failed to find OFC connectivity with somatosensory regions, but did find bilateral connectivity between the adjacent inferior frontal gyrus and parietal area 7 and the supramarginal gyrus (Hsu et al., 2020).

In our study, we found strong OFC connectivity with prefrontal cortex. The medial OFC clusters shared stronger connectivity with the anterior cingulate gyrus and ventromedial prefrontal cortex (vmPFC; including AAL3 medial and medial orbital superior frontal gyrus), regions involved in processing motivationally- and emotionally-salient stimuli, and regulating emotional and behavioral responses. The lateral OFC clusters, in contrast, shared stronger

connectivity with lateral prefrontal cortex. In our K=3 clustering solution, the lateral OFC was split into anterior lateral and posterior lateral clusters, each of which had differentiable connectivity with prefrontal cortical regions. The dorsolateral and medial orbital parts of the superior frontal gyrus were more strongly connected with the anterior lateral OFC clusters. The dorsolateral prefrontal cortex (dlPFC) is involved in executive functions including planning, working memory, task-switching, and preventing distractions from interfering with current goal-directed behaviors (Panikratova et al., 2020; Robbins et al., 1996). The lateral OFC may thus serve as an important source of highly integrated, motivationally-salient sensory information to the dlPFC, and the connectivity between these two regions is likely important for coordinating goal-directed behaviors. The inferior frontal gyrus, in contrast, was more strongly connected with the posterior lateral OFC clusters. The inferior frontal gyrus is the site of Broca's area, and is involved in speech production (Dronkers et al., 2007). A strong link between OFC regions involved in processing motivationally-salient stimuli and the inferior frontal gyrus regions involved in speech production would allow for quick and efficient verbal communication regarding potential rewarding or threatening environmental stimuli.

We also observed substantial subcortical connectivity with the OFC. We found that OFC connectivity with the striatum was organized topographically, in that the medial OFC clusters had stronger connectivity with the ventromedial caudate and putamen, while the lateral OFC clusters had stronger connectivity with the ventrolateral caudate and putamen. The nucleus accumbens shared strong connectivity with both the medial and lateral clusters, although this connectivity was much stronger with the medial clusters. This same topography is also observed in the macaque (Ferry et al., 2000; Haber et al., 1995; Haber & Knutson, 2010). These cortico-

striatal connections are important for reinforcement learning and reward processing. In addition, the amygdala, hippocampus, and parahippocampal gyrus shared connectivity throughout the OFC, while the GMWMI adjacent to the hypothalamus shared connectivity with the medial OFC clusters. The network formed by the amygdala with vmPFC, the ventral striatum, and the mediodorsal nucleus of the thalamus is important for proper emotional responses and emotional learning in response to motivationally-salient stimuli. We found that the OFC shares connectivity with each of these regions, suggesting a role for the OFC in emotional learning. Patients with OFC lesions are generally able to learn the initial reward value of a stimulus, but then have trouble updating these reward values in reversal learning tasks (Berlin et al., 2004; Rudebeck & Rich, 2018). Perhaps the initial stimulus-reward association is learned through the amygdala, but later recognition of changes to this association and updating of these reward-stimulus associations may be mediated by the OFC. Further, the OFC shares connectivity with several regions involved in the Papez circuit, important for spatial and episodic memory, including the hippocampus, hypothalamus, anterior nucleus of the thalamus, posterior cingulate cortex, and parahippocampal cortex. OFC connectivity with this circuit may be important for tracking changing reward contingencies across changing spatial and temporal contexts. The OFC further shares interconnectivity both with anterior insular regions important for incoming visceral and interoceptive sensory signals, and the hypothalamus, important for homeostatic regulation. The OFC may then serve as a relay to coordinate activity between these visceral brain systems and higher-order executive systems in the prefrontal cortex. This would allow for internal monitoring of physiologic states, and coordination of adaptive goal-oriented behaviors in response to visceral and physiologic needs.

Several brain-wide functional networks have been proposed that serve important roles for the regulation of human behavior. Three networks of important consideration include the Central Executive Network (also known as the fronto-parietal network), the Salience Network (or ventral attention network), and the Default Mode Network (S. T. Witt et al., 2021). The default mode network involves the vmPFC, hippocampus, angular gyrus, precuneus, and posterior cingulate cortex, and is thought to be involved in internally-directed cognition and mind wandering. In our data, we found that the medial OFC clusters shared very strong connectivity with the vmPFC, as well as connectivity with the hippocampus, the precuneus and the posterior cingulate cortex. The lateral OFC additionally shared weaker connectivity with vmPFC and the hippocampus. Medial OFC functions involving visceromotor and emotional regulation may very well be influenced by interactions with the default mode network, and these interactions may be important for maintaining an accurate representation of current internal emotional and physiological states. The central executive network, in contrast, involves the dlPFC (especially the middle frontal gyrus) and posterior parietal cortex, and is especially active when engaged in cognitively demanding goal-oriented tasks. The lateral OFC shares strong connectivity with dlPFC regions involved in the central executive network, and the medial OFC shares weaker connectivity with these regions. The lateral OFC has been implicated in reward memory, encoding identity- and value-specific information about incoming stimuli, and predicting future expected outcomes in value-based decision making tasks (Howard et al., 2015, 2020; Howard & Kahnt, 2021). Interactions between the lateral OFC and the dlPFC central executive regions are likely critical for flexibly adapting and updating our behaviors in order to stay on task and reach a particular goal.

Lastly, we found that both medial and lateral OFC share very strong connectivity with the brain regions involved in the salience network, including the anterior cingulate cortex, anterior insular cortex, amygdala, and ventral striatum. The salience network is involved in shifting attention in response to motivationally-salient stimuli, and is thought to help facilitate transitions between default mode network activity and central executive network activity. It has been suggested that the OFC maintains and updates a "cognitive map" of relationships between learned predictive cues, behavioral actions, and outcomes of those actions (Wikenheiser & Schoenbaum, 2016). The OFC then may play a role alongside the salience network in discriminating which incoming stimuli are important or relevant to the current task and should be allowed to influence the activity of the central executive network, versus those salient environmental stimuli that should be ignored as distractions.

The OFC is thus uniquely situated to be able to regulate interactions between these three networks. Medial OFC regions may monitor internal states and physiological needs through interactions with the default mode network and visceromotor structures such as the hypothalamus, while the lateral OFC encodes stimulus reward values and predictions about behavioral outcomes that serve as motivating factors for central executive activity. Incoming salient sensory information activates the salience network, and may tip the balance between default mode and central executive network activity. OFC interactions with the salience network can help to determine which incoming stimuli should interrupt central executive function, versus which stimuli should be ignored. This ensures that the goal-directed activity of the central executive network sufficiently meets internal physiological needs, and that it can be overridden or altered to better meet those needs. Attention Deficit/Hyperactivity Disorder (ADHD) is a

disorder characterized by dysregulated attention, impaired executive function, poor working memory, impaired performance on reward and reversal learning tasks, and poor interoceptive awareness (Brown, 2009; Itami & Uno, 2002; Kutscheidt et al., 2019). OFC dysfunction and OFC gray matter abnormalities have been reported in ADHD (Fernández-Jaén et al., 2014; Itami & Uno, 2002; Tegelbeckers et al., 2018; Yang et al., 2019), in addition to dysfunction and reduced integrity of the central executive, ventral attention, and default mode networks (Janssen et al., 2017; Silk et al., 2008; Uddin et al., 2008; Yerys et al., 2019). Alongside our data describing the anatomical connectivity of the OFC with these three brain networks, observations in the ADHD literature provide further support for the hypothesis that the OFC plays an active role in regulating interactions between these networks, and is necessary for flexible and adaptive goal-oriented behaviors.

In the present study, we have provided an in-depth characterization of the anatomical connectivity of the human OFC, based on an optimized dMRI and tractography pipeline that allowed us to image the OFC with few artifacts. We further used a K-means parcellation technique to divide the OFC into unique subregions based on differences in anatomical connectivity. Our results provide an in-depth look at the brain-wide anatomical connectivity and intrinsic organization of the OFC, and provide insight into the complex functional role of this brain region. Future investigations into specific pathways of the OFC, their microstructural properties, and their relationships with human behavior will help to further elucidate the mechanistic role of the OFC in regulating human behavior.

3.6 Acknowledgements & Author Contributions

This work was supported by the National Institute on Deafness and Other Communication Disorders grant R01 DC015426 (to T.K.), the Neuroscience of Human Cognition Training Program NIH grant T32 NS047987 (to S.L.E.-C.), and the Intramural Research Program at the National Institute on Drug Abuse (ZIA DA000642). The opinions expressed in this work are the authors' own and do not reflect the view of the NIH/DHHS.

Shiloh L. Echevarria-Cooper and Thorsten Kahnt designed the research approach. Shiloh L. Echevarria-Cooper performed the research, including collecting and analyzing the data.

Chapter 4: Validation of the NIH Toolbox Odor Identification Test across Normal Cognition, amnestic Mild Cognitive Impairment, and Alzheimer's Disease

4.1. Abstract & Significance

Olfactory impairments have been associated with aging, amnestic mild cognitive impairment (aMCI) and Alzheimer's disease (AD). Olfactory identification tests have been proposed as a cost-effective measure that may be able to distinguish between normal cognition (NC) and aMCI. The present study, as part of the Advancing Reliable Measurement in Alzheimer's Disease and Cognitive Aging (ARMADA) (Weintraub et al., 2021) parent study, was conducted to validate the NIH Toolbox Odor Identification Test (Dalton et al., 2013) across NC, aMCI, and AD participants over the age of 65 (N=389). We determined that scores on the Odor Identification Test significantly decreased with age (p=2.03e-09) and were significantly lower for aMCI (p=6.28e-08) and for AD (p< 2.0e-16) compared to NC controls after correcting for age and sex. Further, we determined that the Odor Identification Test has a sensitivity of 49.4% and specificity of 88.8% at a threshold of 0.50, for detecting aMCI compared to NC participants. The Area Under the Curve (AUC) was 0.78. Additionally, we found that Odor Identification Scores were significantly lower in participants with a positive AD biomarker test compared to those with a negative AD biomarker test (p = 0.005). Odor Scores were not found to differ significantly based on APOE ε4 allele carrier status. Finally, scores on the Odor Identification Test were evaluated for a NC sample aged 85-91, and were found to be significantly lower than scores from NC participants aged 65-84 (p = 0.000453). This study provides useful measures for the validation of the NIH Toolbox Odor Identification Test across

NC, aMCI, and AD diagnostic categories, and evidence for the usefulness of the NIH Toolbox Odor Identification Test for detecting aMCI compared to NC.

4.2. Introduction

Alzheimer's disease (AD) is a progressive neurodegenerative disorder affecting memory and cognition, leading to reduced independence, impaired ability to carry out the activities of daily life, and lower life expectancy (Mayeux & Stern, 2012). The progression from normal cognition (NC) to dementia of the Alzheimer's type is gradual, and involves an intermediary stage termed amnestic mild cognitive impairment (aMCI). In aMCI, memory impairments are present, but not severe enough to impact daily living (Petersen et al., 2014). Identifying individuals who are in the earliest disease stages and at high risk for converting to AD will help to target preventative measures and slow disease progression.

In addition to age, AD risk factors that may forewarn cognitive decline include carrying a copy of apolipoprotein E (APOE) ε4 allele (Corder et al., 1993), and preclinical presence of amyloid β and/or tau pathology (Braak & Braak, 1991, 1995; Jack et al., 2010; Vos et al., 2016). However, genotyping and testing for known AD biomarkers, involving PET scans with injected radioactive tracers or a lumbar spinal tap to evaluate cerebrospinal fluid markers, are expensive and invasive procedures. Typically, brain imaging, extensive cognitive testing, and evaluation by a specialist is required to diagnose aMCI in clinical settings (Doody et al., 2011). Identifying a quick, low-cost, and easily interpretable measure that can accurately flag individuals who are at risk of cognitive decline is thus imperative to lowering costs and earlier diagnosis (Weintraub et al., 2021).

Olfactory impairments have been proposed as indicators of the early stages of aMCI and AD (Albers et al., 2015; Murphy, 2019). Olfactory identification tests are simple to administer and may provide a time- and cost-effective way to identify individuals at risk of cognitive decline. While olfactory decline is observed in healthy aging (Doty & Kamath, 2014; Palmquist et al., 2020; Seubert et al., 2017), this decline appears to occur earlier and is more severe in individuals who go on to develop aMCI and AD (Bacon et al., 1998; Devanand et al., 2015; Roberts et al., 2016; Schubert et al., 2008; Wilson et al., 2007). Estimates suggest that 85-90% of individuals with AD have impaired olfaction (Morgan et al., 1995; Woodward et al., 2017), and the severity of olfactory impairment is correlated with the severity of cognitive impairment (Murphy et al., 1990; Yoo et al., 2018) and with the degree of tau pathology (Klein et al., 2021; Lafaille-Magnan et al., 2017).

The aim of the present study was to validate the NIH Toolbox Odor Identification Test (Dalton et al., 2013) in an elderly population ranging from NC to AD, as part of a multisite study, Advancing Reliable Measurement in Alzheimer's Disease and Cognitive Aging (ARMADA) (Weintraub et al., 2021). The NIH Toolbox Odor Identification Test is a 9-item multiple choice test that is administered via scratch-and-sniff cards and a computer or tablet, and can be easily interpreted by a primary care physician. Here, we characterized performance on the NIH Toolbox Odor Identification Test in a cohort of research participants involved in longitudinal research through Alzheimer's disease research centers (ADRCs) across the United States. We evaluated performance on the test across diagnostic categories, including NC, aMCI, and AD, while controlling for age and sex. We then validated the Odor Identification Test's ability to discriminate between aMCI and NC participants. In addition, we conducted two

additional analyses to evaluate relationships between scores on the Odor Identification Test with both APOE ε4 allele status and AD biomarker presence in a subset of participants with available genotype and/or biomarker data. Finally, as the NIH Toolbox was initially validated only in populations aged 65-85 (Dalton et al., 2013), we compared Odor Identification Scores between NC participants aged 65-84 and NC participants over age 85.

4.3. Materials and Methods

The purpose of the present study was to validate the NIH Toolbox Odor Identification Test for a general population cohort of adults over age 65, across NC, aMCI, and AD diagnoses. The dataset used in the present study was obtained through the overarching ARMADA study (Weintraub et al., 2021). Participants in the ARMADA study were recruited across nine separate study sites, including Northwestern University (NU), University of Michigan (UM), University of Wisconsin-Madison (UW-M), Mayo Clinic-Jacksonville, Florida (MCF), University of Pittsburgh (UPitt), Emory University, University of California-San Diego (UCSD), Columbia University, and Massachusetts General Hospital (MGH). Participants were recruited from existing research cohorts in this network of Alzheimer's disease research centers (ADRCs) funded by the National Institute on Aging (NIA) and other NIH-funded longitudinal studies that use similar methods to the ADRC longitudinal studies. Emphasis was placed on recruiting participants so that the resulting general population dataset is racially representative of the United States population. Additionally, emphasis was placed on recruiting NC participants over the age of 85 in order the validate the NIH Toolbox Odor Identification Test for this age group. Available data through the ARMADA study includes scores on the NIH Toolbox tests (Gershon

et al., 2013; Hodes et al., 2013), measures of cognitive functioning, health history, and mental health history through the Uniform Data Set (UDS) (Morris et al., 2006; Weintraub et al., 2018); and, for a subset of participants, APOE genotype and/or AD biomarker testing results (cerebrospinal fluid (CSF) and/or a-beta PET imaging) were also available.

NIH Toolbox Odor Identification Test. The NIH Toolbox Odor Identification Test (Dalton et al., 2013) is a 9-item test administered to participants by a facilitator. The test includes 9 odors on scratch-and-sniff cards. For each odor, the participant must choose from four options, including one correct response and three distractor options. Each option is presented with picture and word descriptors on a computer or tablet screen, and read aloud by the facilitator. Scores are recorded as integer values ranging from 0-9, with chance performance at 25%, or roughly a score of 2.

Study Participants. Data collected from N=389 participants as part of the overarching ARMADA study were included in the present study. Participants were included for analysis in the present study if they 1) had completed the NIH Toolbox Odor Identification Test; and 2) had no record in the UDS dataset of previous traumatic brain injury or stroke, both of which may affect olfactory ability (Howell et al., 2018; Wehling et al., 2015). Participants were divided into three research diagnostic categories, including normal cognition (NC), amnestic mild cognitive impairment (aMCI), and Alzheimer's disease (AD). Diagnostic categories were assigned based on neurocognitive testing alongside the participant's CDR score. A score of 0.0 was required for NC, a score of 0.5 for aMCI, and a score greater than or equal to 1.0 for AD. In the NC group, emphasis was placed on recruiting participants over the age of 85 in order to validate the NIHTB

Odor Identification Test for this age group. A summary of participant demographics across diagnostic categories is provided in **Table 4.1**.

Table 4.1: Participant Demographics				
Emphasis Group	**Diagnosis**	**N**	**Male vs. Female**	**Age (Years)**
General Population (Ages 85+)	Normal Cognition	96	42 Male 54 Female	87.7 +/- 2.1
General Population (Ages 65-84)	Normal Cognition	152	50 Male 102 Female	72.7 +/- 5.1
General Population	Mild Cognitive Impairment	79	47 Male 32 Female	77.3 +/- 6.9
General Population	Dementia	62	34 Male 28 Female	75.4 +/- 7.2
		389	173 Male 216 Female	77.8 +/- 8.0

APOE genotype data was available for N=275 participants. Participants were collapsed into two groups, an ε4 allele positive group (at least one ε4 allele, N=98) and an ε4 allele negative group (no ε4 allele, N=177). AD biomarker data were also available for N=165 participants. Participants were collapsed again into two groups, an AD Biomarker Positive group (N=48) and an AD Biomarker Negative group (N=117). Available biomarker tests varied across participants, and included amyloid-beta PET scans and/or cerebrospinal fluid (CSF) amyloid-beta, tau, or phospho-tau measures. Positive or negative assignments were determined based on SUVR or DVR readings for the amyloid beta PET scans, with cut points at 1.35 and 1.19, respectively. Positive or negative group assignments for CSF results were based on the collecting lab's designation of "Consistent with AD" or "Inconsistent with AD". A summary of the APOE genotype and AD Biomarker group assignments is provided in **Table 4.2**.

Table 4.2: Available AD Biomarker and APOE Genotype Data					
Emphasis Group	**Diagnosis**	**N Positive AD Biomarker**	**N Negative AD Biomarker**	**N with APOE ε4 allele**	**N without APOE ε4 allele**
General Population 85+	Normal Cognition	9	21	53	13
General Population 65-85	Normal Cognition	12	89	57	29
General Population	Mild Cognitive Impairment	14	5	38	29
General Population	Dementia	13	2	29	27
Totals		48	117	177	98

Statistical Analyses and Validation of the NIH Toolbox Odor Identification Test. For the present study, we first calculated odor identification score summary statistics across diagnostic categories. These included the mean, standard deviation, range, N at floor, N at ceiling, skewness, and kurtosis of the distribution of odor identification scores for each group.

We then evaluated Odor Identification Scores using a multiple linear regression model with the equation:

$$Odor\ Score \sim \beta_o + Age\beta_1 + Sex\beta_2 + Diagnosis\beta_3$$

We fit this model across the three research diagnostic groups, age, and sex to assess relationships between olfactory performance and diagnosis. We also tested a second version of this model including interaction terms between each of the three predictors. The multiple regression models were fit for the entire participant population (N = 389). For each multiple regression model, age was centered at 77.8 years, the mean age of the entire participant pool. Thus, the intercept values

reported in the Results section represent the mean Odor Scores for NC Males at the mean age 77.8.

We then used a logistic regression model with the following equation, to evaluate whether Odor Scores, Age, and Sex can accurately predict whether a participant is in the aMCI versus NC group:

$$\ln\left(\frac{P}{1-P}\right) = \beta_0 + Odor\ Score\beta_1 + Sex\beta_2 + Age\beta_3$$

P refers to the computed probability of having aMCI given Odor score. For these analyses, we only included participants in the NC ages 65-85 group, and participants in the aMCI group.

We plotted a receiver operating characteristic (ROC) curve based on the fitted values of the logistic regression model. We calculated the Area Under the Curve (AUC), indicating how well Odor Scores, Age, and Sex can distinguish between aMCI and NC participants. The sensitivity, specificity, positive predictive value, and negative predictive value of this model are reported. The fitted probability of having aMCI for each Odor Score (0-9) is also reported.

Further, we used two three-way ANCOVAs to compare differences in odor scores across age, sex and the two special interest categories: AD biomarker presence (Positive versus Negative) and APOE ε4 allele carrier status (one or more ε4 allele versus no ε4 alleles). We then used a two-way ANCOVA to evaluate differences in odor scores based on sex and NC age group (ages 65-84 versus ages 85+).

4.4. Results

Table 4.3 displays the summary statistics for the Odor Identification Scores across each diagnostic cohort and NC age group.

Table 4.3: Summary of Odor Identification Scores by Cohort								
Emphasis Group	**Diagnosis**	**N**	**Mean +/- SD**	**Range**	**N at Floor**	**N at Ceiling**	**Skew-ness**	**Kurto-sis**
General Population 85+	Normal Cognition	96	6.14 +/- 1.70	2 – 9	0	2	-0.734	2.834
General Population 65-85	Normal Cognition	152	6.97 +/- 1.71	2 – 9	0	33	-0.750	2.942
General Population	Mild Cognitive Impairment	79	5.32 +/- 2.18	0 – 9	1	4	-0.163	2.140
General Population	Dementia	62	4.10 +/- 2.01	0 – 9	1	1	0.012	2.447
Total		389	5.97 +/- 2.12	0 – 9	2	40	-0.532	2.534

Differences in Odor Scores Across Age and Diagnostic Categories. To evaluate the decline of performance on the Odor Identification Test with age, and differences in Odor Scores across diagnostic categories, we fit a multiple linear regression model. The model was significant with adjusted $R^2 = 0.2985$ ($F_{4,384}$=40.85, $p < 2.2e\text{-}16$). The resulting model coefficients are displayed in **Table 4.4**. The intercept reflects the mean odor scores for NC Males at mean age 77.8 years.

Table 4.4: Multiple Linear Regression Model on the Relationships of Age, Sex, and Diagnosis with Odor Identification Scores				
Coefficient	**Estimate**	**Standard Error**	**t-value**	**p-value**
Intercept	6.367	0.163	38.951	< 2.0e-16
Age (per year)	-0.070	0.011	-6.143	2.03e-09
Sex = Female	0.530	0.186	-2.848	0.00464
Diagnosis = aMCI	-1.295	0.235	-5.519	6.28e-08
Diagnosis = AD	-2.675	0.258	-10.365	< 2.0e-16

This model suggests that odor identification scores decrease by 1 point for every 14.3-year increase in age (1/0.07 = 14.29). Females scored on average 0.530+/-0.186 points higher than males across diagnostic categories. Participants with aMCI scored on average 1.295+/-0.235 points lower than participants with NC, while participants with AD scored on average 2.675+/-0.258 points lower than participants with NC.

A second model was evaluated including interaction terms between Age and Sex, Age and Diagnosis, and Sex and Diagnosis. None of the interaction terms were significant (p-values ranged from 0.09 through 0.87), so they were not included in the final model. Interestingly, while the effect of Sex was significant in the main effects model, it was no longer significant in the model with main effects and interaction terms (p = 0.09). Differences in odor score across sex were evaluated within each diagnostic category using Welch two-sample t-tests. In the NC group, Odor Scores were significantly different between Males (mean=6.33) and Females (mean=6.84, $t_{182.64}$=2.2163 , p = 0.0279). However, Odor Scores were not significantly different between Males and Females for the aMCI or AD groups (p=0.09 for aMCI, p=0.21 for AD). **Figure 4.1** shows a scatterplot of Odor Identification Scores versus Age, with separate fitted regression lines (Odor Score ~ Age) with 95% confidence intervals for each diagnostic category. While Odor Scores decrease significantly with age, and the mean Odor Scores are significantly different across diagnostic categories, there is no significant interaction between age and diagnosis (i.e., slopes do not differ significantly across the three diagnostic categories). **Figure 4.2** shows distribution plots for Odor Scores, stratified by sex and diagnostic category.

Figure 4.1. Scatterplot displaying Odor Scores as a function of Age. Separate regression lines with 95% confidence intervals are fitted for NC (1, red), aMCI (2, green), and AD (3, blue) diagnostic categories. Odor Scores are integer values (0-9), but are jittered along the y-axis here for easier visualization.

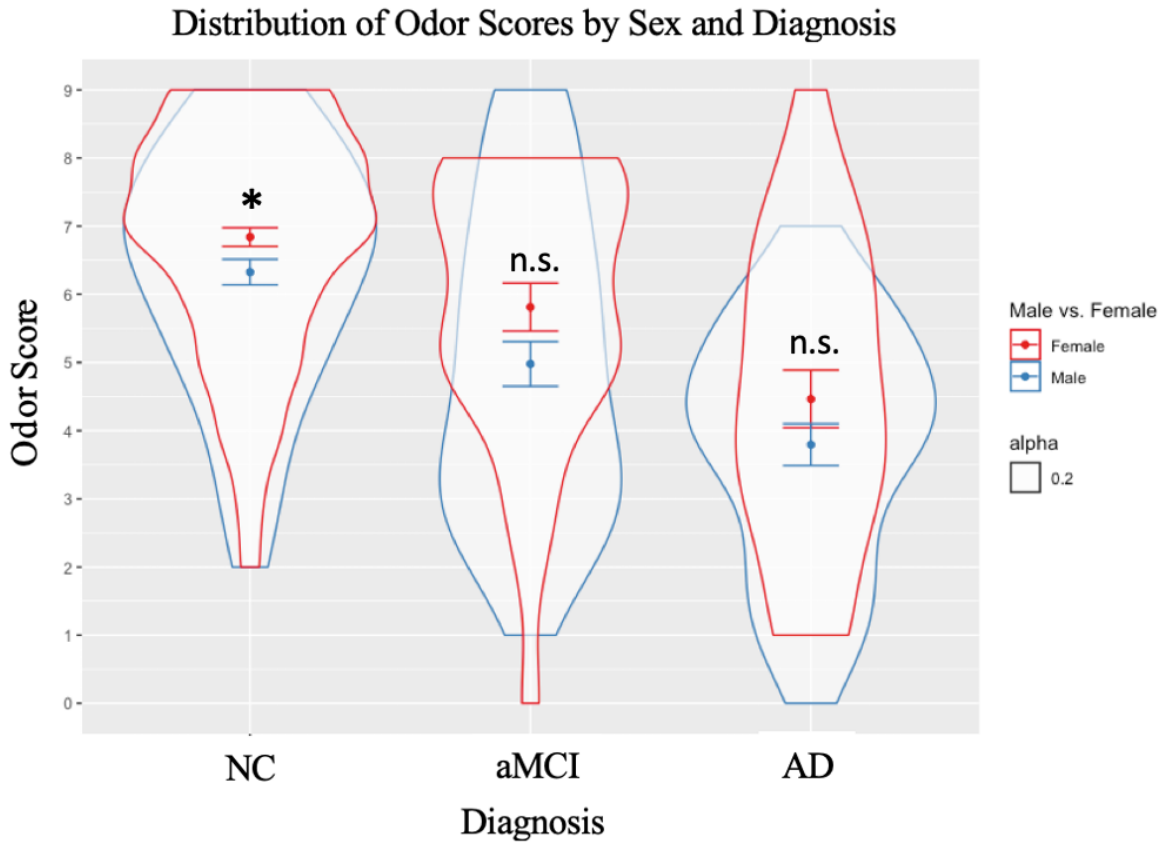

Figure 4.2. Violin plots displaying the distribution of Odor Scores across Sex and Diagnosis categories. Female = red, and Male = Blue.

Validation of the NIH Toolbox Odor Identification Test for Detecting aMCI. To determine whether the Odor Identification Test is useful for detecting aMCI, we computed a Receiver Operator Characteristic (ROC) curve based on a logistic regression model.

The model was fit with Male as the baseline group, and centered at the mean age of 77.8 years. The Akaike Information Criterion of the model was 248.3, with residual deviance of 240.30 (df= 227). The computed values of the coefficients and their interpretations are shown in **Table 4.5.**

Table 4.5: Logistic Regression Model on the Relationships of Age, Sex, and Odor Score with aMCI Diagnosis					
Term	**Coefficient**	**Standard Error**	**z-value**	**p-value**	**Interpretation**
Intercept	1.95977	0.53668	3.652	0.000261	A Male at mean age 77.8, with an Odor Score of 0 has 7.1 to 1 odds of having aMCI compared to NC. (Odds Ratio = 7.1)
Odor Score	-0.29231	0.08514	-3.422	0.000597	For every 1-point increase in Odor Score, there is a 25.3% decrease in relative risk for having aMCI.
Sex	-0.93531	0.32266	-2.899	0.003746	Females have a 60.8% decrease in relative risk for having aMCI compared to Males.
Age	0.10245	0.02815	3.639	0.000274	For every 1-year increase in age there is a 10.8% increase in relative risk for having aMCI

For a threshold of 0.50, the sensitivity and specificity of this model were found to be 49.4% and 88.8%, respectively. The Positive Predictive Value of this model was 69.6%, while the Negative Predictive Value was 77.1%. The calculated area under the curve (AUC) of the ROC plot was 0.78. The ROC plot is displayed in **Figure 4.3**. In **Figure 4.4**, the fitted probability values for having aMCI are plotted against the Odor Scores for each participant, color coded by sex. From this plot, we see that for females, an odor score of 3 or below has >50% chance of having aMCI, while for males, an odor score of 5 or below is has >50% chance of having aMCI.

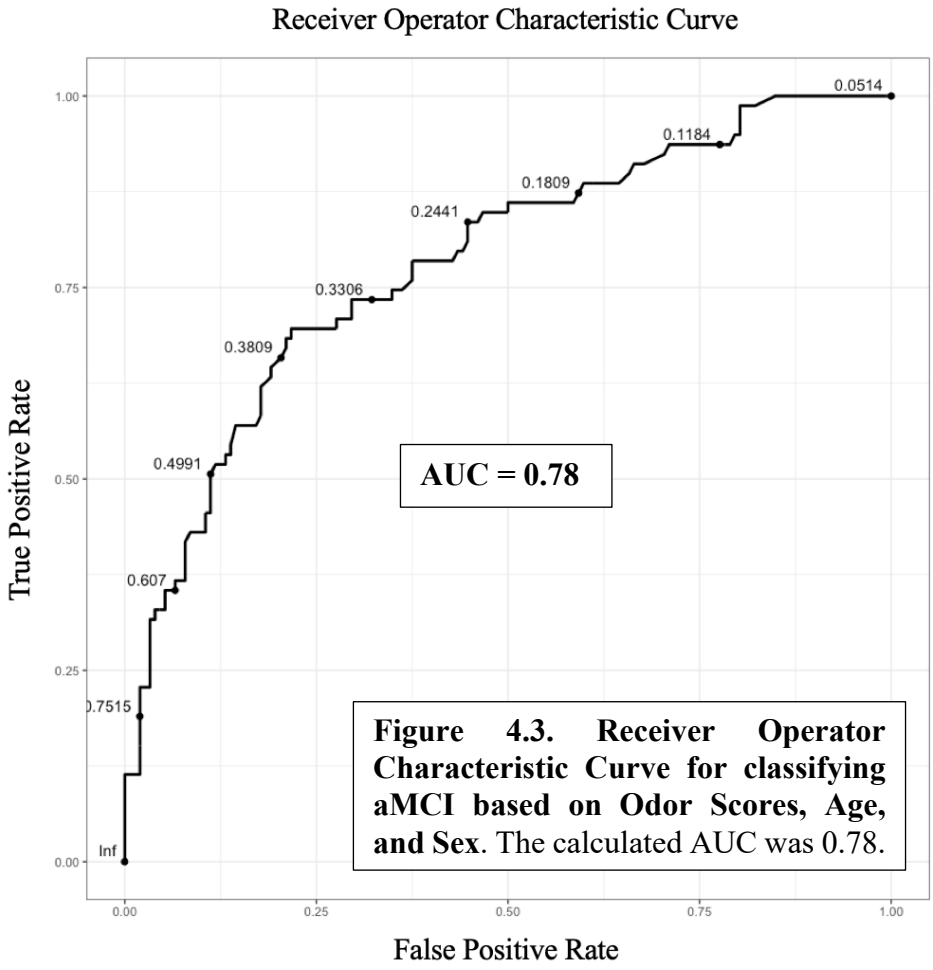

Figure 4.3. Receiver Operator Characteristic Curve for classifying aMCI based on Odor Scores, Age, and Sex. The calculated AUC was 0.78.

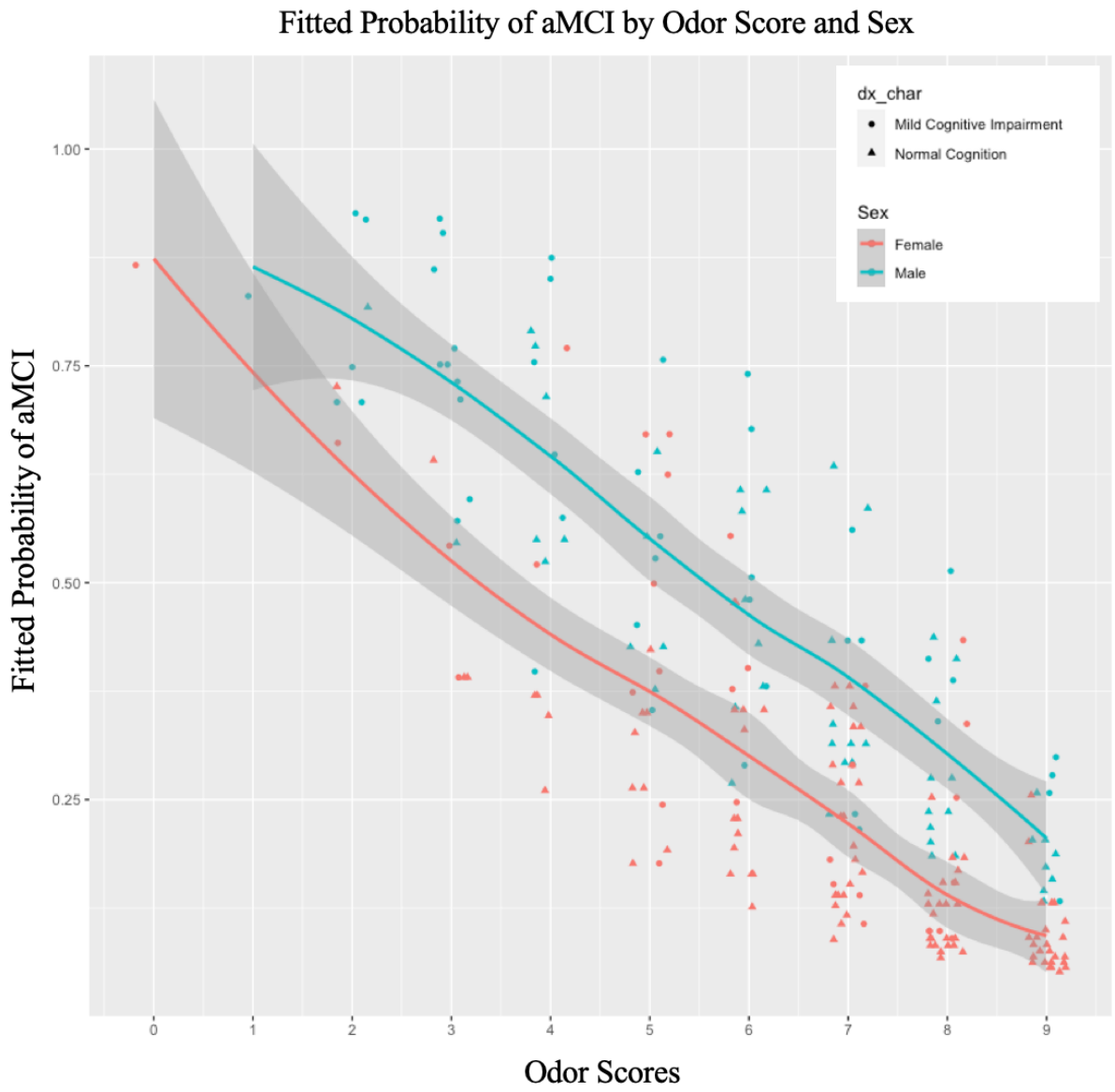

Figure 4.4 Scatter plot of participants' fitted probability of having aMCI from the logarithmic regression model described above, plotted against their scores on the Odor Identification Test. Loess smoother lines are fitted separately for females (Red) and males (Blue), with 95% confidence intervals. True diagnoses are indicated by the shape of the point with NC triangles and aMCI circles. Variability in fitted values about the y-axis reflects variability from the age of the participants. Odor Scores are integer values (0-9), but are jittered about the x-axis here for visualization.

Differences in Odor Scores based on AD Biomarker Presence. The mean +/- standard deviation odor scores for the biomarker positive group and biomarker negative group were 5.60 +/- 2.15, and 6.71 +/- 1.80, respectively. A three-way analysis of covariance (ANCOVA) was used to evaluate differences in odor scores across biomarker groups while controlling for age and sex. There was a significant main effect of biomarker status ($F_{1,161} = 7.941$, $p = 0.005$), where participants who had a positive AD biomarker test scored lower on the odor identification test than participants with a negative AD biomarker test. Main effects of Age and Sex were also significant (Age: $F_{1,161} = 7.923$, $p = 0.005$; Sex: $F_{1,161} = 5.745$, $p = 0.018$). The distribution of Odor Scores based on AD biomarker status is shown in **Figure 4.5.**

Differences in Odor Scores based on APOE ε4 Allele Status. The mean +/- standard deviation odor scores for the APOE ε4 allele carriers versus non-carriers were 5.72 +/- 2.21, and 5.99 +/- 2.18, respectively. A three-way ANCOVA was used to evaluate differences in odor scores between participants with at least one APOE ε4 allele and participants with no APOE ε4 alleles, while controlling for age and sex. The main effect of APOE ε4 allele status was not significant ($F_{1,271} = 2.852$, $p = 0.092$), indicating that odor scores did not significantly differ based on APOE ε4 allele status. The main effects of Age and Sex were significant (Age: $F_{1,271} = 16.926$, $p = 5.16e\text{-}05$; Sex: $F_{1,271} = 14.611$, $p = 1.64e\text{-}04$). The distribution of Odor Scores based on APOE ε4 Allele Status is shown in **Figure 4.6.**

Differences in Odor Scores between NC Participants Ages 65-84 and NC Participants over age 85. The mean and standard deviation odor scores for each age group are listed in **Table 3.** A two-

way ANCOVA was used to evaluate differences in odor scores between NC participants aged 65-84 and NC participants over age 85, while controlling for sex. In this model, the main effect of age group was significant ($F_{1,245} = 12.641$, $p = 0.000453$), indicating that participants in the 85+ years age group performed significantly worse on the odor identification test compared to participants in the 65-84 years age group. The main effect of sex was not significant in this model ($F_{1,245} = 3.601$, $p = 0.059$). The distribution of Odor Scores based on NC Age group are shown in **Figure 4.7.** We further broke down the mean and standard deviation odor scores across each decade: For participants aged 65-74 (N=103), the mean +/- standard deviation odor scores were 7.23 +/- 1.67; for participants aged 75-84 (N=49), the mean +/- standard deviation odor scores were 6.43 +/- 1.70; and for participants aged 85-91 (N=96), the mean +/- standard deviation odor scores were 6.13 +/- 1.70.

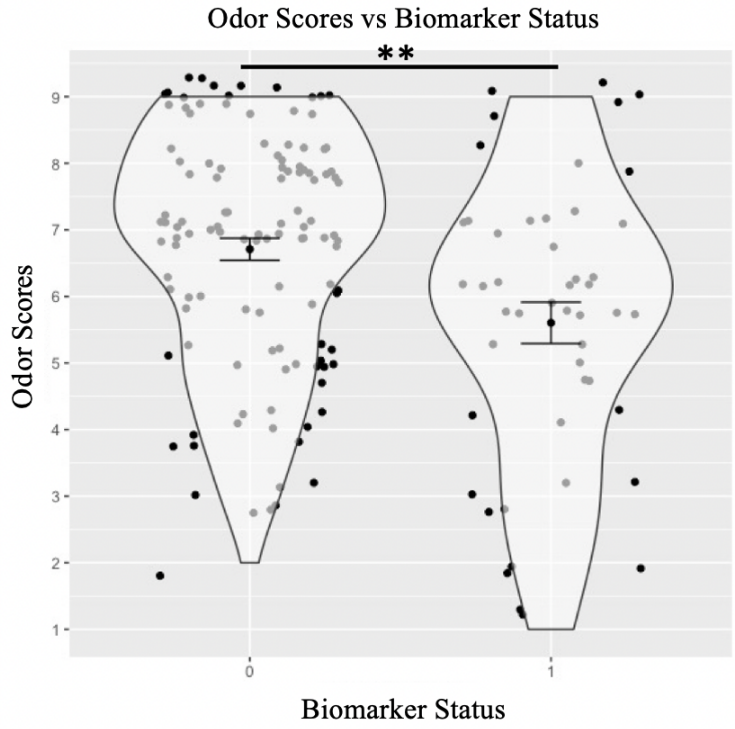

Figure 4.5 Violin plots illustrating the distribution of odor scores across AD biomarker groups. Group 0 was negative for AD biomarkers, and group 1 was positive for AD biomarkers. Note that odor scores are integer values (0-9), but are jittered here for visualization.

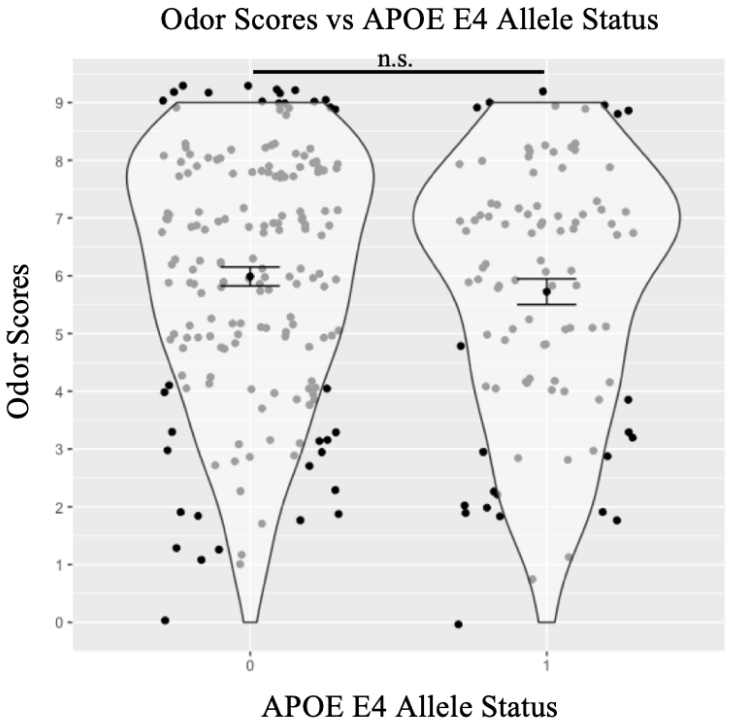

Figure 4.6 Violin plots illustrating the distribution of odor scores across APOE ε4 allele groups. Group 0 had no copies of the ε4 allele, and group 1 had at least one copy of the ε4 allele. Note that odor scores are integer values (0-9), but are jittered here for visualization.

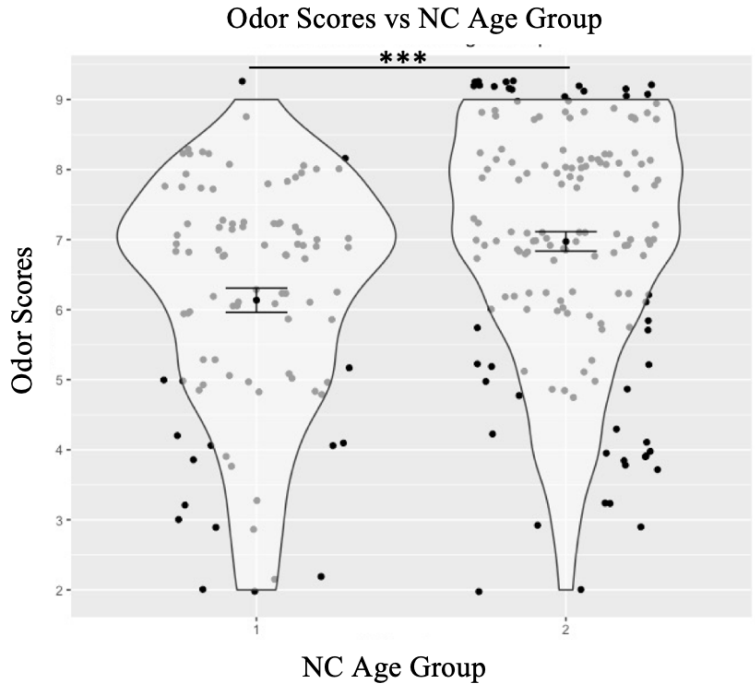

Figure 4.7 Violin plots illustrating the distribution of odor scores across NC participant age groups. Group 1 includes NC participants aged 85+, and group 2 includes NC participants aged 65-84. Note that odor scores are integer values (0-9), but are jittered here for visualization.

4.5. Discussion

In the present study, we found that scores on the NIH Toolbox Odor Identification Test were significantly lower for aMCI and AD compared to NC participants. Using multiple linear regression, we determined that scores on the Odor Identification Test decrease with age at a similar rate across all diagnostic categories, although the mean scores for each diagnostic category significantly differed. This may indicate that olfactory impairments begin earlier in life for those who go on to develop aMCI and AD, and is consistent with related findings that odor impairments may precede diagnosis of aMCI or AD by several years (Roberts et al., 2016; Schubert et al., 2008; Wilson et al., 2007). In addition, we found a weak effect of sex on odor identification scores, with females scoring better than males on average.

We further found that the Odor Identification Test is a useful tool for discriminating between participants with aMCI and participants with NC, while controlling for sex and age. An ROC curve fit with results from a logistic regression model had an AUC of 0.78, indicating good predictive value of the odor identification test. The sensitivity and specificity of the test at a threshold of 0.50 were 49.4% and 88.8%, respectively. While the odor identification test only correctly flagged about 50% of aMCI cases, it had a fairly low rate of false negatives. These findings are consistent with earlier studies of odor identification tests. The University of Pennsylvania Smell Identification Test (UPSIT) (Doty et al., 1984) was found to have a 74% sensitivity and 71% specificity for identifying aMCI in a recent study (Woodward et al., 2017). Additionally, in a longitudinal study, the San Diego Odor Identification Test (SDOIT) (Krantz et al., 2009) was found to have a sensitivity of 55.1% and specificity of 84.4% for predicting the 5-year incidence of cognitive impairment in a group of participants who had normal cognition at

baseline (Schubert et al., 2008). Thus, the NIH Toolbox Odor Identification Test appears to have similar or nominally better sensitivity and specificity for identifying aMCI compared to other evaluated odor identification tests.

The fitted logistic regression model also indicated an increase in relative risk of aMCI of about 10.8% per year increase in age, suggesting that the relative risk of having aMCI doubles roughly every 6.75 years within this age group. Additionally, the model indicated that females have a 60.8% decrease in relative risk for having aMCI compared to males, given a particular age and score on the Odor Identification Test. To illustrate this effect, we plotted the fitted probability values for having aMCI for males and females against their scores on the Odor Identification Test, and fit loess smoother curves with 95% confidence intervals. We see from the plot that for females, scores of 3 and below on the Odor Identification test indicate greater than 50% probability of having aMCI, while for males, scores of 5 and below indicate greater than 50% probability of having aMCI. Thus, clinicians and researchers using the Odor Identification Test to evaluate the possible presence of aMCI should consider age and sex when determining diagnosis.

For a subset of participants, data from various AD biomarker tests and APOE genotype data were available. We determined whether Odor Identification Scores differ significantly depending on the presence of AD biomarkers or the presence of at least one APOE ε4 allele. We determined that odor scores were significantly lower for participants who had a positive AD biomarker test compared to those who had negative AD biomarker tests. This is consistent with previous findings that the severity of AD biomarkers, particularly tau pathology, correlates with performance on odor identification tests (Klein et al., 2021; Lafaille-Magnan et al., 2017;

Vassilaki et al., 2017). We determined that odor identification scores did not significantly differ between participants who had no APOE ε4 alleles, and participants who had at least one APOE ε4 allele. The APOE ε4 allele is associated with an increased lifetime risk of developing aMCI and AD (Belloy et al., 2019), but when comparing APOE ε4 allele status and olfactory impairment, there have been mixed results. One study found that there was a significant interaction between family history of AD and APOE ε4 allele status on an odor identification test, but no significant main effect of APOE ε4 allele status (Handley et al., 2006). However, in a 10-year longitudinal study, APOE ε4 homozygotes were found to have earlier onset olfactory impairment and more rapid decline in olfaction and cognition compared to controls (Josefsson et al., 2017). A third study found that APOE ε4 homozygotes performed significantly worse on odor identification and odor memory tasks compared to APOE ε3/ε4 heterozygotes and noncarriers (Oleson & Murphy, 2015). A large population-based study (N=1236) found that APOE ε4 allele carriers were impaired in odor identification compared to non-carriers, but that this effect was independent from 5-year conversion from NC to AD (Olofsson et al., 2010). This literature suggests olfactory impairment risk with one APOE ε4 allele may be more easily detected with larger sample sizes, and that APOE ε4 homozygotes have a substantially increased risk for olfactory impairments compared to APOE ε3/ε4 heterozygotes and noncarriers. However, in our sample of N=275 participants with available genotype data, only 19 were identified as APOE ε4 homozygotes. This is likely too small a sample size to accurately test for effects of APOE ε4 carrier status on olfactory performance.

Lastly, since the NIH Toolbox Odor Identification Test was originally only validated for NC populations up to age 85 (Dalton et al., 2013), we tested performance on the test for a group

of N=96 NC participants ages 85 through 91. We found that performance on the Odor Identification Test for this age group was significantly lower compared to performance of NC participants aged 65-84. This is consistent with previous literature suggesting a steady decline of olfactory ability with age, beginning with a slow decline in the 40s-50s and a more rapid decline after age 60 (Albers et al., 2015; Dalton et al., 2013; Doty & Kamath, 2014).

While we have determined that the NIH Toolbox Odor Identification Test is useful for classifying aMCI versus NC, it is not sensitive or specific enough to rely on for an individual diagnosis. Olfactory impairments are strongly associated with aMCI and AD, but are not specific to these disorders and have been associated with healthy aging (Dalton et al., 2013), Parkinson's disease (Fullard et al., 2017; M. Witt et al., 2009), Huntington's disease (Patino et al., 2021), multiple sclerosis (Carotenuto et al., 2019; L.-M. Li et al., 2016), traumatic brain injuries (Howell et al., 2018), and strokes (Wehling et al., 2015). We have identified a positive predictive value for the NIH Toolbox Odor Identification Test of 69.6%, while the Negative Predictive Value was 77.1%. While the test cannot provide a definitive diagnosis, we suggest that this simple and cost-effective 9-item test may be useful if included in annual physical exams provided to senior patients. If a low score is obtained, then the patient may be referred for in-depth neuropsychological evaluation by a specialist to determine whether other symptoms of mild cognitive impairments are present.

An additional consideration is the cultural relevancy of odor identification tests. These tests require some degree of familiarity and past experiences with the presented odors. Many odors are language- or culture-specific, and native speakers have been shown to perform significantly better on tests developed within their culture compared to non-native participants

(Cavazzana et al., 2017; Cho et al., 2009; Shu et al., 2007). With this in mind, we caution that using the NIH Toolbox Odor Identification Test to evaluate risk of aMCI outside of the United States population may not be as accurate.

Further studies are needed to determine whether the NIH Toolbox Odor Identification Test has longitudinal predictive power for identifying which NC participants will convert to aMCI, and which aMCI participants will convert to AD. Additionally, investigations into the relationships between odor identification scores and amyloid and tau burden will help determine the usefulness of these tests for identifying participants with AD-specific pathologies. In summary, we have provided evidence for the association between scores on the NIH Toolbox Odor Identification Test and diagnosis across NC, aMCI, and AD participants, and we have demonstrated that this test has good predictive power for classifying NC from aMCI participants.

4.6. Acknowledgements & Author Contributions

This work was supported by NIH grants NIDCD R01DC015426-04S1 and ADC P30: NIA P30AG13854 (to T.K.).

Shiloh L. Echevarria-Cooper, Thorsten Kahnt, and Sandra Weintraub designed the research approach. Shiloh L. Echevarria-Cooper performed the statistical analysis. Sandra Weintraub, Emily H. Ho, and Richard Gershon provided guidance and commentary on the research approach and provided access to the ARMADA dataset. Shiloh L. Echevarria-Cooper wrote the first draft of the manuscript. Thorsten Kahnt contributed to writing and editing the manuscript.

Chapter 5: Concluding Remarks and Future Directions

In the present thesis work, we have provided a detailed characterization of the human olfactory and OFC anatomical brain networks, and evaluated relationships between olfactory performance and age across NC, aMCI and AD cohorts. Here, we consider the broader significance of our findings, and propose new lines of future research to further our understanding of the human olfactory-OFC brain network's anatomy and function in health and disease.

Our results in Chapter 2 provide novel evidence for specific projections of the human lateral olfactory tracts into primary olfactory cortex, and provide evidence for a relationship between olfactory tract microstructural integrity and olfactory perceptual performance. However, the specific cellular-level topological organization and functional dissociation of the parallel olfactory tract pathways have yet to be determined. Future work might start by identifying whether specific parts of the olfactory bulb project to specific cortical ROIs by using high resolution structural and diffusion MRI methods. Sub-millimeter resolution structural scans are becoming more common, and can be achieved with good signal-to-noise ratios when using 7T and 10T scanners, although scanning time required will be quite high. In *in vivo* studies, participants with a range of olfactory perceptual abilities can be recruited and evaluated for differences in olfactory tract microstructural integrity. We may then be able to determine whether microstructural measures in the separate olfactory tract striae relate to different olfactory functions. In addition, potential *post mortem* experiments could combine high-resolution structural and diffusion MRI measures with histological methods and newly developing *ex vivo* axon tracing methods (Heilingoetter & Jensen, 2016; Yendiki et al., 2022) to investigate the

microstructural and cellular-level anatomy of the human olfactory tracts and primary olfactory cortex in greater detail. Our probabilistic lateral olfactory tract atlas will help in localizing the lateral olfactory tracts and striae in future structural and diffusion MRI investigations of these pathways.

Our work in Chapter 3 provides a detailed characterization of the human OFC anatomical networks, and further identifies OFC subregions that have distinct connectivity profiles through a k-means clustering approach. With these results, we are able to identify how the OFC is situated within several brain-wide anatomical networks, and develop hypotheses regarding OFC function and contribution to these networks' functioning. We found that the OFC shares strong connectivity with the hub regions in the ventral attention network, the default mode network, and the central executive network, suggesting that the OFC may provide some influence in the activity of these networks. One hypothesis is that the OFC's "cognitive map" of motivationally-salient stimuli and their contextual relevancy may serve as a sort of reference for the ventral attention network to help determine if and when an incoming stimulus should be allowed to interrupt or recruit the functions of the central executive network. Further research, perhaps using a task-based fMRI approach, will be necessary to test these hypotheses. Potential experiments may characterize task-based functional connectivity between regions of the ventral attention network, central executive network, and the OFC during a decision-making task with changing reward contingencies. Differences in OFC functional connectivity with the ventral attention and central executive networks could be characterized in response to changing stimuli that are task-relevant and that require a change in behavior to complete the task, versus salient distractor stimuli that should be ignored in order to successfully complete the task. A transcranial

magnetic stimulation experiment could also determine whether a participant would perform more poorly on this type of task following temporary deactivation of the OFC. Ultimately, our characterization of the human OFC's anatomical networks provides a myriad of jumping-off points for generating testable mechanistic hypotheses on the function and behavioral importance of the human OFC.

Our findings in Chapter 4 add to a growing body of literature documenting olfactory perceptual impairments in the aMCI to AD disease process. While evidence is accumulating that olfaction is impaired early on in the disease process, and that olfactory perceptual tests are able to detect early stages of cognitive decline and predict future conversion to AD, a mechanistic understanding of the olfactory neuropathology is still lacking. Future studies may use optimized MS-EPI diffusion MRI and structural MRI sequences, such as the one developed for this thesis work, to evaluate the microstructural integrity of the lateral olfactory tracts, olfactory bulbs, and primary olfactory cortical regions in elderly participants across NC, aMCI, and AD. Diffusion microstructural measures such as FA and MD may be used to evaluate differences across groups and identify signs of neurodegeneration in the olfactory system. Pairing these techniques with a longitudinal study design would allow us to build temporal hypotheses regarding disease progression, and determine whether degeneration follows along previously identified white matter pathways and across synapses.

The current findings provide a new level of insight into the anatomical network structure of the human olfactory system and OFC. Additionally, we found that olfactory functioning is impaired in aMCI and AD, suggesting that olfactory brain regions are likely adversely affected in these diseases. New lines of research will be necessary to further elucidate the anatomical and

functional characteristics of specific regions and pathways within the human olfactory-OFC brain networks, and their susceptibility to degeneration and dysregulation in the aMCI to AD disease process. The findings presented in this thesis provide a valuable reference for generating anatomically-informed hypotheses of human olfactory-OFC function in health and disease.

References

Albers, M. W., Albers, A., Keim, A. C., Cunin, C., Hyman, B. T., Gomez-Isla, T., Blacker, D., Das, S., & Locascio, J. J. (2020). Selective loss of episodic memory of odor percepts is associated with progression to amnestic MCI or Alzheimer's disease in cognitively healthy seniors. *Alzheimer's & Dementia*, *16*(S5), e046649. https://doi.org/10.1002/alz.046649

Albers, M. W., Gilmore, G. C., Kaye, J., Murphy, C., Wingfield, A., Bennett, D. A., Boxer, A. L., Buchman, A. S., Cruickshanks, K. J., Devanand, D. P., Duffy, C. J., Gall, C. M., Gates, G. A., Granholm, A.-C., Hensch, T., Holtzer, R., Hyman, B. T., Lin, F. R., McKee, A. C., … Zhang, L. I. (2015). At the interface of sensory and motor dysfunctions and Alzheimer's Disease. *Alzheimer's & Dementia : The Journal of the Alzheimer's Association*, *11*(1), 70–98. https://doi.org/10.1016/j.jalz.2014.04.514

Alexander, A. L., Lee, J. E., Lazar, M., & Field, A. S. (2007). Diffusion tensor imaging of the brain. *Neurotherapeutics: The Journal of the American Society for Experimental NeuroTherapeutics*, *4*(3), 316–329. https://doi.org/10.1016/j.nurt.2007.05.011

Allen, B., Spiegel, D. P., Thompson, B., Pestilli, F., & Rokers, B. (2015). Altered white matter in early visual pathways of humans with amblyopia. *Vision Research*, *114*, 48–55. https://doi.org/10.1016/j.visres.2014.12.021

Allison, A. C. (1954). The secondary olfactory areas in the human brain. *Journal of Anatomy*, *88*(Pt 4), 481-488.2.

Attems, J., Lintner, F., & Jellinger, K. A. (2005). Olfactory involvement in aging and Alzheimer's disease: An autopsy study. *Journal of Alzheimer's Disease: JAD*, *7*(2), 149–157; discussion 173-180. https://doi.org/10.3233/jad-2005-7208

Bacon, A. W., Bondi, M. W., Salmon, D. P., & Murphy, C. (1998). Very Early Changes in Olfactory Functioning Due to Alzheimer's Disease and the Role of Apolipoprotein E in Olfactiona. *Annals of the New York Academy of Sciences*, *855*(1), 723–731. https://doi.org/10.1111/j.1749-6632.1998.tb10651.x

Bahar-Fuchs, A., Chételat, G., Villemagne, V. L., Moss, S., Pike, K., Masters, C. L., Rowe, C., & Savage, G. (2010). Olfactory Deficits and Amyloid-β Burden in Alzheimer's Disease, Mild Cognitive Impairment, and Healthy Aging: A PiB PET Study. *Journal of Alzheimer's Disease*, *22*(4), 1081–1087. https://doi.org/10.3233/JAD-2010-100696

Bao, X., Gjorgieva, E., Shanahan, L. K., Howard, J. D., Kahnt, T., & Gottfried, J. A. (2019). Grid-like Neural Representations Support Olfactory Navigation of a Two-Dimensional Odor Space. *Neuron*, *102*(5), 1066-1075.e5. https://doi.org/10.1016/j.neuron.2019.03.034

Bao, X., Raguet, L. L., Cole, S. M., Howard, J. D., & Gottfried, J. (2016). The role of piriform associative connections in odor categorization. *ELife*, *5*, e13732. https://doi.org/10.7554/eLife.13732

Basser, P. J., Mattiello, J., & LeBihan, D. (1994). MR diffusion tensor spectroscopy and imaging. *Biophysical Journal*, *66*(1), 259–267. https://doi.org/10.1016/S0006-3495(94)80775-1

Basser, P. J., & Pierpaoli, C. (1996). Microstructural and Physiological Features of Tissues Elucidated by Quantitative-Diffusion-Tensor MRI. *Journal of Magnetic Resonance, Series B*, *111*(3), 209–219. https://doi.org/10.1006/jmrb.1996.0086

Beaulieu, C., Does, M. D., Snyder, R. E., & Allen, P. S. (1996). Changes in water diffusion due to Wallerian degeneration in peripheral nerve. *Magnetic Resonance in Medicine*, *36*(4), 627–631. https://doi.org/10.1002/mrm.1910360419

Belloy, M. E., Napolioni, V., & Greicius, M. D. (2019). A Quarter Century of APOE and Alzheimer's Disease: Progress to Date and the Path Forward. *Neuron*, *101*(5), 820–838. https://doi.org/10.1016/j.neuron.2019.01.056

Bengtsson, S. L., Nagy, Z., Skare, S., Forsman, L., Forssberg, H., & Ullén, F. (2005). Extensive piano practicing has regionally specific effects on white matter development. *Nature Neuroscience*, *8*(9), 1148–1150. https://doi.org/10.1038/nn1516

Berlin, H. A., Rolls, E. T., & Kischka, U. (2004). Impulsivity, time perception, emotion and reinforcement sensitivity in patients with orbitofrontal cortex lesions. *Brain*, *127*(5), 1108–1126. https://doi.org/10.1093/brain/awh135

Blumenfeld-Katzir, T., Pasternak, O., Dagan, M., & Assaf, Y. (2011). Diffusion MRI of Structural Brain Plasticity Induced by a Learning and Memory Task. *PLOS ONE*, *6*(6), e20678. https://doi.org/10.1371/journal.pone.0020678

Boniface M. Kavoi & Hassanali Jameela. (2011). Comparative Morphometry of the Olfactory Bulb, Tractand Stria in the Human, Dog and Goat. *Int. J. Morphol.*, *29*(3), 939–946.

Bowman, N. E., Kording, K. P., & Gottfried, J. A. (2012). Temporal Integration of Olfactory Perceptual Evidence in Human Orbitofrontal Cortex. *Neuron*, *75*(5), 916–927. https://doi.org/10.1016/j.neuron.2012.06.035

Braak, H., & Braak, E. (1991). Neuropathological stageing of Alzheimer-related changes. *Acta Neuropathologica*, *82*(4), 239–259. https://doi.org/10.1007/BF00308809

Braak, H., & Braak, E. (1995). Staging of alzheimer's disease-related neurofibrillary changes. *Neurobiology of Aging*, *16*(3), 271–278. https://doi.org/10.1016/0197-4580(95)00021-6

Brown, T. E. (2009). ADD/ADHD and impaired executive function in clinical practice. *Current Attention Disorders Reports*, *1*(1), 37–41. https://doi.org/10.1007/s12618-009-0006-3

Buchanan, S. M., Parker, T. D., Lane, C. A., Keshavan, A., Keuss, S. E., Lu, K., James, S.-N., Murray-Smith, H., Wong, A., Nicholas, J., Cash, D. M., Malone, I. B., Coath, W., Thomas, D. L., Sudre, C., Fox, N. C., Richards, M., & Schott, J. M. (2020). Olfactory testing does not predict β-amyloid, MRI measures of neurodegeneration or vascular pathology in the British 1946 birth cohort. *Journal of Neurology*, *267*(11), 3329–3336. https://doi.org/10.1007/s00415-020-10004-4

Calamante, F., Tournier, J.-D., Jackson, G. D., & Connelly, A. (2010). Track-density imaging (TDI): Super-resolution white matter imaging using whole-brain track-density mapping. *NeuroImage*, *53*(4), 1233–1243. https://doi.org/10.1016/j.neuroimage.2010.07.024

Carmichael, S. T., Clugnet, M. C., & Price, J. L. (1994). Central olfactory connections in the macaque monkey. *The Journal of Comparative Neurology*, *346*(3), 403–434. https://doi.org/10.1002/cne.903460306

Carmichael, S. T., & Price, J. L. (1994). Architectonic subdivision of the orbital and medial prefrontal cortex in the macaque monkey. *Journal of Comparative Neurology*, *346*(3), 366–402. https://doi.org/10.1002/cne.903460305

Carmichael, S. T., & Price, J. L. (1995a). Limbic connections of the orbital and medial prefrontal cortex in macaque monkeys. *The Journal of Comparative Neurology*, *363*(4), 615–641. https://doi.org/10.1002/cne.903630408

Carmichael, S. T., & Price, J. L. (1995b). Sensory and premotor connections of the orbital and medial prefrontal cortex of macaque monkeys. *The Journal of Comparative Neurology*, *363*(4), 642–664. https://doi.org/10.1002/cne.903630409

Carmichael, S. T., & Price, J. L. (1996). Connectional networks within the orbital and medial prefrontal cortex of macaque monkeys. *The Journal of Comparative Neurology*, *371*(2), 179–207. https://doi.org/10.1002/(SICI)1096-9861(19960722)371:2<179::AID-CNE1>3.0.CO;2-#

Carotenuto, A., Costabile, T., Moccia, M., Falco, F., Scala, M. R., Russo, C. V., Saccà, F., De Rosa, A., Lanzillo, R., & Brescia Morra, V. (2019). Olfactory function and cognition in relapsing–remitting and secondary-progressive multiple sclerosis. *Multiple Sclerosis and Related Disorders*, *27*, 1–6. https://doi.org/10.1016/j.msard.2018.09.024

Catani, M., Dell'Acqua, F., & Thiebaut de Schotten, M. (2013). A revised limbic system model for memory, emotion and behaviour. *Neuroscience & Biobehavioral Reviews*, *37*(8), 1724–1737. https://doi.org/10.1016/j.neubiorev.2013.07.001

Catani, M., & Thiebaut de Schotten, M. (2008). A diffusion tensor imaging tractography atlas for virtual in vivo dissections. *Cortex*, *44*(8), 1105–1132. https://doi.org/10.1016/j.cortex.2008.05.004

Cavada, C., Compañy, T., Tejedor, J., Cruz-Rizzolo, R. J., & Reinoso-Suárez, F. (2000). The Anatomical Connections of the Macaque Monkey Orbitofrontal Cortex. A Review. *Cerebral Cortex*, *10*(3), 220–242. https://doi.org/10.1093/cercor/10.3.220

Cavazzana, A., Wesarg, C., Schriever, V. A., Hummel, T., Lundström, J. N., & Parma, V. (2017). A Cross-Cultural Adaptation of the Sniffin' Sticks Olfactory Identification Test

for US children. *Chemical Senses*, *42*(2), 133–140. https://doi.org/10.1093/chemse/bjw113

Cerliani, L., D'Arceuil, H., & Thiebaut de Schotten, M. (2017). Connectivity-based parcellation of the macaque frontal cortex, and its relation with the cytoarchitectonic distribution described in current atlases. *Brain Structure and Function*, *222*(3), 1331–1349. Scopus. https://doi.org/10.1007/s00429-016-1280-3

Chiavaras, M. M., LeGoualher, G., Evans, A., & Petrides, M. (2001). Three-Dimensional Probabilistic Atlas of the Human Orbitofrontal Sulci in Standardized Stereotaxic Space. *NeuroImage*, *13*(3), 479–496. https://doi.org/10.1006/nimg.2000.0641

Cho, J. H., Jeong, Y. S., Lee, Y. J., Hong, S.-C., Yoon, J.-H., & Kim, J. K. (2009). The Korean version of the Sniffin' stick (KVSS) test and its validity in comparison with the cross-cultural smell identification test (CC-SIT). *Auris Nasus Larynx*, *36*(3), 280–286. https://doi.org/10.1016/j.anl.2008.07.005

Corder, E. H., Saunders, A. M., Strittmatter, W. J., Schmechel, D. E., Gaskell, P. C., Small, G. W., Roses, A. D., Haines, J. L., & Pericak-Vance, M. A. (1993). Gene dose of apolipoprotein E type 4 allele and the risk of Alzheimer's disease in late onset families. *Science (New York, N.Y.)*, *261*(5123), 921–923. https://doi.org/10.1126/science.8346443

Crosby, E. C., & Humphrey, T. (1941). Studies of the vertebrate telencephalon. II. The nuclear pattern of the anterior olfactory nucleus, tuberculum olfactorium and the amygdaloid complex in adult man. *Journal of Comparative Neurology*, *74*, 309–352.

Croxson, P. L., Johansen-Berg, H., Behrens, T. E. J., Robson, M. D., Pinsk, M. A., Gross, C. G., Richter, W., Richter, M. C., Kastner, S., & Rushworth, M. F. S. (2005). Quantitative

Investigation of Connections of the Prefrontal Cortex in the Human and Macaque using Probabilistic Diffusion Tractography. *Journal of Neuroscience*, *25*(39), 8854–8866. https://doi.org/10.1523/JNEUROSCI.1311-05.2005

Dalton, P., Doty, R. L., Murphy, C., Frank, R., Hoffman, H. J., Maute, C., Kallen, M. A., & Slotkin, J. (2013). Olfactory assessment using the NIH Toolbox. *Neurology*, *80*(11 Suppl 3), S32–S36. https://doi.org/10.1212/WNL.0b013e3182872eb4

Devanand, D. P., Lee, S., Manly, J., Andrews, H., Schupf, N., Doty, R. L., Stern, Y., Zahodne, L. B., Louis, E. D., & Mayeux, R. (2015). Olfactory deficits predict cognitive decline and Alzheimer dementia in an urban community. *Neurology*, *84*(2), 182–189. https://doi.org/10.1212/WNL.0000000000001132

Dietrich, S., Hertrich, I., Kumar, V., & Ackermann, H. (2015). Experience-Related Structural Changes of Degenerated Occipital White Matter in Late-Blind Humans – A Diffusion Tensor Imaging Study. *PLOS ONE*, *10*(4), e0122863. https://doi.org/10.1371/journal.pone.0122863

Djordjevic, J., Jones-Gotman, M., De Sousa, K., & Chertkow, H. (2008). Olfaction in patients with mild cognitive impairment and Alzheimer's disease. *Neurobiology of Aging*, *29*(5), 693–706. https://doi.org/10.1016/j.neurobiolaging.2006.11.014

Doody, R. S., Ferris, S. H., Salloway, S., Meuser, T. M., Murthy, A. K., Li, C., & Goldman, R. (2011). Identifying amnestic mild cognitive impairment in primary care: A feasibility study. *Clinical Drug Investigation*, *31*(7), 483–491. https://doi.org/10.2165/11588810-000000000-00000

Doty, R. L., & Kamath, V. (2014). The influences of age on olfaction: A review. *Frontiers in Psychology*, *5*, 20. https://doi.org/10.3389/fpsyg.2014.00020

Doty, R. L., Reyes, P. F., & Gregor, T. (1987). Presence of both odor identification and detection deficits in Alzheimer's disease. *Brain Research Bulletin*, *18*(5), 597–600. https://doi.org/10.1016/0361-9230(87)90129-8

Doty, R. L., Shaman, P., Kimmelman, C. P., & Dann, M. S. (1984). University of Pennsylvania Smell Identification Test: A rapid quantitative olfactory function test for the clinic. *The Laryngoscope*, *94*(2 Pt 1), 176–178. https://doi.org/10.1288/00005537-198402000-00004

Dronkers, N. F., Plaisant, O., Iba-Zizen, M. T., & Cabanis, E. A. (2007). Paul Broca's historic cases: High resolution MR imaging of the brains of Leborgne and Lelong. *Brain: A Journal of Neurology*, *130*(Pt 5), 1432–1441. https://doi.org/10.1093/brain/awm042

Duan, Y., Norcia, A. M., Yeatman, J. D., & Mezer, A. (2015). The Structural Properties of Major White Matter Tracts in Strabismic Amblyopia. *Investigative Ophthalmology & Visual Science*, *56*(9), 5152–5160. https://doi.org/10.1167/iovs.15-17097

Ebeling, U., & Cramon, D. v. (1992). Topography of the uncinate fascicle and adjacent temporal fiber tracts. *Acta Neurochirurgica*, *115*(3), 143–148. https://doi.org/10.1007/BF01406373

Echevarria-Cooper, S. L., Zhou, G., Zelano, C., Pestilli, F., Parrish, T. B., & Kahnt, T. (2022). Mapping the Microstructure and Striae of the Human Olfactory Tract with Diffusion MRI. *Journal of Neuroscience*, *42*(1), 58–68. https://doi.org/10.1523/JNEUROSCI.1552-21.2021

Fernández-Jaén, A., López-Martín, S., Albert, J., Fernández-Mayoralas, D. M., Fernández-Perrone, A. L., Tapia, D. Q., & Calleja-Pérez, B. (2014). Cortical thinning of temporal

pole and orbitofrontal cortex in medication-naïve children and adolescents with ADHD. *Psychiatry Research: Neuroimaging*, *224*(1), 8–13. https://doi.org/10.1016/j.pscychresns.2014.07.004

Ferry, A. T., Ongür, D., An, X., & Price, J. L. (2000). Prefrontal cortical projections to the striatum in macaque monkeys: Evidence for an organization related to prefrontal networks. *The Journal of Comparative Neurology*, *425*(3), 447–470. https://doi.org/10.1002/1096-9861(20000925)425:3<447::aid-cne9>3.0.co;2-v

Fjaeldstad, A., Fernandes, H. M., Van Hartevelt, T. J., Gleesborg, C., Møller, A., Ovesen, T., & Kringelbach, M. L. (2017). Brain fingerprints of olfaction: A novel structural method for assessing olfactory cortical networks in health and disease. *Scientific Reports*, *7*(1), Article 1. https://doi.org/10.1038/srep42534

Frank, L. R. (2002). Characterization of anisotropy in high angular resolution diffusion-weighted MRI. *Magnetic Resonance in Medicine*, *47*(6), 1083–1099. https://doi.org/10.1002/mrm.10156

Fullard, M. E., Morley, J. F., & Duda, J. E. (2017). Olfactory Dysfunction as an Early Biomarker in Parkinson's Disease. *Neuroscience Bulletin*, *33*(5), 515–525. https://doi.org/10.1007/s12264-017-0170-x

Genc, E., Bergmann, J., Tong, F., Blake, R., Singer, W., & Kohler, A. (2011). Callosal connections of primary visual cortex predict the spatial spreading of binocular rivalry across the visual hemifields. *Frontiers in Human Neuroscience*, *5*. https://www.frontiersin.org/articles/10.3389/fnhum.2011.00161

Gershon, R. C., Wagster, M. V., Hendrie, H. C., Fox, N. A., Cook, K. F., & Nowinski, C. J. (2013). NIH toolbox for assessment of neurological and behavioral function. *Neurology*, *80*(11 Suppl 3), S2-6. https://doi.org/10.1212/WNL.0b013e3182872e5f

Giguere, M., & Goldman-Rakic, P. S. (1988). Mediodorsal nucleus: Areal, laminar, and tangential distribution of afferents and efferents in the frontal lobe of rhesus monkeys. *The Journal of Comparative Neurology*, *277*(2), 195–213. https://doi.org/10.1002/cne.902770204

Gilbert, P. E., & Murphy, C. (2004). The effect of the ApoE epsilon4 allele on recognition memory for olfactory and visual stimuli in patients with pathologically confirmed Alzheimer's disease, probable Alzheimer's disease, and healthy elderly controls. *Journal of Clinical and Experimental Neuropsychology*, *26*(6), 779–794. https://doi.org/10.1080/13803390490509439

Gottfried, J. A. (2010). Central mechanisms of odour object perception. *Nature Reviews. Neuroscience*, *11*(9), 628–641. https://doi.org/10.1038/nrn2883

Gottfried, J. A., & Zald, D. H. (2005). On the scent of human olfactory orbitofrontal cortex: Meta-analysis and comparison to non-human primates. *Brain Research. Brain Research Reviews*, *50*(2), 287–304. https://doi.org/10.1016/j.brainresrev.2005.08.004

Haber, S. N., & Knutson, B. (2010). The reward circuit: Linking primate anatomy and human imaging. *Neuropsychopharmacology: Official Publication of the American College of Neuropsychopharmacology*, *35*(1), 4–26. https://doi.org/10.1038/npp.2009.129

Haber, S. N., Kunishio, K., Mizobuchi, M., & Lynd-Balta, E. (1995). The orbital and medial prefrontal circuit through the primate basal ganglia. *The Journal of Neuroscience: The Official Journal of the Society for Neuroscience*, *15*(7 Pt 1), 4851–4867.

Haberly, L. B., & Price, J. L. (1978a). Association and commissural fiber systems of the olfactory cortex of the rat. *The Journal of Comparative Neurology*, *178*(4), 711–740. https://doi.org/10.1002/cne.901780408

Haberly, L. B., & Price, J. L. (1978b). Association and commissural fiber systems of the olfactory cortex of the rat. II. Systems originating in the olfactory peduncle. *The Journal of Comparative Neurology*, *181*(4), 781–807. https://doi.org/10.1002/cne.901810407

Haehner, A., Tosch, C., Wolz, M., Klingelhoefer, L., Fauser, M., Storch, A., Reichmann, H., & Hummel, T. (2013). Olfactory Training in Patients with Parkinson's Disease. *PLOS ONE*, *8*(4), e61680. https://doi.org/10.1371/journal.pone.0061680

Hagmann, P., Cammoun, L., Gigandet, X., Meuli, R., Honey, C. J., Wedeen, V. J., & Sporns, O. (2008). Mapping the Structural Core of Human Cerebral Cortex. *PLoS Biology*, *6*(7), e159. https://doi.org/10.1371/journal.pbio.0060159

Handley, O. J., Morrison, C. M., Miles, C., & Bayer, A. J. (2006). ApoE gene and familial risk of Alzheimer's disease as predictors of odour identification in older adults. *Neurobiology of Aging*, *27*(10), 1425–1430. https://doi.org/10.1016/j.neurobiolaging.2005.08.001

Hanekamp, S., Ćurčić-Blake, B., Caron, B., McPherson, B., Timmer, A., Prins, D., Boucard, C. C., Yoshida, M., Ida, M., Hunt, D., Jansonius, N. M., Pestilli, F., & Cornelissen, F. W. (2021). White matter alterations in glaucoma and monocular blindness differ outside the

visual system. *Scientific Reports*, *11*(1), Article 1. https://doi.org/10.1038/s41598-021-85602-x

Heather Hsu, C.-C., Rolls, E. T., Huang, C.-C., Chong, S. T., Zac Lo, C.-Y., Feng, J., & Lin, C.-P. (2020). Connections of the Human Orbitofrontal Cortex and Inferior Frontal Gyrus. *Cerebral Cortex*, *30*(11), 5830–5843. https://doi.org/10.1093/cercor/bhaa160

Heilingoetter, C. L., & Jensen, M. B. (2016). Histological methods for ex vivo axon tracing: A systematic review. *Neurological Research*, *38*(7), 561–569. https://doi.org/10.1080/01616412.2016.1153820

Hodes, R. J., Insel, T. R., Landis, S. C., & Research, O. behalf of the N. B. for N. (2013). The NIH Toolbox: Setting a standard for biomedical research. *Neurology*, *80*(11 Supplement 3), S1–S1. https://doi.org/10.1212/WNL.0b013e3182872e90

Hofstetter, S., Tavor, I., Moryosef, S. T., & Assaf, Y. (2013). Short-Term Learning Induces White Matter Plasticity in the Fornix. *Journal of Neuroscience*, *33*(31), 12844–12850. https://doi.org/10.1523/JNEUROSCI.4520-12.2013

Howard, J. D., Gottfried, J. A., Tobler, P. N., & Kahnt, T. (2015). Identity-specific coding of future rewards in the human orbitofrontal cortex. *Proceedings of the National Academy of Sciences of the United States of America*, *112*(16), 5195–5200. https://doi.org/10.1073/pnas.1503550112

Howard, J. D., & Kahnt, T. (2017). Identity-Specific Reward Representations in Orbitofrontal Cortex Are Modulated by Selective Devaluation. *The Journal of Neuroscience: The Official Journal of the Society for Neuroscience*, *37*(10), 2627–2638. https://doi.org/10.1523/JNEUROSCI.3473-16.2017

Howard, J. D., & Kahnt, T. (2021). To be specific: The role of orbitofrontal cortex in signaling reward identity. *Behavioral Neuroscience*, *135*(2), 210–217. https://doi.org/10.1037/bne0000455

Howard, J. D., Reynolds, R., Smith, D. E., Voss, J. L., Schoenbaum, G., & Kahnt, T. (2020). Targeted Stimulation of Human Orbitofrontal Networks Disrupts Outcome-Guided Behavior. *Current Biology: CB*, *30*(3), 490-498.e4. https://doi.org/10.1016/j.cub.2019.12.007

Howell, J., Costanzo, R. M., & Reiter, E. R. (2018). Head trauma and olfactory function. *World Journal of Otorhinolaryngology - Head and Neck Surgery*, *4*(1), 39–45. https://doi.org/10.1016/j.wjorl.2018.02.001

Illig, K. R. (2005). Projections from orbitofrontal cortex to anterior piriform cortex in the rat suggest a role in olfactory information processing. *Journal of Comparative Neurology*, *488*(2), 224–231. https://doi.org/10.1002/cne.20595

Itami, S., & Uno, H. (2002). Orbitofrontal cortex dysfunction in attention-deficit hyperactivity disorder revealed by reversal and extinction tasks. *NeuroReport*, *13*(18), 2453–2457.

Jack, C. R., Knopman, D. S., Jagust, W. J., Shaw, L. M., Aisen, P. S., Weiner, M. W., Petersen, R. C., & Trojanowski, J. Q. (2010). Hypothetical model of dynamic biomarkers of the Alzheimer's pathological cascade. *Lancet Neurology*, *9*(1), 119. https://doi.org/10.1016/S1474-4422(09)70299-6

Janssen, T. W. P., Hillebrand, A., Gouw, A., Geladé, K., Van Mourik, R., Maras, A., & Oosterlaan, J. (2017). Neural network topology in ADHD; evidence for maturational

delay and default-mode network alterations. *Clinical Neurophysiology*, *128*(11), 2258–2267. https://doi.org/10.1016/j.clinph.2017.09.004

Jenkinson, M., Beckmann, C. F., Behrens, T. E. J., Woolrich, M. W., & Smith, S. M. (2012). FSL. *NeuroImage*, *62*(2), 782–790. https://doi.org/10.1016/j.neuroimage.2011.09.015

Jeurissen, B., Descoteaux, M., Mori, S., & Leemans, A. (2019). Diffusion MRI fiber tractography of the brain. *NMR in Biomedicine*, *32*(4), e3785. https://doi.org/10.1002/nbm.3785

Jeurissen, B., Leemans, A., Tournier, J.-D., Jones, D. K., & Sijbers, J. (2013). Investigating the prevalence of complex fiber configurations in white matter tissue with diffusion magnetic resonance imaging. *Human Brain Mapping*, *34*(11), 2747–2766. https://doi.org/10.1002/hbm.22099

Jiramongkolchai, P., Jones, M. S., Peterson, A., Lee, J. J., Liebendorfer, A., Klatt-Cromwell, C. N., Schneider, J. S., Drescher, A. J., Ogden, M. A., Brunworth, J. D., Kallogjeri, D., Kukuljan, S., Peelle, J. E., & Piccirillo, J. F. (2021). Association of Olfactory Training with Neural Connectivity in Adults with Postviral Olfactory Dysfunction. *JAMA Otolaryngology - Head and Neck Surgery*, *147*(6), 502–509. https://doi.org/10.1001/jamaoto.2021.0086

Jones-Gotman, M., & Zatorre, R. J. (1993). Odor recognition memory in humans: Role of right temporal and orbitofrontal regions. *Brain and Cognition*, *22*, 182–198. https://doi.org/10.1006/brcg.1993.1033

Josefsson, M., Larsson, M., Nordin, S., Adolfsson, R., & Olofsson, J. (2017). APOE-ε4 effects on longitudinal decline in olfactory and non-olfactory cognitive abilities in middle-aged and old adults. *Scientific Reports*, *7*, 1286. https://doi.org/10.1038/s41598-017-01508-7

Kahnt, T., Chang, L. J., Park, S. Q., Heinzle, J., & Haynes, J.-D. (2012). Connectivity-Based Parcellation of the Human Orbitofrontal Cortex. *Journal of Neuroscience*, *32*(18), 6240–6250.

Kahnt, T., & Tobler, P. N. (2017). Dopamine Modulates the Functional Organization of the Orbitofrontal Cortex. *Journal of Neuroscience*, *37*(6), 1493–1504.

Klawiter, E. C., Schmidt, R. E., Trinkaus, K., Liang, H.-F., Budde, M. D., Naismith, R. T., Song, S.-K., Cross, A. H., & Benzinger, T. L. (2011). Radial diffusivity predicts demyelination in ex vivo multiple sclerosis spinal cords. *NeuroImage*, *55*(4), 1454–1460. https://doi.org/10.1016/j.neuroimage.2011.01.007

Klein, J., Yan, X., Johnson, A., Tomljanovic, Z., Zou, J., Polly, K., Honig, L. S., Brickman, A. M., Stern, Y., Devanand, D. P., Lee, S., & Kreisl, W. C. (2021). Olfactory Impairment Is Related to Tau Pathology and Neuroinflammation in Alzheimer's Disease. *Journal of Alzheimer's Disease: JAD*, *80*(3), 1051–1065. https://doi.org/10.3233/JAD-201149

Krantz, E. M., Schubert, C. R., Dalton, D. S., Zhong, W., Huang, G. H., Klein, B. E. K., Klein, R., Nieto, F. J., & Cruickshanks, K. J. (2009). Test–Retest Reliability of the San Diego Odor Identification Test and Comparison with the Brief Smell Identification Test. *Chemical Senses*, *34*(5), 435–440. https://doi.org/10.1093/chemse/bjp018

Kringelbach, M. L., & Rolls, E. T. (2004). The functional neuroanatomy of the human orbitofrontal cortex: Evidence from neuroimaging and neuropsychology. *Progress in Neurobiology*, *72*(5), 341–372. https://doi.org/10.1016/j.pneurobio.2004.03.006

Kutscheidt, K., Dresler, T., Hudak, J., Barth, B., Blume, F., Ethofer, T., Fallgatter, A. J., & Ehlis, A.-C. (2019). Interoceptive awareness in patients with attention-deficit/hyperactivity disorder (ADHD). *ADHD Attention Deficit and Hyperactivity Disorders*, *11*(4), 395–401. https://doi.org/10.1007/s12402-019-00299-3

Lafaille-Magnan, M.-E., Poirier, J., Etienne, P., Tremblay-Mercier, J., Frenette, J., Rosa-Neto, P., Breitner, J. C. S., & PREVENT-AD Research Group. (2017). Odor identification as a biomarker of preclinical AD in older adults at risk. *Neurology*, *89*(4), 327–335. https://doi.org/10.1212/WNL.0000000000004159

Lee, E. T. Y. (1989). Choosing nodes in parametric curve interpolation. *Computer-Aided Design*, *21*(6), 363–370. https://doi.org/10.1016/0010-4485(89)90003-1

Leng, B., Han, S., Bao, Y., Zhang, H., Wang, Y., Wu, Y., & Wang, Y. (2016). The uncinate fasciculus as observed using diffusion spectrum imaging in the human brain. *Neuroradiology*, *58*(6), 595–606. https://doi.org/10.1007/s00234-016-1650-9

Li, L.-M., Yang, L.-N., Zhang, L.-J., Fu, Y., Li, T., Qi, Y., Wang, J., Zhang, D.-Q., Zhang, N., Liu, J., & Yang, L. (2016). Olfactory dysfunction in patients with multiple sclerosis. *Journal of the Neurological Sciences*, *365*, 34–39. https://doi.org/10.1016/j.jns.2016.03.045

Li, W., Lopez, L., Osher, J., Howard, J. D., Parrish, T. B., & Gottfried, J. A. (2010). Right orbitofrontal cortex mediates conscious olfactory perception. *Psychological Science*, *21*(10), 1454–1463. https://doi.org/10.1177/0956797610382121

Li, W., Luxenberg, E., Parrish, T., & Gottfried, J. A. (2006). Learning to Smell the Roses: Experience-Dependent Neural Plasticity in Human Piriform and Orbitofrontal Cortices. *Neuron*, *52*(6), 1097–1108. https://doi.org/10.1016/j.neuron.2006.10.026

Li, X., Morgan, P. S., Ashburner, J., Smith, J., & Rorden, C. (2016). The first step for neuroimaging data analysis: DICOM to NIfTI conversion. *Journal of Neuroscience Methods*, *264*, 47–56. https://doi.org/10.1016/j.jneumeth.2016.03.001

Lucassen, E. B., Turel, A., Knehans, A., Huang, X., & Eslinger, P. (2016). Olfactory dysfunction in Multiple Sclerosis: A scoping review of the literature. *Multiple Sclerosis and Related Disorders*, *6*, 1–9. https://doi.org/10.1016/j.msard.2015.12.002

Mackey, S., & Petrides, M. (2010). Quantitative demonstration of comparable architectonic areas within the ventromedial and lateral orbital frontal cortex in the human and the macaque monkey brains. *The European Journal of Neuroscience*, *32*(11), 1940–1950. https://doi.org/10.1111/j.1460-9568.2010.07465.x

Mai, J., Majtanik, M., & Paxinos, G. (2015). *Atlas of the human brain* (4th ed.). Academic Press.

Mark, L. P., Daniels, D. L., Naidich, T. P., Hendrix, L. E., & Maas, E. (1994). Anatomic moment. The septal area. *AJNR. American Journal of Neuroradiology*, *15*(2), 273–276.

Martino, J., Brogna, C., Robles, S. G., Vergani, F., & Duffau, H. (2010). Anatomic dissection of the inferior fronto-occipital fasciculus revisited in the lights of brain stimulation data. *Cortex*, *46*(5), 691–699. https://doi.org/10.1016/j.cortex.2009.07.015

Mayeux, R., & Stern, Y. (2012). Epidemiology of Alzheimer Disease. *Cold Spring Harbor Perspectives in Medicine*, *2*(8), a006239. https://doi.org/10.1101/cshperspect.a006239

McGann, J. P. (2017). Poor human olfaction is a 19th-century myth. *Science (New York, N.Y.)*, *356*(6338). https://doi.org/10.1126/science.aam7263

Mesulam, M.-M., Mash, D., Hersh, L., Bothwell, M., & Geula, C. (1992). Cholinergic innervation of the human striatum, globus pallidus, subthalamic nucleus, substantia nigra, and red nucleus. *Journal of Comparative Neurology*, *323*(2), 252–268. https://doi.org/10.1002/cne.903230209

Miao, W., Li, J., Tang, M., Xian, J., Li, W., Liu, Z., Liu, S., Sabel, B. A., Wang, Z., & He, H. (2013). Altered White Matter Integrity in Adolescents with Prelingual Deafness: A High-Resolution Tract-Based Spatial Statistics Imaging Study. *AJNR: American Journal of Neuroradiology*, *34*(6), 1264–1270. https://doi.org/10.3174/ajnr.A3370

Milardi, D., Cacciola, A., Calamuneri, A., Ghilardi, M. F., Caminiti, F., Cascio, F., Andronaco, V., Anastasi, G., Mormina, E., Arrigo, A., Bruschetta, D., & Quartarone, A. (2017). The Olfactory System Revealed: Non-Invasive Mapping by using Constrained Spherical Deconvolution Tractography in Healthy Humans. *Frontiers in Neuroanatomy*, *11*. https://doi.org/10.3389/fnana.2017.00032

Miyamichi, K., Amat, F., Moussavi, F., Wang, C., Wickersham, I., Wall, N. R., Taniguchi, H., Tasic, B., Huang, Z. J., He, Z., Callaway, E. M., Horowitz, M. A., & Luo, L. (2011). Cortical representations of olfactory input by trans-synaptic tracing. *Nature*, *472*(7342), 191–196. https://doi.org/10.1038/nature09714

Mobley, A. S., Rodriguez-Gil, D. J., Imamura, F., & Greer, C. A. (2014). Aging in the olfactory system. *Trends in Neurosciences*, *37*(2), 77–84. https://doi.org/10.1016/j.tins.2013.11.004

Morgan, C. D., Nordin, S., & Murphy, C. (1995). Odor identification as an early marker for Alzheimer's disease: Impact of lexical functioning and detection sensitivity. *Journal of Clinical and Experimental Neuropsychology*, *17*(5), 793–803. https://doi.org/10.1080/01688639508405168

Mori, S. (2007). *Introduction to Diffusion Tensor Imaging*. Elsevier Science. https://doi.org/10.1016/B978-0-444-52828-5.X5014-5

Morris, J. C., Weintraub, S., Chui, H. C., Cummings, J., DeCarli, C., Ferris, S., Foster, N. L., Galasko, D., Graff-Radford, N., Peskind, E. R., Beekly, D., Ramos, E. M., & Kukull, W. A. (2006). The Uniform Data Set (UDS): Clinical and Cognitive Variables and Descriptive Data From Alzheimer Disease Centers. *Alzheimer Disease & Associated Disorders*, *20*(4), 210–216. https://doi.org/10.1097/01.wad.0000213865.09806.92

Murphy, C. (2019). Olfactory and other sensory impairments in Alzheimer disease. *Nature Reviews Neurology*, *15*(1), 11–24. https://doi.org/10.1038/s41582-018-0097-5

Murphy, C., Gilmore, M. M., Seery, C. S., Salmon, D. P., & Lasker, B. R. (1990). Olfactory thresholds are associated with degree of dementia in Alzheimer's disease. *Neurobiology of Aging*, *11*(4), 465–469. https://doi.org/10.1016/0197-4580(90)90014-q

Negoias, S., Croy, I., Gerber, J., Puschmann, S., Petrowski, K., Joraschky, P., & Hummel, T. (2010). Reduced olfactory bulb volume and olfactory sensitivity in patients with acute major depression. *Neuroscience*, *169*(1), 415–421. https://doi.org/10.1016/j.neuroscience.2010.05.012

Nordin, S., & Murphy, C. (1996). Impaired sensory and cognitive olfactory function in questionable Alzheimer's disease. *Neuropsychology*, *10*, 113–119. https://doi.org/10.1037/0894-4105.10.1.113

Nunes, R., Hajnal, J., Golay, X., & Larkman, D. J. (2006). Simultaneous slice excitation and reconstruction for single shot EPI. *Proceedings of the 14th Annual Meeting of ISMRM*.

O'Doherty, J., Rolls, E. T., Francis, S., Bowtell, R., McGlone, F., Kobal, G., Renner, B., & Ahne, G. (2000). Sensory-specific satiety-related olfactory activation of the human orbitofrontal cortex. *Neuroreport*, *11*(2), 399–403. https://doi.org/10.1097/00001756-200002070-00035

Ogawa, S., Takemura, H., Horiguchi, H., Terao, M., Haji, T., Pestilli, F., Yeatman, J. D., Tsuneoka, H., Wandell, B. A., & Masuda, Y. (2014). White Matter Consequences of Retinal Receptor and Ganglion Cell Damage. *Investigative Ophthalmology & Visual Science*, *55*(10), 6976–6986. https://doi.org/10.1167/iovs.14-14737

Oleson, S., & Murphy, C. (2015). Olfactory Dysfunction in ApoE ε4/4 Homozygotes with Alzheimer's Disease. *Journal of Alzheimer's Disease: JAD*, *46*(3), 791–803. https://doi.org/10.3233/JAD-150089

Olofsson, J. K., Nordin, S., Wiens, S., Hedner, M., Nilsson, L.-G., & Larsson, M. (2010). Odor identification impairment in carriers of ApoE-varepsilon4 is independent of clinical dementia. *Neurobiology of Aging*, *31*(4), 567–577. https://doi.org/10.1016/j.neurobiolaging.2008.05.019

Öngür, D., An, X., & Price, J. l. (1998). Prefrontal cortical projections to the hypothalamus in Macaque monkeys. *Journal of Comparative Neurology*, *401*(4), 480–505. https://doi.org/10.1002/(SICI)1096-9861(19981130)401:4<480::AID-CNE4>3.0.CO;2-F

Ongür, D., Ferry, A. T., & Price, J. L. (2003a). Architectonic subdivision of the human orbital and medial prefrontal cortex. *The Journal of Comparative Neurology*, *460*(3), 425–449. https://doi.org/10.1002/cne.10609

Ongür, D., Ferry, A. T., & Price, J. L. (2003b). Architectonic subdivision of the human orbital and medial prefrontal cortex. *The Journal of Comparative Neurology*, *460*(3), 425–449. https://doi.org/10.1002/cne.10609

Öngür, D., & Price, J. L. (2000). The Organization of Networks within the Orbital and Medial Prefrontal Cortex of Rats, Monkeys and Humans. *Cerebral Cortex*, *10*(3), 206–219. https://doi.org/10.1093/cercor/10.3.206

Palmquist, E., Larsson, M., Olofsson, J. K., Seubert, J., Bäckman, L., & Laukka, E. J. (2020). A Prospective Study on Risk Factors for Olfactory Dysfunction in Aging. *The Journals of Gerontology. Series A, Biological Sciences and Medical Sciences*, *75*(3), 603–610. https://doi.org/10.1093/gerona/glz265

Panikratova, Y. R., Vlasova, R. M., Akhutina, T. V., Korneev, A. A., Sinitsyn, V. E., & Pechenkova, E. V. (2020). Functional connectivity of the dorsolateral prefrontal cortex contributes to different components of executive functions. *International Journal of Psychophysiology*, *151*, 70–79. https://doi.org/10.1016/j.ijpsycho.2020.02.013

Patenaude, B., Smith, S. M., Kennedy, D. N., & Jenkinson, M. (2011). A Bayesian model of shape and appearance for subcortical brain segmentation. *NeuroImage*, *56*(3), 907–922. https://doi.org/10.1016/j.neuroimage.2011.02.046

Patino, J., Karagas, N. E., Chandra, S., Thakur, N., & Stimming, E. F. (2021). Olfactory Dysfunction in Huntington's Disease. *Journal of Huntington's Disease*, *10*(4), 413–422. https://doi.org/10.3233/JHD-210497

Pestilli, F., Yeatman, J. D., Rokem, A., Kay, K. N., & Wandell, B. A. (2014). Evaluation and statistical inference for living connectomes. *Nature Methods*, *11*(10), 1058–1063. https://doi.org/10.1038/nmeth.3098

Peters, J. M., Hummel, T., Kratzsch, T., Lötsch, J., Skarke, C., & Frölich, L. (2003). Olfactory function in mild cognitive impairment and Alzheimer's disease: An investigation using psychophysical and electrophysiological techniques. *The American Journal of Psychiatry*, *160*(11), 1995–2002. https://doi.org/10.1176/appi.ajp.160.11.1995

Petersen, R. C., Caracciolo, B., Brayne, C., Gauthier, S., Jelic, V., & Fratiglioni, L. (2014). Mild cognitive impairment: A concept in evolution. *Journal of Internal Medicine*, *275*(3), 214–228. https://doi.org/10.1111/joim.12190

Petrides, M., & Pandya, D. N. (2002). Comparative cytoarchitectonic analysis of the human and the macaque ventrolateral prefrontal cortex and corticocortical connection patterns in the monkey. *The European Journal of Neuroscience*, *16*(2), 291–310. https://doi.org/10.1046/j.1460-9568.2001.02090.x

Pierpaoli, C., Jezzard, P., Basser, P. J., Barnett, A., & Di Chiro, G. (1996). Diffusion tensor MR imaging of the human brain. *Radiology*, *201*(3), 637–648. https://doi.org/10.1148/radiology.201.3.8939209

Pinto, J. M., Wroblewski, K. E., Kern, D. W., Schumm, L. P., & McClintock, M. K. (2014). Olfactory dysfunction predicts 5-year mortality in older adults. *PloS One*, *9*(10), e107541. https://doi.org/10.1371/journal.pone.0107541

Poellinger, A., Thomas, R., Lio, P., Lee, A., Makris, N., Rosen, B. R., & Kwong, K. K. (2001). Activation and habituation in olfaction—An fMRI study. *NeuroImage*, *13*(4), 547–560. https://doi.org/10.1006/nimg.2000.0713

Porter, D. A., & Heidemann, R. M. (2009). High resolution diffusion-weighted imaging using readout-segmented echo-planar imaging, parallel imaging and a two-dimensional navigator-based reacquisition. *Magnetic Resonance in Medicine*, *62*(2), 468–475. https://doi.org/10.1002/mrm.22024

Potter, H., & Butters, N. (1980). An assessment of olfactory deficits in patients with damage to prefrontal cortex. *Neuropsychologia*, *18*(6), 621–628. https://doi.org/10.1016/0028-3932(80)90101-3

Potter, H., & Nauta, W. J. H. (1979). A note on the problem of olfactory associations of the orbitofrontal cortex in the monkey. *Neuroscience*, *4*(3), 361–367. https://doi.org/10.1016/0306-4522(79)90099-X

Power, J. D., Silver, B. M., Silverman, M. R., Ajodan, E. L., Bos, D. J., & Jones, R. M. (2019). Customized head molds reduce motion during resting state fMRI scans. *NeuroImage*, *189*, 141–149. https://doi.org/10.1016/j.neuroimage.2019.01.016

Price, J. L., Davis, P. B., Morris, J. C., & White, D. L. (1991). The distribution of tangles, plaques and related immunohistochemical markers in healthy aging and Alzheimer's disease. *Neurobiology of Aging*, *12*(4), 295–312. https://doi.org/10.1016/0197-4580(91)90006-6

Price, J. L., & Slotnick, B. M. (1983). Dual olfactory representation in the rat thalamus: An anatomical and electrophysiological study. *The Journal of Comparative Neurology*, *215*(1), 63–77. https://doi.org/10.1002/cne.902150106

Ray, J. P., & Price, J. L. (1992). The organization of the thalamocortical connections of the mediodorsal thalamic nucleus in the rat, related to the ventral forebrain–prefrontal cortex topography. *Journal of Comparative Neurology*, *323*(2), 167–197. https://doi.org/10.1002/cne.903230204

Rempel-Clower, N. l., & Barbas, H. (1998). Topographic organization of connections between the hypothalamus and prefrontal cortex in the rhesus monkey. *Journal of Comparative Neurology*, *398*(3), 393–419. https://doi.org/10.1002/(SICI)1096-9861(19980831)398:3<393::AID-CNE7>3.0.CO;2-V

Roalf, D. R., Moberg, M. J., Turetsky, B. I., Brennan, L., Kabadi, S., Wolk, D. A., & Moberg, P. J. (2017). A quantitative meta-analysis of olfactory dysfunction in mild cognitive impairment. *Journal of Neurology, Neurosurgery, and Psychiatry*, *88*(3), 226–232. https://doi.org/10.1136/jnnp-2016-314638

Robbins, T. W., Weinberger, D., Taylor, J. G., Morris, R. G., Roberts, A. C., Robbins, T. W., & Weiskrantz, L. (1996). Dissociating executive functions of the prefrontal cortex.

Philosophical Transactions of the Royal Society of London. Series B: Biological Sciences, *351*(1346), 1463–1471. https://doi.org/10.1098/rstb.1996.0131

Roberts, R. O., Christianson, T. J. H., Kremers, W. K., Mielke, M. M., Machulda, M. M., Vassilaki, M., Alhurani, R. E., Geda, Y. E., Knopman, D. S., & Petersen, R. C. (2016). Association Between Olfactory Dysfunction and Amnestic Mild Cognitive Impairment and Alzheimer Disease Dementia. *JAMA Neurology*, *73*(1), 93–101. https://doi.org/10.1001/jamaneurol.2015.2952

Rokem, A., Takemura, H., Bock, A. S., Scherf, K. S., Behrmann, M., Wandell, B. A., Fine, I., Bridge, H., & Pestilli, F. (2017). The visual white matter: The application of diffusion MRI and fiber tractography to vision science. *Journal of Vision*, *17*(2), 4. https://doi.org/10.1167/17.2.4

Rolls, E. T., Huang, C.-C., Lin, C.-P., Feng, J., & Joliot, M. (2020). Automated anatomical labelling atlas 3. *NeuroImage*, *206*, 116189. https://doi.org/10.1016/j.neuroimage.2019.116189

Rolls, E. T., Joliot, M., & Tzourio-Mazoyer, N. (2015). Implementation of a new parcellation of the orbitofrontal cortex in the automated anatomical labeling atlas. *NeuroImage*, *122*, 1–5. https://doi.org/10.1016/j.neuroimage.2015.07.075

Roosendaal, S. D., Geurts, J. J. G., Vrenken, H., Hulst, H. E., Cover, K. S., Castelijns, J. A., Pouwels, P. J. W., & Barkhof, F. (2009). Regional DTI differences in multiple sclerosis patients. *NeuroImage*, *44*(4), 1397–1403. https://doi.org/10.1016/j.neuroimage.2008.10.026

Rose, M. (1927). Die sog. Riechrinde beim Menschen und beim Affen. *Journal f. Psychologie Und Neurologie*, *34*(6), 261–401.

Rudebeck, P. H., & Rich, E. L. (2018). Orbitofrontal cortex. *Current Biology*, *28*, R1075–R1095.

Rumeau, C., Nguyen, D. T., & Jankowski, R. (2016). How to assess olfactory performance with the Sniffin' Sticks test(®). *European Annals of Otorhinolaryngology, Head and Neck Diseases*, *133*(3), 203–206. https://doi.org/10.1016/j.anorl.2015.08.004

Sampaio-Baptista, C., Khrapitchev, A. A., Foxley, S., Schlagheck, T., Scholz, J., Jbabdi, S., DeLuca, G. C., Miller, K. L., Taylor, A., Thomas, N., Kleim, J., Sibson, N. R., Bannerman, D., & Johansen-Berg, H. (2013). Motor Skill Learning Induces Changes in White Matter Microstructure and Myelination. *Journal of Neuroscience*, *33*(50), 19499–19503. https://doi.org/10.1523/JNEUROSCI.3048-13.2013

Schoenbaum, G., & Eichenbaum, H. (1995). Information coding in the rodent prefrontal cortex. I. Single-neuron activity in orbitofrontal cortex compared with that in pyriform cortex. *Journal of Neurophysiology*, *74*(2), 733–750. https://doi.org/10.1152/jn.1995.74.2.733

Scholz, J., Klein, M. C., Behrens, T. E. J., & Johansen-Berg, H. (2009). Training induces changes in white matter architecture. *Nature Neuroscience*, *12*(11), 1370–1371. https://doi.org/10.1038/nn.2412

Schubert, C. R., Carmichael, L. L., Murphy, C., Klein, B. E. K., Klein, R., & Cruickshanks, K. J. (2008). OLFACTION AND THE 5-YEAR INCIDENCE OF COGNITIVE IMPAIRMENT IN AN EPIDEMIOLOGIC STUDY OF OLDER ADULTS. *Journal of the American Geriatrics Society*, *56*(8), 1517–1521. https://doi.org/10.1111/j.1532-5415.2008.01826.x

Schwob, J. E., & Price, J. L. (1984). The development of lamination of afferent fibers to the olfactory cortex in rats, with additional observations in the adult. *Journal of Comparative Neurology*, *223*(2), 203–222. https://doi.org/10.1002/cne.902230205

Scott, J. W., McBride, R. L., & Schneider, S. P. (1980). The organization of projections from the olfactory bulb to the piriform cortex and olfactory tubercle in the rat. *The Journal of Comparative Neurology*, *194*(3), 519–534. https://doi.org/10.1002/cne.901940304

Seubert, J., Laukka, E. J., Rizzuto, D., Hummel, T., Fratiglioni, L., Bäckman, L., & Larsson, M. (2017). Prevalence and Correlates of Olfactory Dysfunction in Old Age: A Population-Based Study. *The Journals of Gerontology. Series A, Biological Sciences and Medical Sciences*, *72*(8), 1072–1079. https://doi.org/10.1093/gerona/glx054

Shu, C.-H., Yuan, B.-C., Lin, S.-H., & Lin, C.-Z. (2007). Cross-Cultural Application of the "Sniffin' Sticks" Odor Identification Test. *American Journal of Rhinology*, *21*(5), 570–573. https://doi.org/10.2500/ajr.2007.21.3075

Silk, T. J., Vance, A., Rinehart, N., Bradshaw, J. L., & Cunnington, R. (2008). Dysfunction in the Fronto-Parietal Network in Attention Deficit Hyperactivity Disorder (ADHD): An fMRI Study. *Brain Imaging and Behavior*, *2*(2), 123–131. https://doi.org/10.1007/s11682-008-9021-8

Skorpil, M., Rolheiser, T., Robertson, H., Sundin, A., & Svenningsson, P. (2011). Diffusion tensor fiber tractography of the olfactory tract. *Magnetic Resonance Imaging*, *29*(2), 289–292. https://doi.org/10.1016/j.mri.2010.07.004

Smith, R. E., Tournier, J.-D., Calamante, F., & Connelly, A. (2012). Anatomically-constrained tractography: Improved diffusion MRI streamlines tractography through effective use of

anatomical information. *NeuroImage*, *62*(3), 1924–1938. https://doi.org/10.1016/j.neuroimage.2012.06.005

Smith, R. E., Tournier, J.-D., Calamante, F., & Connelly, A. (2013). SIFT: Spherical-deconvolution informed filtering of tractograms. *NeuroImage*, *67*, 298–312. https://doi.org/10.1016/j.neuroimage.2012.11.049

Smith, R. E., Tournier, J.-D., Calamante, F., & Connelly, A. (2015a). The effects of SIFT on the reproducibility and biological accuracy of the structural connectome. *NeuroImage*, *104*, 253–265. https://doi.org/10.1016/j.neuroimage.2014.10.004

Smith, R. E., Tournier, J.-D., Calamante, F., & Connelly, A. (2015b). SIFT2: Enabling dense quantitative assessment of brain white matter connectivity using streamlines tractography. *NeuroImage*, *119*, 338–351. https://doi.org/10.1016/j.neuroimage.2015.06.092

Smith, S. M. (2002). Fast robust automated brain extraction. *Human Brain Mapping*, *17*(3), 143–155. https://doi.org/10.1002/hbm.10062

Smith, S. M., Jenkinson, M., Woolrich, M. W., Beckmann, C. F., Behrens, T. E. J., Johansen-Berg, H., Bannister, P. R., De Luca, M., Drobnjak, I., Flitney, D. E., Niazy, R. K., Saunders, J., Vickers, J., Zhang, Y., De Stefano, N., Brady, J. M., & Matthews, P. M. (2004). Advances in functional and structural MR image analysis and implementation as FSL. *NeuroImage*, *23 Suppl 1*, S208-219. https://doi.org/10.1016/j.neuroimage.2004.07.051

Sobel, N., Prabhakaran, V., Desmond, J. E., Glover, G. H., Goode, R. L., Sullivan, E. V., & Gabrieli, J. D. (1998). Sniffing and smelling: Separate subsystems in the human olfactory cortex. *Nature*, *392*(6673), 282–286. https://doi.org/10.1038/32654

Song, S.-K., Sun, S.-W., Ju, W.-K., Lin, S.-J., Cross, A. H., & Neufeld, A. H. (2003). Diffusion tensor imaging detects and differentiates axon and myelin degeneration in mouse optic nerve after retinal ischemia. *NeuroImage*, *20*(3), 1714–1722. https://doi.org/10.1016/j.neuroimage.2003.07.005

Song, S.-K., Yoshino, J., Le, T. Q., Lin, S.-J., Sun, S.-W., Cross, A. H., & Armstrong, R. C. (2005). Demyelination increases radial diffusivity in corpus callosum of mouse brain. *NeuroImage*, *26*(1), 132–140. https://doi.org/10.1016/j.neuroimage.2005.01.028

SPM12 Software—Statistical Parametric Mapping. (2014). Retrieved June 16, 2021, from https://www.fil.ion.ucl.ac.uk/spm/software/spm12/

Stalnaker, T. A., Cooch, N. K., & Schoenbaum, G. (2015). What the orbitofrontal cortex does not do. *Nature Neuroscience*, *18*(5), Article 5. https://doi.org/10.1038/nn.3982

Tanabe, T., Yarita, H., Iino, M., Ooshima, Y., & Takagi, S. F. (1975). An olfactory projection area in orbitofrontal cortex of the monkey. *Journal of Neurophysiology*, *38*(5), 1269–1283. https://doi.org/10.1152/jn.1975.38.5.1269

Tegelbeckers, J., Kanowski, M., Krauel, K., Haynes, J.-D., Breitling, C., Flechtner, H.-H., & Kahnt, T. (2018). Orbitofrontal Signaling of Future Reward is Associated with Hyperactivity in Attention-Deficit/Hyperactivity Disorder. *The Journal of Neuroscience: The Official Journal of the Society for Neuroscience*, *38*(30), 6779–6786. https://doi.org/10.1523/JNEUROSCI.0411-18.2018

Thiebaut de Schotten, M., Dell'Acqua, F., Valabregue, R., & Catani, M. (2012). Monkey to human comparative anatomy of the frontal lobe association tracts. *Cortex*, *48*(1), 82–96. https://doi.org/10.1016/j.cortex.2011.10.001

Thomas, C., & Baker, C. I. (2013). Teaching an adult brain new tricks: A critical review of evidence for training-dependent structural plasticity in humans. *NeuroImage*, *73*, 225–236. https://doi.org/10.1016/j.neuroimage.2012.03.069

Tournier, J.-D., Calamante, F., & Connelly, A. (2007). Robust determination of the fibre orientation distribution in diffusion MRI: Non-negativity constrained super-resolved spherical deconvolution. *NeuroImage*, *35*(4), 1459–1472. https://doi.org/10.1016/j.neuroimage.2007.02.016

Tournier, J.-D., Calamante, F., & Connelly, A. (2010). *Improved probabilistic streamlines tractography by 2nd order integration over fibre orientation distributions*. Proceedings of the International Society for Magnetic Resonance in Medicine.

Tournier, J.-D., Calamante, F., & Connelly, A. (2012). MRtrix: Diffusion tractography in crossing fiber regions. *International Journal of Imaging Systems and Technology*, *22*(1), 53–66. https://doi.org/10.1002/ima.22005

Tournier, J.-D., Calamante, F., & Connelly, A. (2013). Determination of the appropriate b value and number of gradient directions for high-angular-resolution diffusion-weighted imaging. *NMR in Biomedicine*, *26*(12), 1775–1786. https://doi.org/10.1002/nbm.3017

Tournier, J.-D., Smith, R., Raffelt, D., Tabbara, R., Dhollander, T., Pietsch, M., Christiaens, D., Jeurissen, B., Yeh, C.-H., & Connelly, A. (2019). MRtrix3: A fast, flexible and open

software framework for medical image processing and visualisation. *NeuroImage*, *202*, 116137. https://doi.org/10.1016/j.neuroimage.2019.116137

Tournier, J.-D., Yeh, C.-H., Calamante, F., Cho, K.-H., Connelly, A., & Lin, C.-P. (2008). Resolving crossing fibres using constrained spherical deconvolution: Validation using diffusion-weighted imaging phantom data. *NeuroImage*, *42*(2), 617–625. https://doi.org/10.1016/j.neuroimage.2008.05.002

Tu, L., Lv, X., Fan, Z., Zhang, M., Wang, H., & Yu, X. (2020). Association of Odor Identification Ability With Amyloid-β and Tau Burden: A Systematic Review and Meta-Analysis. *Frontiers in Neuroscience*, *14*. https://www.frontiersin.org/articles/10.3389/fnins.2020.586330

Tzourio-Mazoyer, N., Landeau, B., Papathanassiou, D., Crivello, F., Etard, O., Delcroix, N., Mazoyer, B., & Joliot, M. (2002). Automated anatomical labeling of activations in SPM using a macroscopic anatomical parcellation of the MNI MRI single-subject brain. *NeuroImage*, *15*(1), 273–289. https://doi.org/10.1006/nimg.2001.0978

Uddin, L. Q., Kelly, A. M. C., Biswal, B. B., Margulies, D. S., Shehzad, Z., Shaw, D., Ghaffari, M., Rotrosen, J., Adler, L. A., Castellanos, F. X., & Milham, M. P. (2008). Network homogeneity reveals decreased integrity of default-mode network in ADHD. *Journal of Neuroscience Methods*, *169*(1), 249–254. https://doi.org/10.1016/j.jneumeth.2007.11.031

Uyematsu, S. (1921). A STUDY OF THE CORTICAL OLFACTORY CENTER Based On TwoCases Of Unilateral Involement Of The Olfactory Lobe. *Archives of Neurology & Psychiatry*, *6*(2), 146–156.

Vassilaki, M., Christianson, T. J., Mielke, M. M., Geda, Y. E., Kremers, W. K., Machulda, M. M., Knopman, D. S., Petersen, R. C., Lowe, V. J., Jack, C. R., & Roberts, R. O. (2017). Neuroimaging biomarkers and impaired olfaction in cognitively normal individuals. *Annals of Neurology*, *81*(6), 871–882. https://doi.org/10.1002/ana.24960

Vos, S. J. B., Gordon, B. A., Su, Y., Visser, P. J., Holtzman, D. M., Morris, J. C., Fagan, A. M., & Benzinger, T. L. S. (2016). NIA-AA Staging of Preclinical Alzheimer Disease: Discordance and Concordance of CSF and Imaging Biomarkers. *Neurobiology of Aging*, *44*, 1–8. https://doi.org/10.1016/j.neurobiolaging.2016.03.025

Wallis, J. D. (2012). Cross-species studies of orbitofrontal cortex and value-based decision-making. *Nature Neuroscience*, *15*(1), Article 1. https://doi.org/10.1038/nn.2956

Wang, D., Qin, W., Liu, Y., Zhang, Y., Jiang, T., & Yu, C. (2013). Altered White Matter Integrity in the Congenital and Late Blind People. *Neural Plasticity*, *2013*, e128236. https://doi.org/10.1155/2013/128236

Wang, F., Howard, J. D., Voss, J. L., Schoenbaum, G., & Kahnt, T. (2020). Targeted Stimulation of an Orbitofrontal Network Disrupts Decisions Based on Inferred, Not Experienced Outcomes. *Journal of Neuroscience*, *40*(45), 8726–8733. https://doi.org/10.1523/JNEUROSCI.1680-20.2020

Wehling, E., Naess, H., Wollschlaeger, D., Hofstad, H., Bramerson, A., Bende, M., & Nordin, S. (2015). Olfactory dysfunction in chronic stroke patients. *BMC Neurology*, *15*(1), 199. https://doi.org/10.1186/s12883-015-0463-5

Weintraub, S., Besser, L., Dodge, H. H., Teylan, M., Ferris, S., Goldstein, F. C., Giordani, B., Kramer, J., Loewenstein, D., Marson, D., Mungas, D., Salmon, D., Welsh-Bohmer, K.,

Zhou, X.-H., Shirk, S. D., Atri, A., Kukull, W. A., Phelps, C., & Morris, J. C. (2018). Version 3 of the Alzheimer Disease Centers' Neuropsychological Test Battery in the Uniform Data Set (UDS). *Alzheimer Disease and Associated Disorders*, *32*(1), 10–17. https://doi.org/10.1097/WAD.0000000000000223

Weintraub, S., Karpouzian-Rogers, T., Peipert, J. D., Nowinski, C., Slotkin, J., Wortman, K., Ho, E., Rogalski, E., Carlsson, C., Giordani, B., Goldstein, F., Lucas, J., Manly, J. J., Rentz, D., Salmon, D., Snitz, B., Dodge, H. H., Riley, M., Eldes, F., … Gershon, R. (2021). ARMADA: Assessing reliable measurement in Alzheimer's disease and cognitive aging project methods. *Alzheimer's & Dementia*, *18*(8), 1–12. https://doi.org/10.1002/alz.12497

Weiskopf, N., Hutton, C., Josephs, O., & Deichmann, R. (2006). Optimal EPI parameters for reduction of susceptibility-induced BOLD sensitivity losses: A whole-brain analysis at 3 T and 1.5 T. *NeuroImage*, *33*(2), 493–504. https://doi.org/10.1016/j.neuroimage.2006.07.029

Westin, C., Peled, S., Gudbjartsson, H., Kikinis, R., & Jolesz, F. (1997). *Geometrical Diffusion Measures for MRI from Tensor Basis Analysis*. Paper presented at the meeting of the ISMRM '97, Vancouver Canada. https://www.bibsonomy.org/bibtex/286cfe4e41f5518d3348b4f99dfed8850/bmeyer

White, L. E. (1965). Olfactory bulb projections of the rat. *The Anatomical Record*, *152*(4), 465–479. https://doi.org/10.1002/ar.1091520406

Wikenheiser, A. M., & Schoenbaum, G. (2016). Over the river, through the woods: Cognitive maps in the hippocampus and orbitofrontal cortex. *Nature Reviews Neuroscience*, *17*(8), Article 8. https://doi.org/10.1038/nrn.2016.56

Wilson, R. S., Schneider, J. A., Arnold, S. E., Tang, Y., Boyle, P. A., & Bennett, D. A. (2007). Olfactory Identification and Incidence of Mild Cognitive Impairment in Older Age. *Archives of General Psychiatry*, *64*(7), 802–808. https://doi.org/10.1001/archpsyc.64.7.802

Wilson, R. S., Yu, L., & Bennett, D. A. (2011). Odor Identification and Mortality in Old Age. *Chemical Senses*, *36*(1), 63–67. https://doi.org/10.1093/chemse/bjq098

Witt, M., Bormann, K., Gudziol, V., Pehlke, K., Barth, K., Minovi, A., Hähner, A., Reichmann, H., & Hummel, T. (2009). Biopsies of olfactory epithelium in patients with Parkinson's disease. *Movement Disorders: Official Journal of the Movement Disorder Society*, *24*(6), 906–914. https://doi.org/10.1002/mds.22464

Witt, S. T., van Ettinger-Veenstra, H., Salo, T., Riedel, M. C., & Laird, A. R. (2021). What Executive Function Network is that? An Image-Based Meta-Analysis of Network Labels. *Brain Topography*, *34*(5), 598–607. https://doi.org/10.1007/s10548-021-00847-z

Woodward, M. R., Amrutkar, C. V., Shah, H. C., Benedict, R. H. B., Rajakrishnan, S., Doody, R. S., Yan, L., & Szigeti, K. (2017). Validation of olfactory deficit as a biomarker of Alzheimer disease. *Neurology: Clinical Practice*, *7*(1), 5–14. https://doi.org/10.1212/CPJ.0000000000000293

Woolrich, M. W., Jbabdi, S., Patenaude, B., Chappell, M., Makni, S., Behrens, T., Beckmann, C., Jenkinson, M., & Smith, S. M. (2009). Bayesian analysis of neuroimaging data in FSL. *NeuroImage*, *45*(1 Suppl), S173-186. https://doi.org/10.1016/j.neuroimage.2008.10.055

Yang, D.-Y., Chi, M. H., Chu, C.-L., Lin, C.-Y., Hsu, S.-E., Chen, K. C., Lee, I. H., Chen, P. S., & Yang, Y. K. (2019). Orbitofrontal dysfunction during the reward process in adults with ADHD: An fMRI study. *Clinical Neurophysiology*, *130*(5), 627–633. https://doi.org/10.1016/j.clinph.2019.01.022

Yarita, H., Iino, M., Tanabe, T., Kogure, S., & Takagi, S. F. (1980). A transthalamic olfactory pathway to orbitofrontal cortex in the monkey. *Journal of Neurophysiology*, *43*(1), 69–85. https://doi.org/10.1152/jn.1980.43.1.69

Yeatman, J. D., Dougherty, R. F., Myall, N. J., Wandell, B. A., & Feldman, H. M. (2012). Tract profiles of white matter properties: Automating fiber-tract quantification. *PloS One*, *7*(11), e49790. https://doi.org/10.1371/journal.pone.0049790

Yeatman, J. D., Dougherty, R. F., Rykhlevskaia, E., Sherbondy, A. J., Deutsch, G. K., Wandell, B. A., & Ben-Shachar, M. (2011). Anatomical properties of the arcuate fasciculus predict phonological and reading skills in children. *Journal of Cognitive Neuroscience*, *23*(11), 3304–3317. https://doi.org/10.1162/jocn_a_00061

Yendiki, A., Aggarwal, M., Axer, M., Howard, A. F. D., van Walsum, A.-M. van C., & Haber, S. N. (2022). Post mortem mapping of connectional anatomy for the validation of diffusion MRI. *NeuroImage*, *256*, 119146. https://doi.org/10.1016/j.neuroimage.2022.119146

Yerys, B. E., Tunç, B., Satterthwaite, T. D., Antezana, L., Mosner, M. G., Bertollo, J. R., Guy, L., Schultz, R. T., & Herrington, J. D. (2019). Functional Connectivity of Frontoparietal and Salience/Ventral Attention Networks Have Independent Associations With Co-occurring Attention-Deficit/Hyperactivity Disorder Symptoms in Children With Autism.

Biological Psychiatry: Cognitive Neuroscience and Neuroimaging, *4*(4), 343–351. https://doi.org/10.1016/j.bpsc.2018.12.012

Yoo, H. S., Jeon, S., Chung, S. J., Yun, M., Lee, P. H., Sohn, Y. H., Evans, A. C., & Ye, B. S. (2018). Olfactory dysfunction in Alzheimer's disease- and Lewy body-related cognitive impairment. *Alzheimer's & Dementia: The Journal of the Alzheimer's Association*, *14*(10), 1243–1252. https://doi.org/10.1016/j.jalz.2018.05.010

Yushkevich, P. A., Piven, J., Hazlett, H. C., Smith, R. G., Ho, S., Gee, J. C., & Gerig, G. (2006). User-guided 3D active contour segmentation of anatomical structures: Significantly improved efficiency and reliability. *NeuroImage*, *31*(3), 1116–1128. https://doi.org/10.1016/j.neuroimage.2006.01.015

Zatorre, R. J., & Jones-Gotman, M. (1991). Human olfactory discrimination after unilateral frontal or temporal lobectomy. *Brain: A Journal of Neurology*, *114 (Pt 1A)*, 71–84.

Zhang, Y., Brady, M., & Smith, S. (2001). Segmentation of brain MR images through a hidden Markov random field model and the expectation-maximization algorithm. *IEEE Transactions on Medical Imaging*, *20*(1), 45–57. https://doi.org/10.1109/42.906424

Zhou, G., Lane, G., Cooper, S. L., Kahnt, T., & Zelano, C. (2019). Characterizing functional pathways of the human olfactory system. *ELife*, *8*. https://doi.org/10.7554/eLife.47177